Quantum metrology with high-density atomic vapors and squeezed states of light

DISSERTATION

submitted for the degree of
Doctor of Philosophy
by
Vito Giovanni Lucivero

ICFO - Institut de Ciències Fotòniques
BIST - Barcelona Institute of Science and Technology
UPC - Universitat Politecnica de Catalunya

Thesis Advisor: Prof. Dr. Morgan W.Mitchell

Abstract

Nowadays there is a considerable progress in optical magnetometry and spin noise spectroscopy, which use magnetically-sensitive atomic ensembles and optical read-out, approaching the limits set by quantum mechanics. In recent years optical magnetometers have become the most sensitive instruments for measuring low-frequency magnetic fields, achieving sub-femtotesla sensitivity and surpassing the competitive superconducting quantum interference devices (SQUIDs), and have found applications in biomedicine, geophysics, space science as well as in tests of fundamental physics. Another emerging technique is spin noise spectroscopy (SNS), which allows one to determine physical properties of an unperturbed spin system from its power noise spectrum. In the last decade technological advances like real-time spectrum analyzers and shot-noise-limited detectors have allowed improvements in the sensitivity of spin noise detection leading to a broad range of applications in both atomic and solid state physics.

The main goal of this thesis is to address a major outstanding question: whether squeezed light can improve the sensitivity of atomic sensors under optimal sensitivity conditions, typically in a high-density regime due to the statistical advantage of using more atoms.

Firstly, we describe the design, construction and characterization of a new versatile experimental apparatus for the study of squeezed-light atomic spectroscopy within a high-density regime ($n \geq 10^{12}$ cm^{-3}) and low-noise ($\simeq$ pT/$\sqrt{\text{Hz}}$) magnetic environment. The new experimental system is combined with an existing source of polarization squeezed light based on spontaneous parametric down conversion (SPDC) in a nonlinear crystal, which is the active medium of an optical parametric oscillator.

Secondly, we report the first experimental demonstration of quantum-enhanced

spin noise spectroscopy of natural abundance Rb via polarization squeezing of the probe beam. We found that input squeezing of 3.0 dB improves the signal-to-noise ratio by 1.5 dB to 2.6 dB over the combined (power)$\otimes$(number density) ranges (0.5 mW to 4.0 mW)$\otimes$($1.5 \times 10^{12}\text{cm}^{-3}$ to $1.3 \times 10^{13}\text{cm}^{-3}$), covering the ranges used in optimized spin noise spectroscopy experiments. We also show that squeezing improves the trade-off between statistical sensitivity and broadening effects.

Next, we introduce a novel theoretical model by defining a standard quantum limit (SQL) for optically-detected noise spectroscopy, identified as a bound to the covariance of the parameters estimated by fitting power noise spectra. We test the model for spin noise spectroscopy of natural abundance Rb and we demonstrate experimental performance of SNS at the SQL for a coherent probe and below the SQL for a polarization squeezed probe.

Finally, we report an optical magnetometer based on amplitude modulated optical rotation (AMOR), using a ^{85}Rb vapor cell, that achieves room temperature sensitivity of 70 fT/$\sqrt{\text{Hz}}$ at 7.6 μT and we demonstrate its photon shot-noise-limited (SNL) behaviour from 5 μT to 75 μT. While no quantum resources of light were used in this second experiment, the combination of best sensitivity, in the class of room-temperature scalar magnetometers, and SNL operation makes the system a promising candidate for application of squeezed light to an optimized optical magnetometer with best-in-class sensitivity.

Dedication

To my parents

Contents

Chapter 1

Introduction

1.1 Context and motivation

The study of the interaction between light and matter in the presence of a magnetic field, i.e. magneto-optics, is one of the most long-lived topic in physics and has had a crucial impact on the development of modern science and technology. This long tradition of scientific inquiry started with milestone discoveries, among the others, by *Faraday* [1, 2] and *Voigt* [3] of the rotation of the polarization plane of a linearly polarized probe through its interaction with an atomic medium placed in a longitudinal or transverse magnetic field, respectively. Starting from the 1970's, the rise of laser technology together with the development of the theory of optical pumping [4], have enabled physicists to investigate regimes with stronger interaction between atoms and light fields, nonlinear magneto-optical effects were discovered [5, 6], and the scheme based on the generation of atomic polarization and the detection of its magneto-optical evolution became a robust and standard

approach in precision measurements performed with atomic ensembles, i.e. atomic metrology.

Nowadays, there is a considerable progress in precision measurements that use magnetically-sensitive atomic ensembles and optical read-out. In this context the most vibrant topic is *optical magnetometry* [7]: in recent years optical magnetometers have surpassed in sensitivity the superconducting quantum interference devices (SQUID) by reaching the sub-femtotesla level of magnetic sensitivity [8, 9, 10]. Magnetic fields are present within a huge variety of natural phenomena and optical magnetometers have found applications in many scientific areas including biomedicine [11, 12, 13], geophysics [14, 15, 16], space science [17, 18] as well as in tests of fundamental physics [19, 20, 21]. Chip-scale atomic magnetometers [22] have been also developed and could help realize tiny mass-producible devices with high sensitivity and low power consumption. Another emerging technique that we investigate in this thesis is *spin noise spectroscopy* (SNS), which allows one to determine physical properties of an unperturbed spin system from its power noise spectrum. Even if extracting information through the intrinsic fluctuations of a spin system was theoretically predicted in the 1940's [23], just in the last decade technological advances like real-time FFT spectrum analyzers and shot-noise-limited detectors have improved the sensitivity of spin noise detection in both atomic [24] and solid state [25] physics, making SNS an established method to study g-factors, nuclear spin, isotope abundance ratios and spin lifetime in atomic gases [26, 27] as well as conduction electrons [28] and localized states in semiconductors [29] under thermal equilibrium. Altough non-optical noise spectroscopies based on resonance force microscopy [30, 31] and NV-center magnetometry [32, 33, 34] have recently emerged, the most sensitive and wide

used technique, pioneered by Aleksandrov and Zapasskii [35], is based on optical Faraday rotation (FR).

The sensitivity of FR-based spin noise spectroscopy is limited by the photon-shot-noise, a noise contribution due to the quantum nature of light and to the random time arrival of photons at the detection stage. When the number of photons of the probe beam that hit the detector is N, then the intrinsic uncertainty on the estimated phase ϕ (polarization rotation angle) has the quantum noise scaling $\delta\phi \sim 1/\sqrt{N}$. The same shot-noise contribution represents one of the quantum limitations to the sensitivity of optical magnetometers approaching fundamental limits. However, quantum optics provides a way of performing sub-shot-noise measurements by using squeezed states of light. Following the original proposal from Caves [36], squeezed states have been applied to several interferometer schemes as in the seminal experiments of polarization interferometry [37] and saturated absorption spectroscopy [38], in quantum measurements with cold atoms [39] and, more recently, in optical magnetometry [40], gravitational-wave detection [41] and biological measurements [42].

The principal goal of this thesis is to study whether squeezed light can improve the sensitivity of atomic sensors under optimal sensitivity conditions, typically in a high-density regime due to the statistical advantage of using more atoms. Indeed, to date squeezed-light optical magnetometers [40, 43, 44, 45] have shown reduction of the sensitivity by squeezing under certain, but *not optimal*, experimental conditions. The best reported sensitivity among the squeezed-light magnetometers is $1\,\mathrm{pT}/\sqrt{\mathrm{Hz}}$ [43], which is still three orders of magnitude worse than the state of the art sensitivity of sub-$\mathrm{fT}\sqrt{\mathrm{Hz}}$ [8, 9, 10]. Furthermore, the experiment by Horrom et al. [43] saw a complex and to-date unexplained behaviour:

by probing a polarized ensemble in a magnetometer based on nonlinear magneto optical rotation (NMOR), below the density that gives optimal sensitivity when a classical probe is used, squeezing reduced the measurement noise. In contrast, above that density, squeezing *increased* the measurement noise. At the optimum, the net effect was zero, to within the resolution of the measurement. A related experiment by Novikova et al. [45] demonstrated a strong coupling between the nonlinear magneto-optical rotation (NMOR) signal and optical quantum noise that introduces significant noise excess in the region where maximum sensitivity is expected. It is thus not obvious that squeezing will improve a high-density Faraday rotation measurement [24, 7], as it does for lower densities [39, 40].

In this thesis we describe two main experiments: first, we study application of squeezed light to spin noise spectroscopy of hot Rb vapor and we report quantum enhancement of the signal-to-noise ratio up to 2.6 dB by applying 3 dB of polarization squeezing of the probe over the full density range up to $n = 10^{13}$ cm^3, covering practical conditions used in optimized SNS experiments. Indeed, we show for the first time that squeezed light improves SNS over a broad atomic density and optical power ranges that include conditions used in state-of-the-art experiments [26, 46, 27, 47]. Differently from [43, 45] we deal with a un-polarized atomic ensemble and off-resonant probing, as required for a non-perturbative technique like spin noise spectroscopy. Furthermore, in our apparatus the source of squeezing is based on spontaneous parametric down-conversion (SPDC) in a non-linear crystal, while in [43, 45] an atomic squeezer based on polarization self rotation has been used. Our experimental results do not show any coupling between the optical and spin noise contributions so that squeezing reduces the measurement noise at both low and high densities. We also show that squeezing improves the trade-off be-

tween statistica sensitivity and broadening effects, a previously unobserved quantum advantage. Furthermore, we introduce a novel theoretical model by defining a standard quantum limit (SQL) for optically-detected noise spectroscopy, identified as a bound to the covariance of the parameters estimated by fitting power noise spectra. We test the model for spin noise spectroscopy of natural abundance Rb and we demonstrate experimental performance of SNS at the SQL. We further confirm the shot noise limitation to the sensitivity of the technique, by demonstrating parameter estimation below the SQL via polarization squeezing of the probe beam. In the second experiment we describe an optical magnetometer based on amplitude modulated optical rotation (AMOR), using a ^{85}Rb vapour cell, that achieves room-temperature sensitivity of $70\,\mathrm{fT}/\sqrt{\mathrm{Hz}}$ at $7.6\,\mu\mathrm{T}$ and we demonstrate its photon shot-noise-limited (SNL) behaviour from $5\,\mu\mathrm{T}$ to $75\,\mu\mathrm{T}$, making the system a promising candidate for application of squeezed-light to an optical magnetometer with best-in-class sensitivity.

1.2 Thesis Outline

This thesis is structured in the following way:

Chapter 2 provides the theoretical background for the whole thesis. First, within the scenario of optical interferometry, we define the fundamental limitation on the phase estimation, i.e. the photon shot-noise-limit (SNL), in presence of coherent states. Then, we introduce the theory of quadrature and polarization squeezing of light by showing its metrological advantage in phase estimation. Secondly, we review the concepts of linear and nonlinear magneto-optical effects by focusing on their application to spin noise spectroscopy, via paramagnetic Fara-

day rotation, and to optical magnetometry, through nonlinear magneto-optical rotation (NMOR). Finally, we define the fundamental limits of optical magnetometers.

Chapter 3 describes the design, construction and characterization of a versatile experimental setup for the study of atomic spectroscopy (and potentially magnetometry) in the presence of squeezed light. The apparatus combines a source of polarization squeezing with a conventional setup of spin noise spectroscopy of high-density Rb atoms. First, we describe the atomic system, the oven and its temperature stabilization. Then, we report the design and characterization of both the magnetic coils and the magnetic shielding. Finally we describe the generation and detection of polarization squeezing.

Chapter 4 describes the quantum enhancement of spin noise spectroscopy of a dense Rb vapor via polarization squeezing of the probe beam. We report the improvement of the signal-to-noise ratio of an amount comparable with the input squeezing of $\simeq 3$ dB over all the investigated parameter range. We also show that squeezing improves the trade-off between statistical sensitivity and broadening effects, a qualitative new quantum advantage. After introducing both the theory and the mode of operation, we describe the data analysis procedure and we report the experimental results.

Chapter 5 presents a novel theoretical model on the covariance matrix of the fit parameters in noise spectroscopy. We define a new kind of standard quantum limit (SQL) for the uncertainty on the fit parameters in the presence of optical shot noise and atomic spin noise. We compare the theoretical covariance matrix against data, from the experiment described in Chapter (4), and we find very good agreement by demonstrating spin noise spectroscopy at the standard quantum

limit. We also show the beating of the SQL by polarization squeezing of the probe, in agreement with theoretical expectations.

Chapter 6 describes a shot-noise-limited optical magnetometer with sub-picotesla sensitivity based on amplitude modulated optical rotation (AMOR). In this second experiment, carried out at the Jagiellonian University (Krakow) in collaboration with the group of Prof. Wojciech Gawlik, we report sensitivity of $\simeq 70\,\mathrm{fT}/\sqrt{\mathrm{Hz}}$, among the best reported sensitivities in the class of room-temperature low-frequency magnetometers, and SNL operation over a broad dynamic range ($5\,\mu$T to 75 μT) by making the described apparatus a promising candidate for application of squeezed light to a state-of-the-art optical magnetometer.

Chapter 7 summarizes the main results of the thesis and gives an outlook on future prespectives of the work.

Chapter 2

Theoretical background

In this chapter we provide concepts and references for the theoretical framework of the experiments presented in the Thesis. We first describe a general phase estimation process and we introduce the theory of polarization squeezing by focusing on its application to phase estimation. Then we give a schematic description of magneto-optical effects like linear Faraday rotation and nonlinear magneto-optical rotation (NMOR) and we describe their application in spin noise spectroscopy and optical magnetometry, respectively. Furthermore, we define the fundamental limits of optical magnetometers to which we will refer in chapter (6).

2.1 Phase estimation

In parameter estimation, a certain physical quantity of interest alters a property in the interaction between a probe input, known and previously prepared, and a system under investigation. Then, such physical parameter is (often) estimated

indirectly through the detection of the probe output after its interaction with the system. In optical interferometry the parameter estimation problem is translated into the measurement of a phase difference between either two optical paths (path interferometer) or two polarization components (polarization interferometer) and such measurement can be performed with very high sensitivity. However, because of the discrete nature of photons, quantum physics sets lower limits on the uncertainty in phase estimation, the so called shot-noise-limit (SNL), that turns to be fundamentally related to the uncertainty in photon number. Quantum metrology [48] uses quantum resources of both light and atoms to enhance precision in phase estimation beyond that possible through classical approaches.

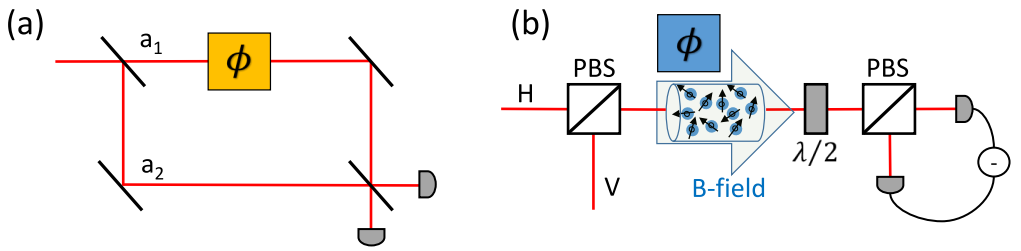

Figure 2.1: **(a)** Path interferometer in a Mach-Zehnder geometry. The relative phase between the interferometer arms a_1, a_2 is modeled by a phase shift ϕ in one arm. The intensity of each detector shows a sinusoidal dependence on the phase shift, so that uncertainty in intensity translates into an uncertainty in phase. **(b)** Polarization interferometer in which a relative phase shift ϕ between the H, V polarization components is imprinted onto the probe polarization by the interaction with an atomic ensemble in the presence of a nonzero magnetic field, i.e. by a magnto-optical effect (see Sections (2.3) and (2.4)). A polarimeter, that consists of an half wave-plate ($\lambda/2$), a polarizing beam splitter (PBS) and two photo-detectors allows one to reduce laser intensity and technical noise sources in the polarization rotation measurement (see Section 2.1.1).

The goal of this thesis is to apply squeezed light to high-precision measurements like spin noise spectroscopy and optical magnetometry, which use magnetically-sensitive atomic ensembles and optical read-out. These measurements can be understood as polarization interferometers in which the phase shift between two polarization components is imprinted onto the optical probe by the magneto-

optical interaction with a high density atomic vapor, as shown in Fig. (2.2 (b)). While the magneto-optical effects will be introduced in sections (2.3) and (2.4), in the following we describe the polarimetry detection scheme and the photon shot-noise contribution to the sensitivity of the phase estimation process.

2.1.1 Polarimetry detection

In the experiments described in this thesis, we use the detection scheme based on *balanced polarimetry*, which consists of a half-waveplate, a polarizing beam splitter (PBS) and two photo-detectors, whose signals are subtracted and the differential signal is further amplified to give the final output. For zero phase shift on the input probe polarization, a condition that corresponds in having the magnetic field turned off in our experiments, the polarimeter is fixed in the balanced condition by setting the half-waveplate at an angle of 22.5°, so that, after the splitting at the PBS, half of the photons (with +45° polarization) reach one detector while the second half (with −45° polarization) reach the second detector. The mean differential signal is then zero when no polarization rotation takes place and the laser intensity noise fluctuations, which affect the individual signals, are subtracted and cancelled through the difference operation. When the source of phase shift (for instance the magnetic field) is switched on, then the rotation signal is detected against a zero background and the optical rotation ϕ is given from a simple expression valid for $\phi \ll 1$ [6]:

$$\phi = \frac{I_{+45^\circ} - I_{-45^\circ}}{2(I_{+45^\circ} + I_{-45^\circ})} \tag{2.1}$$

where I_{+45° and I_{-45° are the optical intensities reaching the two detectors, respectively. The main benefit of the polarimetry detection, e.g. over absorption-based measurements, is the subtraction of technical noise due to laser intensity and polarization fluctuations that, in the balanced condition, affect both beams with the same noise amplitudes. However, shot-noise fluctuations intrinsically limit the sensitivity of the technique as we describe in the next section (2.1.2)). The other advantage of this setup is its insensitivity to circular dichroism, while the rotation signal can arise from linear dichroism (as in NMOR) or circular birefringence (as in normal and paramagnetic Faraday rotation). In section (3.3.2) we describe two different polarimeter schemes that we used in the experiment reported in chapter (4).

2.1.2 Phase estimation with coherent states

In the whole thesis we deal with quantum and technical noise contributions to the differential output signal of a balanced polarimeter and, when this is fed into a spectrum analyzer, to its power spectral density (PSD) in the frequency domain. In a polarization rotation measurement the output voltage of the polarimeter is simply given by:

$$V(t) = G i_{\mathrm{diff}}(t) \tag{2.2}$$

where G (V/A) is the transimpedance gain of the balanced detector and i_{diff} is the differential photo-current between the two photo-detectors. In the balanced condition, the rotation angle of Eq. (2.1) is $\langle\phi\rangle = 0$ and also the differential photo-current has zero mean value $\langle i_{\mathrm{diff}}\rangle = 0$. However fluctuations arise from different electronic, quantum and technical noise sources. It can be shown that, due to the discrete nature of photons and to the randomness in their time arrival

to the detector, the generated photo-current exhibits *shot noise* fluctuations given by the Schottky's formula [49]:

$$(\Delta i_{\text{diff}})^2_{\text{sh}} = (\langle i^2_{\text{diff}}\rangle - \langle i_{\text{diff}}\rangle^2)_{\text{sh}} = (\langle i^2_{\text{diff}}\rangle)_{\text{sh}} = 2q\langle i_{\text{diff}}\rangle\Delta\nu \tag{2.3}$$

where $q = 1.6 \times 10^{-19}$ C is the electron charge and $\Delta\nu$ is the detector frequency bandwidth. Then, still in the balanced condition, the photon shot-noise contribution to the output voltage is given by:

$$(\Delta V_{\text{sh}})^2 = \langle V^2\rangle = 2G^2q\langle i_{\text{diff}}\rangle\Delta\nu \tag{2.4}$$

which can be also expressed as a function of the mean optical power P that impinges the detector:

$$\langle V^2\rangle_{\text{sh}} = 2G^2q\Re P\Delta\nu \tag{2.5}$$

where $\Re = Qq/E_{\text{ph}}$ (A/W) is the detector responsivity, Q denotes its quantum-efficiency and $E_{\text{ph}} = \hbar\omega = 2.49 \times 10^{-19}$ J , in the experiments described in this work, is the photon energy at 795 nm. From Eq. (2.5) we can directly obtain the shot noise contribution to the one-sided power spectral density, which is given in units of V^2/Hz by

$$S_{\text{sh}}(\nu) = 2G^2q\Re P \tag{2.6}$$

and has the properties of being frequency independent (white noise) and scaling as the mean optical power P. Although we derived the shot noise from Eq. (2.3), which is valid in electronics for any current made of discrete charges with random fluctuations, it is worth to note that in photo-detection the shot noise is a consequence of the discrete nature of photons. For a coherent probe, the photon shot noise is due to the Poissonian statistics of the photon distribution

and can be derived with a quantum-mechanical approach in unit of photon number [50]. However, in the experiments presented in this thesis we work with bright coherent beams ($P \gg \mu$W) and continuous-time measurements, leading to a power noise spectrum for which the shot-noise expression given in Eq. (2.6) is more appropriate. Furthermore, the fluctuations of Eq. (2.4) set the photon shot-noise-limit (SNL) to the polarimetric sensitivity, which is expressed as uncertainty on the rotation angle of Eq. (2.1) and is given by [24]:

$$\delta\phi_{\mathrm{ph}} \approx \sqrt{\frac{\Delta\nu}{2N_{\mathrm{ph}}Q}} \tag{2.7}$$

where N_{ph} is the total number of photons per second reaching the polarimeter. Eq. (2.7) defines the photon SNL for a phase estimation process performed with coherent states.

As we will also show in this thesis, squeezed states of light, which exhibit sub-Poissonian statistics [51], allows one to perform sub-shot-noise measurements by reducing the shot noise contribution to the noise power density of Eq. 2.6 for coherent states, at same mean power, and, equivalently, to overcome the shot-noise-limited polarimetric sensitivity of Eq. (2.7) resulting in an improvement of the signal-to-noise ratio of the polarization rotation measurement. However, in order to perform quantum optics experiments and take advantages from the use of squeezing, the detection scheme of the specific experiment needs to be firstly limited by the photon-shot-noise. Indeed, our detection system (see section (3.3.2)) has electronic noise fluctuations approximately given by [52]:

$$(\Delta i)^2_{\mathrm{el}} = (\Delta i)^2_{\mathrm{amp}} + (\Delta i)^2_{\mathrm{fl}} \tag{2.8}$$

which is the sum of the *amplifier noise* $(\Delta i)^2_{\text{amp}} \approx 2qG\Delta\nu F$, where F is the so-called excess noise factor, and the $\approx 1/\nu$ *flicker noise* $(\Delta i)^2_{\text{fl}} = (K_I^2/\nu)\Delta\nu$ where K_I is the appropriate device constant in unit of A. The electronic noise is independent on optical power and it is a property of the overall detection system that consists of a balanced polarimeter and a spectrum analyzer. Here we neglect the *dark electronic noise* and *thermal (or Johnson) noise* [52] contributions, which are negligible in our balanced detectors. The first condition for the SNL operation mode is that the shot noise fluctuations should be much larger than the electronic noise: $(\Delta i)^2_{\text{el}} \ll (\Delta i_{diff})^2_{\text{sh}}$. Secondly, because of the imperfection of the balanced condition, residual technical noise due to laser intensity and polarization fluctuations, which power density scales as the mean power squared, needs to be smaller that the shot noise contribution. Then, the SNL frequency bandwidth and optical range of a detection system can be found by looking at the scaling of the power noise density as optical mean power at a given detection frequency. A full detailed quantum noise analysis of polarimetry detection is given in Section (6.6), where we define the experimental SNL condition for the detection stage.

2.2 Squeezed states of light

In the experiment described in chapter (4) we exploit polarization squeezing of the probe beam to beat the photon SNL polarimetric sensitivity resulting in quantum-enhancement of the signal-to-noise ratio of spin noise specroscopy of a hot Rb ensemble. As described in detail in chapter (3), we generate polarization squeezing by combining quadrature squeezed vacuum with an orthogonally polarized local oscillator bright beam. In the next section we briefly introduce the theoretical concepts of quadrature and polarization squeezing.

2.2.1 Quadrature squeezing

In its quantum description [50] the single mode electric field operator is described by the so-called quadrature field operators having a phase difference of $\pi/2$:

$$\hat{X_1} = \frac{1}{2}(\hat{a}^\dagger + \hat{a}) \qquad \hat{X_2} = \frac{i}{2}(\hat{a}^\dagger - \hat{a}) \tag{2.9}$$

where $\hat{a}$ and $\hat{a}^\dagger$ are the single mode annihilation and creation field operators. The quadrature operators, that can essentially be understood as dimensionless position and momentum operators [53], satisfy the commutation relation:

$$[\hat{X_1}, \hat{X_2}] = i/2 \tag{2.10}$$

Due to the generalized Robertson uncertainty relation [54], the variances of the quadratures are then bound by the relation:

$$\mathrm{var}(\hat{\mathrm{X}_1})\mathrm{var}(\mathrm{X}_2) \geq \frac{1}{4}|\langle[\hat{\mathrm{X}_1}, \hat{\mathrm{X}_2}]\rangle|^2 = \frac{1}{16} \tag{2.11}$$

where the variance of the operator $\hat{A}$ is defined as $\mathrm{var}(\hat{\mathrm{A}}) = \langle\hat{\mathrm{A}}^2\rangle - \langle\hat{\mathrm{A}}\rangle^2$. The coherent state is a minimum-uncertainty state for which $\mathrm{var}(\hat{\mathrm{X}}_1) = \mathrm{var}(\hat{\mathrm{X}}_2) = 1/4$ and the inequality of Eq. (2.11) becomes an equality. In contrast, a *quadrature squeezed* field state has the variance of one quadrature lower than a coherent state at the expense of a higher variance of the conjugate quadrature [53, 50]:

$$\mathrm{var}(\hat{\mathrm{X}_\mathrm{i}}) < \frac{1}{4} \qquad (\mathrm{i} = 1 \quad \text{or} \quad 2) \tag{2.12}$$

The quadrature squeezed state is obtained by applying the so-called squeezing operator [50]:

$$\hat{S}(\xi) = \exp[\frac{1}{2}(\xi^* \hat{a}^2 - \xi \hat{a}^{\dagger 2})] \tag{2.13}$$

where $\xi = se^{i\theta}$ is the complex squeezing parameter with amplitude $s \geq 0$ and phase $0 \leq \theta \leq 2\pi$. The squeezing operator creates and annihilates pairs of photons and can be described as a two-photon generalization of the displacement operator [50]. The *quadrature squeezed vacuum* state, that we experimentally generate through spontaneous parametric down conversion (SPDC) as described in chapter (3), is defined by $|\xi\rangle = \hat{S}(\xi)|0\rangle$ [50].

2.2.2 Polarization squeezing

As already mentioned, in the experiments described in this thesis the phase information is encoded in the probe polarization, so that we generate and detect squeezing in the polarization degree of freedom. A continuous variable description of the light polarization is obtained by defining the Stokes parameters:

$$\hat{S}_0 = \hat{a}_H^\dagger \hat{a}_H + \hat{a}_V^\dagger \hat{a}_V \tag{2.14}$$

$$\hat{S}_x = \hat{a}_H^\dagger \hat{a}_H - \hat{a}_V^\dagger \hat{a}_V \tag{2.15}$$

$$\hat{S}_y = \hat{a}_H^\dagger \hat{a}_V + \hat{a}_V^\dagger \hat{a}_H \tag{2.16}$$

$$\hat{S}_z = i(\hat{a}_V^\dagger \hat{a}_H - \hat{a}_H^\dagger \hat{a}_V) \tag{2.17}$$

where the subscripts H, V indicate horizontal and vertical polarization components [55]. Because of the bosonic commutation relations $[\hat{a}_j, \hat{a}_k] = \delta_{jk}$ with $j, k = H$ or V, the operator $\hat{S}_0$, that correspond to the total number of photons,

commutes with all the other Stokes operators:

$$[\hat{S}_0, \hat{S}_i] = 0 \qquad i = x, y, z \tag{2.18}$$

while the remaining operators satisfy the commutation relations of the SU(2) Lie algebra [56]:

$$[\hat{S}_i, \hat{S}_j] = 2i\hat{\varepsilon}_{ijk} S_k \qquad i, j, k = x, y, z \tag{2.19}$$

This noncommutativity precludes the simultaneous exact measurement of the Stokes operators and, analogously to Eq. (2.11) for the quadrature variables, their variances are related by uncertainty relations [56]:

$$\mathrm{var}(\hat{\mathrm{S}}_\mathrm{x})\mathrm{var}(\hat{\mathrm{S}}_\mathrm{y}) \geq |\langle \hat{\mathrm{S}}_\mathrm{z} \rangle|^2 \quad \mathrm{var}(\hat{\mathrm{S}}_\mathrm{y})\mathrm{var}(\hat{\mathrm{S}}_\mathrm{z}) \geq |\langle \hat{\mathrm{S}}_\mathrm{x} \rangle|^2 \quad \mathrm{var}(\hat{\mathrm{S}}_\mathrm{z})\mathrm{var}(\hat{\mathrm{S}}_\mathrm{x}) \geq |\langle \hat{\mathrm{S}}_\mathrm{y} \rangle|^2 \tag{2.20}$$

Analogously to quadrature squeezing, a state is *polarization squeezed* if:

$$\mathrm{var}(\hat{\mathrm{S}}_\mathrm{j}) < |\langle \hat{\mathrm{S}}_\mathrm{k} \rangle| \qquad \text{with} \quad \mathrm{j} \neq \mathrm{k} \tag{2.21}$$

which means that at least one Stokes operator has an uncertainty smaller than that of a coherent state with the same optical power. Experimentally, a polarization squeezed state can be generated by overlapping two quadrature squeezed states [56, 57] or by mixing a single quadrature squeezed state with a strong coherent beam (local oscillator - LO) with orthogonal polarization as in [37, 39]. In our experiment, as described in detail in chapter (3), we follow the latter approach by mixing a vertically polarized squeezed vacuum with a bright horizontally polarized LO. The combined state, at the output of a polarizing beam splitter, shows a strong horizontal polarization, i.e. $\hat{S}_x \approx \hat{S}_0$ with sub-shot noise (squeezed) quan-

tum fluctuations either in the $\hat{S}_y$ or $\hat{S}_z$ Stokes operator. Then, it is convenient to look at the squeezing behaviour in the $\hat{S}_y, \hat{S}_z$ plane by defining the operator $\hat{S}_\varphi = \hat{S}_y \cos\varphi + \hat{S}_z \sin\varphi$ with $\mathrm{var}(\hat{\mathrm{S}}_\varphi) = \langle \mathrm{N} \rangle$. This state is polarization squeezed if, for a certain relative phase φ, $\mathrm{var}(\hat{\mathrm{S}}_\varphi)$ is smaller than that of a coherent state.

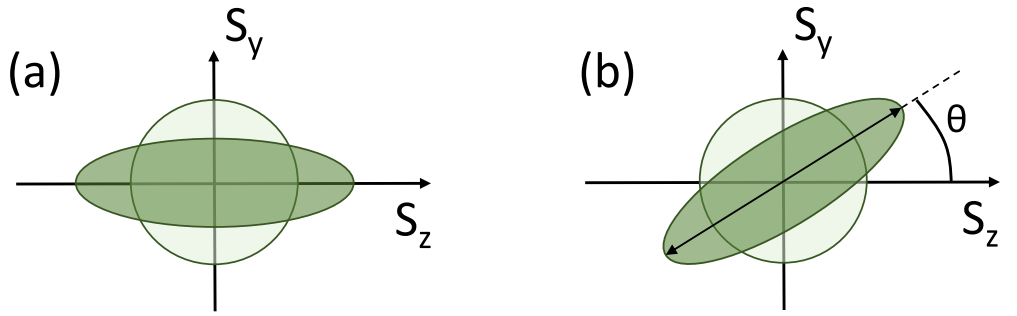

Figure 2.2: **Phase space representation of a polarization-squeezed state. (a)** The uncertainty area of a coherent state is represented by a circle (light green), while the uncertainty area of a polarization-squeezed state forms an ellipse (dark green). **(b)** The angle of the ellipse in the phase space θ is determined by the relative phase between local oscillator and squeezed vacuum (see text).

While the uncertainty area of a coherent state gives a circle in the phase-space diagram, the uncertainty area of a polarization squeezed state is visualized by an ellipse. Finally, so far we assumed a phase between the squeezed vacuum and the local oscillator (LO) fixed at $\theta = 0$. A change of this relative phase corresponds to a rotation of the polarization-squeezing ellipse in the $\hat{S}_y, \hat{S}_z$ plane [55]. In section (3.3) we describe the experimental generation and detection of this kind of polarization squeezing.

2.2.3 Phase estimation with squeezed states

If polarization squeezed light is injected into a polarization interferometer, the shot-noise level can be reduced or increased depending on the relative phase be-

tween the quadrature squeezed vacuum and the LO [37]. When the squeezing is locked to the minimum of the noise oscillations the phase estimation can be reduced below SNL. This can be shown at least in two ways. First, we note that the balanced polarimetry scheme described in section (2.1.1), when the half-waveplate before the PBS is set at an angle of 22.5°, corresponds to the experimental measurement of the $\hat{S}_y$ Stokes parameter, which is defined in Eq. (2.17) and can be expressed in terms of optical intensity operators as $\hat{S}_y = \hat{I}_{+45^\circ} - \hat{I}_{-45^\circ}$ [55]. The polarization rotation measurement can be written as [40]:

$$\hat{S}_y^{(\mathrm{out})} = \hat{S}_y^{(\mathrm{in})} + \hat{S}_x\phi \tag{2.22}$$

where $\hat{S}_x = \hat{I}_H - \hat{I}_V$ is the difference between the optical intensity with horizontal and vertical linear polarization of an input coherent beam, $\hat{S}_y^{(\mathrm{in})}$ and $\hat{S}_y^{(\mathrm{out})}$ are the input and output states of the $\hat{S}_y$ operator, while ϕ is the rotation angle defined in Eq. (2.1). In Eq. (2.23) we assume that the two contributions of the RHS are independent. Furthermore, we don't make any assumption on the nature of the rotation, but we just look at the noise properties. For an horizontal polarized coherent beam $\hat{S}_x$ is maximum and $\hat{S}_y^{(\mathrm{in})}$ is zero. Furthermore, for a zero mean rotation angle $\langle\phi\rangle = 0$, as in spin noise spectroscopy (SNS) (see chapter (4)), what we measure in the balanced condition is the variance:

$$\mathrm{var}(\hat{\mathrm{S}}_{\mathrm{y}}^{(\mathrm{out})}) = \langle(\hat{\mathrm{S}}_{\mathrm{y}}^{(\mathrm{out})})^2\rangle = \mathrm{var}(\hat{\mathrm{S}}_{\mathrm{y}}^{(\mathrm{in})}) + \mathrm{var}(\hat{\mathrm{S}}_{\mathrm{x}}\phi) \tag{2.23}$$

where the first and second terms of the RHS are the photon shot-noise and the atomic noise, i.e. the signal in SNS, contributions, respectively. In Eq. (2.23) we also assume that the detection is shot-noise-limited, i.e. that other noise contributions like electronic noise are much smaller than shot noise [40], as described

in section (2.1.2). Then, just by using the definition of Eq. (2.21), if the probe beam is polarization squeezed in the $\hat{S}_y^{(\mathrm{in})}$ operator, then $\mathrm{var}(\hat{\mathrm{S}}_{\mathrm{y}}^{(\mathrm{in})})_{\mathrm{sq}} < \mathrm{var}(\hat{\mathrm{S}}_{\mathrm{y}}^{(\mathrm{in})})$ and the noise of the measurement described by Eq. (2.23) is performed below the shot-noise-limit.

Another convenient way to look at the quantum noise suppression is the definition of a squeezing parameter $\xi^2 < 1$ [39] so that, the power noise density in presence of a polarization squeezed beam with $10\log(\xi^2)$ dB of squeezing is given by :

$$S_{\mathrm{sq}}(\nu) = S_{\mathrm{sh}}(\nu)\xi^2 \tag{2.24}$$

with a clear reduction of the shot noise density defined in Eq. 2.6. This notation will be used in chapter 4.

2.3 Linear magneto-optical effects

In the work described in this Thesis a phase shift is imprinted onto a linearly polarized probe beam by the interaction of light with an atomic ensemble in presence of a magnetic field i.e. by a *magneto-optical* effect. In the experiments reported in chapters (4) and (6) we exploit different magneto-optical effects where the polarization rotation shows *linear* and *nonlinear* dependence on the light field amplitude, respectively. Then, before introducing the concepts of nonlinear magneto-optics, we first review the basic physics of linear magneto-optics.

2.3.1 Introduction and background

During the second half of the 19th century Michael Faraday [1, 2, 58] discovered that linearly polarized light undergoes rotation of its polarization plane during the propagation through a medium placed in a magnetic field longitudinal with respect to the beam propagation direction. By using an oil lamp as light source and a dense leaded glass as atomic medium, Faraday was able to demonstrate that the angle of magneto-optical rotation ϕ is proportional to the applied magnetic field and to the length of the interacting medium:

$$\phi = \mathcal{V} l B \tag{2.25}$$

where $\mathcal{V}$ is the so-called Verdet constant that characterizes the ability of a medium to rotate the polarization plane. To give an example, typical commercial Faraday rotators or optical isolators, that are made of dense flint glasses, show linear rotation with a Verdet constant of $\mathcal{V} \simeq 3 \times 10^{-5}$ radG^{-1}cm^{-1}, while nonlinear optical rotation with $\mathcal{V} \simeq 3 \times 10^{4}$ radG^{-1}cm^{-1} can be observed in resonant alkali vapors [6]. Then, by considering the difference in density, an atomic vapor can be tought as a magneto-optical material with 10^{20} greater rotation "per atom" than heavy glass.

The resonant behaviour of the linear Faraday rotation was discovered at the end of the 19th century by the Italian physicists D. Macaluso and O.M. Corbino, who performed a series of experiments [59, 60] to study near resonance magneto-optical rotation in alkali vapors by selecting atom-resonant frequencies from sunlight through a diffraction grating. The results obtained by Macaluso and Corbino, in addition to the discovery of splitting of spectral lines in a magnetic field by Peter Zeeman [61, 62], led Woldemer Voigt [63] to explain the magneto-optical

rotation in terms of a difference in the refractive indices for the circular polarization components of the linearly polarized probe due to the Zeeman shifting of the medium spectral lines. Before starting with the formal theoretical treatment, we clarify that the linear magneto-optical rotation is called *Faraday effect* (or *Macaluso-Corbino effect* near resonance) when the magnetic field is longitudinal with the probe propagation direction, while it is called *Voigt effect* (in gases) or *Cotton-Mouton effect* (in liquids) if the applied field is perpendicular.

2.3.2 Faraday effect

The Faraday effect can be understood as a polarization interferometer where the input polarization is a liner combination of left (σ_+) and right (σ_-) circular polarization. If atomic anisotropy is generated (or naturally present) in the medium, then the two circular polarizations experience different dispersive and absorptive features resulting either in a rotation of the linear polarization plane or in change from linear to elliptical or circular polarization, respectively. In this thesis a rubidium vapor serves as anisotropic medium and the simplest transition in which magneto-optical rotation can be observed is the $F = 1 \rightarrow F' = 0$ system, where F and F' denote the total angular momentum of the ground and excited state, respectively. In such system, shown in Fig. (2.3) and usually described as Λ-system [6], the σ_+ component generates the transition from the ground state of $m = -1$ to the excited state $m' = 0$, where m and m' are the magnetic quantum numbers determining projections of the angular momentum on the quantization axis (beam propagation direction) for the ground and excited state, respectively. The σ_- component excites the transition $m = 1 \rightarrow m' = 0$, while the sublevel $m = 0$ is decoupled from light.

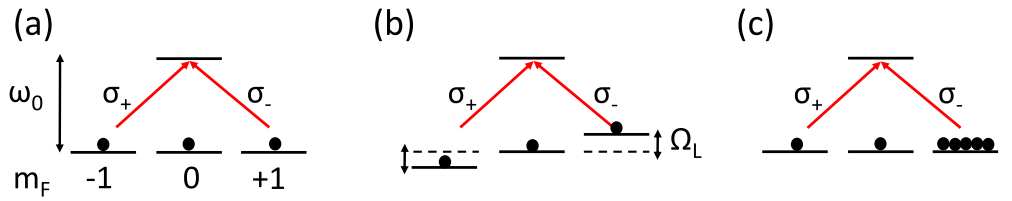

Figure 2.3: **(a) No Faraday effect.** Zero magnetic field condition, where the $\sigma_{\pm}$ polarization components have the same refractive index and there is no polarization rotation. **(b) Normal Faraday effect.** In presence of nonzero magnetic field, the Zeeman shift of the energy sub-levels causes a difference in the refractive index for $\sigma_{\pm}$ polarizations resulting in polarization rotation of a linearly polarized probe. **(c) Paramagnetic Faraday effect.** The isotropy of the medium is broken by population imbalance of Zeeman sublevels. For a thermal state, spin noise fluctuations can be measured as described in Section (2.3.4))

If no magnetic field is applied the atomic medium is isotropic as shown in Fig. (2.3 a), i.e. left and right polarization components have the same refractive index, the ensemble is in a thermal state and the mean polarization rotation is zero. Anisotropy can be induced by applying a nonzero magnetic field along the quantization axis (normal Faraday effect shown in Fig. (2.3 b)) or by a population imbalance of Zeeman sublevels (paramagnetic Faraday effect shown in Fig. (2.3 c)), generated by optical pumping [4]. Even for zero magnetic field and under thermal equilibrium (no optical pumping), intrinsic statistical fluctuations between Zeeman sublevels cause local instantaneous magnetization, i.e. spatial anisotropy, that turn into the so-called *spin noise* and such fluctuations can be mapped onto the probe polarization through Faraday rotation. The power spectrum analysis of these spin fluctuations is the core of the *spin noise spectroscopy* technique that we define in section (2.3.4) and we deeply investigate in chapters (4) and (5), with both coherent and polarization squeezed light probing.

We now provide an expression for the electric field intensity of a probe beam after Faraday interaction with an atomic medium. We consider the linear Faraday effect where a magnetic field B_z is applied along the z-direction of propagation

of a linearly polarized, monochromatic, weak-intensity probe beam. The electric field of the incident beam can be written as:

$$\mathbf{E}(0,t) = E_0 \mathbf{e}_\epsilon \cos \omega t \tag{2.26}$$

where the electric field vector $\mathbf{E}$, with amplitude E_0, oscillates in the x, y plane so that $\mathbf{e}_\epsilon = \mathbf{e}_x \cos\epsilon + \mathbf{e}_y \sin\epsilon$. The propagation through the atomic medium of length L can be described with the evolution of the circular polarization components $\sigma_\pm$ with amplitudes $A_\pm = A_\pm^r + iA_\pm^i$:

$$\mathbf{E}(z,t) = \frac{E_0}{2}(A_+ \mathbf{e}_+ e^{-i(\omega t - k_+ z)} + A_- \mathbf{e}_- e^{-i(\omega t - k_- z)} + c.c.) \tag{2.27}$$

where $\mathbf{e}_\pm = \mp\frac{1}{\sqrt{2}}(\mathbf{e}_x \pm i\mathbf{e}_y)$ and $k_\pm = \frac{\omega}{c}(n_\pm + i\alpha_\pm)$ are the wave numbers for the two $\sigma_\pm$ circular polarization components being $n_\pm$ and $\alpha_\pm$ the real and the imaginary parts of the refractive indices, respectively. In polarimetry detection the intensity measured after the polarizer depends on the relative angle between the probe output polarization direction ϵ and the polarizer angle θ:

$$I_\theta = (\mathbf{E}(L,t) \cdot \mathbf{e}_\theta)^2 \tag{2.28}$$

where $\mathbf{e}_\theta = \mathbf{e}_x \cos\theta - \mathbf{e}_y \sin\theta$. By inserting Eq. (2.27) in Eq. (2.28) we can evaluate the intensity transmitted by the polarizer [64]:

$$\begin{aligned} I_\theta &= \frac{I_0}{4}(e^{-2\alpha_+ \omega L/c} + e^{-2\alpha_- \omega L/c}) \\ &+ \frac{I_0}{2}\cos[2(\epsilon - \theta) + (n_+ - n_-)\frac{\omega L}{c}]e^{-(\alpha_+ + \alpha_-)\omega L/c} \end{aligned} \tag{2.29}$$

where I_0 is the incident intensity, ω is the angular frequency of the probe light.

By using the identities $\cos 2x = 1 - 2\sin^2 x$ and $\cos x = -\cos(x - \pi)$ Eq. (2.29) becomes:

$$\begin{aligned} I_\theta &= \frac{I_0}{4}(e^{-\alpha_+ \omega L/c} - e^{-\alpha_- \omega L/c})^2 \\ &+ I_0 \sin^2[(\epsilon - \theta - \frac{\pi}{2}) + (n_+ - n_-)\frac{\omega L}{2c}]e^{-(\alpha_+ + \alpha_-)\omega L/c} \end{aligned} \tag{2.30}$$

where the first term describes the differential absorption due to circular dichroism, sometimes called the parity nonconservation rotation [64], and the second term includes the Faraday rotation due to the difference in real part of the refractive index for the $\sigma_\pm$ circular polarization components with an overall absorption factor. Then, the dispersive Faraday rotation angle ϕ is given by:

$$\phi = (n_+ - n_-)\frac{\omega L}{2c} \tag{2.31}$$

2.3.3 Macaluso-Corbino effect

As first example, we now consider the Faraday rotation expression in the case of the Macaluso-Corbino effect (or normal Faraday effect). If we consider the Λ-type atomic system, introduced in section (2.3.2) and depicted in Fig. (2.3 (b), it can be shown [65] that, in the case of a narrow-band light interacting with motionless atoms and zero magnetic field, the complex refractive index $\eta = n + i\alpha$ is the same for the two circular polarization components and it is given by:

$$\eta \approx 1 + 2\pi\chi_0 \frac{1}{\Delta\omega + i\Gamma/2} \tag{2.32}$$

where $\Delta\omega = \omega - \omega_0$ is the light detuning, ω and ω_0 are probe and transition frequency respectively, Γ is the relaxation rate of the excited state and χ_0 is the

atomic linear susceptibility. When a nonzero magnetic field is applied along the quantization axis, the ground state Zeeman sublevels are shifted by the Larmor frequency $\Omega_L = g_F \mu_B B/\hbar$ where g_F is the Landé factor and μ_B is the Bohr magneton. As already mentioned, this turns into the modification of the refractive index for the $\sigma_\pm$ circular polarization components:

$$\eta_\pm \approx 1 + 2\pi\chi_0 \frac{1}{(\Delta\omega \mp \Omega_L) + i\Gamma/2} \tag{2.33}$$

By inserting the real part ($n_\pm$) of Eq. (2.33) into Eq. (2.31) we obtain the Macaluso-Corbino (or normal Faraday) rotation angle:

$$\phi \approx \frac{4\pi\chi_0\omega L}{c} \frac{\Omega_L(\Delta\omega^2 - \Gamma^2/4 - \Omega_L^2)}{[\Delta\omega^2 - \Gamma^2/4 - \Omega_L^2]^2 + \Gamma^2\Delta\omega^2} \tag{2.34}$$

Through the Larmor frequency expression, Eq. (2.34) shows that the rotation angle is a function of the applied magnetic field B and describes an example of an optical magnetometer based on the linear Faraday effect. Moreover, Eq. (2.34) is important for understanding the characteristic Lorentzian dependence (dispersion-like shape) of the rotation signal versus both magnetic field and frequency detuning. Indeed, the resonant dependence of the magneto-optical rotation is well visible: far from resonance there is no rotation, while for light tuned to an atomic transition the rotation is maximal.

Even if the Macaluso-Corbino effect is an important step for understanding application of linear Faraday rotation to optical magnetometry, we don't use it in this thesis. In the magnetometer described in chapter (6) we use *nonlinear* magneto-optical rotation (NMOR), described in section (2.4), which is rather based on linear dichroism (an absorptive effect) and provides much better sensitiv-

ity than the linear Faraday effect. On the other hand, in chapter (4) we deal with spin noise spectroscopy, which is based on a dispersive effect and it is introduced in the following.

2.3.4 Spin noise spectroscopy

Spin noise spectroscopy (SNS) is a non-perturbative approach that allows one to extract physical properties of both atoms [66] and semiconductors [25] from the power noise spectrum of the unperturbed spin system that, under thermal equilibrium, exhibits intrinsic spin fluctuations. These fluctuations between the different atomic levels generate instantaneous population unbalance that can be mapped onto the polarization of a probe beam via Faraday rotation. Then, the dispersive rotation is due to circular birefringence and has the form of Eq. (2.31). The probe beam is off-resonance in order not to perturb the system out of equilibrium. This is clearly different from conventional perturbative approaches like paramagnetic Faraday rotation where a non-equilibrium population distribution is generated through optical pumping [4]. In chapter (4) we describe SNS of natural abundance Rb and we demonstrate quantum-enhancement of the signal-to-noise ratio via polarization squeezing of the probe beam. We detect spin noise fluctuations in the so-called Voigt configuration [66], by applying a magnetic field transverse with respect to the probe propagation direction and by measuring the FR with a balanced polarimeter (see section (2.1.1)). In this configuration any random transverse fluctuation of magnetization will precess around the magnetic field direction at the Larmor frequency during the transverse relaxation time T_2 and then will be replaced by another fluctuating magnetization with different magnitude and phase of precession. As result, the probe beam undergoes random FR pro-

cesses at the Larmor frequency. The Voigt scheme is advantageous because, for large enough magnetic field ($B \geq \mu$T), the resonance frequency of the spin noise peak, in the power noise spectrum, is shifted far from the $1/\nu$ electronic (flicker) noise and also ends up in a more likely shot-noise-limted detection region. Indeed, this feature is also well-matched with atom-resonant squeezed light sources [67, 68, 69, 70, 71], which have shown squeezing at radio frequencies. While in chapter (4) we describe the experimental setup, the data analysis and the experimental results, here we derive the atomic spin noise contribution to the power spectral density for Rb in natural abundance.

Here we refer to the dispersive rotation angle of Eq. (2.31) with the notation $\phi = \Theta_{\rm FR}$. The following theoretical derivation has been obtained by my colleague Dr. Ricardo Jiménez-Martínez and it is also reported in [72]. We can compute the FR angle $\Theta_{\rm FR}$ by a coarse-grained approach. Dropping the t for simplicity, and labelling by i the isotope mass number and by j the hyperfine state, so that $f^{(i,j)}$ is the single-atom total spin quantum number, the contribution to $\Theta_{\rm FR}$ from atoms in a small region of dimensions $\Delta x \times \Delta y \times L_{\rm cell}$, centered on (x_m, y_m)

$$\Theta_{\rm FR}^{(i,j)} = \frac{1}{P}\frac{D_i(\nu')}{(2I_i+1)}\sum_m P(x_m,y_m)\frac{\sigma_0}{\Delta x \Delta y}F_z^{(i,j,m)}, \tag{2.35}$$

where $P(x_m, y_m) \approx \Delta x \Delta y \mathcal{I}(x_m, y_m)$ is the power of the beam in the given region, $2I_i + 1$ is a geometrical factor accounting for the hyperfine coupling between electronic spin ($S = 1/2$) and nuclear spin (I_i) of the atom, so that $f^{(i,j)} = I_i + j$, $j \in \{-\frac{1}{2}, +\frac{1}{2}\}$, and $F_z^{(i,j,m)}$ is the z-component of the collective angular momentum operator, i.e., the sum of the individual angular momenta $\mathbf{f}^{(i,j)}$ for atoms in the given region.

The on-resonance cross-section for the collision-broadened optical line is [73]

$$\sigma_0 = \frac{cr_e f_{osc}}{\Delta\nu_{light}/2} = 2.4 \times 10^{-12}\ \mathrm{cm}^2 \tag{2.36}$$

where $r_e = 2.82 \times 10^{-13}$ cm is the classical electron radius, $f_{osc} = 0.34$ is the oscillator strength of the D_1 transition in Rb, and c is the speed of light. The spectral factor is

$$D_i(\nu') = \frac{(\nu' - \nu'_j)\Delta\nu_{light}/2}{(\nu' - \nu'_j)^2 + (\Delta\nu_{light}/2)^2}, \tag{2.37}$$

where ν' and ν'_j, denote the probe optical frequency and optical resonance frequency, respectively, and $\Delta\nu_{light}$ represents the pressure-broadened FWHM of the optical transition. For the vapor cell used in our experiments $\Delta\nu_{light} \approx 2.4\,\mathrm{GHz}$ due to 100 Torr of N_2 buffer gas (see section (3.1.1)).

For a given region, the mean of the collective spin projection is $\langle F_z^{(i,j,m)} \rangle = n_i \Delta x \Delta y L_{cell} \mathrm{Tr}[\rho f_z^{i,j}] = 0$ where n_i is the atomic density of the i-th species, and ρ is the thermal state, which to a very good approximation is a uniform mixture of the ground states. As a result $\langle \Theta_{FR}^{(i,j)} \rangle = 0$.

In a similar way, and assuming that different atoms are independent, so that their variances sum, we find

$$\begin{aligned} \mathrm{var}\ \Theta_{FR}^{(i,j)} &= \left(\frac{\sigma_0}{P}\frac{D_i(\nu')}{(2I_i+1)}\right)^2 \mathrm{var} \sum_m \mathcal{I}(x_m, y_m) F_z^{(i,j,m)} \\ &\propto \sum_m \mathrm{var}\ \mathcal{I}(x_m, y_m) F_z^{(i,j,m)} \\ &\propto \sum_m \mathcal{I}^2(x_m, y_m) \mathrm{var}\ F_z^{(i,j,m)}, \end{aligned} \tag{2.38}$$

where var $F_z^{(i,j,m)} = n_i\,\Delta x\,\Delta y\,L_{\rm cell}{\rm Tr}[\rho(f_z^{(i,j)})^2]$, with

$$\mathrm{Tr}[\rho(f_z^{(i,j)})^2] = \frac{f^{(i,j)}(f^{(i,j)}+1)(2f^{(i,j)}+1)}{6(2I_i+1)}. \tag{2.39}$$

Taking the limit $\Delta x\Delta y \to dx\,dy$, and assuming the contributions of different isotopes and different hyperfine levels contribute independently, the spin noise due to isotope i is

$$\mathrm{var}\ \Theta_{\rm FR}^{(i)} = \kappa_i^2\sigma_0^2 n L_{\rm cell}\frac{\int dxdy\mathcal{I}^2(x,y)}{P^2}, \tag{2.40}$$

where the parameter κ_i^2 is given by

$$\kappa_i^2 \;=\; \sum_j \frac{D_i^2(\nu')}{(2I_i+1)^3}\frac{f^{(i,j)}(f^{(i,j)}+1)(2f^{(i,j)}+1)}{6} \tag{2.41}$$

Equation (2.40) is conveniently expressed as

$$\mathrm{var}\ \Theta_{\rm FR}^{(i)} = N_i\frac{\sigma_0^2}{A_{\rm eff}^2}\kappa_i^2, \tag{2.42}$$

where $N_i \equiv n_i A_{\rm eff} L_{\rm cell}$ is the effective number of istope-i atoms in the beam, and $A_{\rm eff}$ is the effective area [46]:

$$A_{\rm eff} \equiv \frac{[\int dxdy\,\mathcal{I}(x,y)]^2}{\int dxdy\,\mathcal{I}^2(x,y)}. \tag{2.43}$$

The spin noise oscillates at the Larmor frequency ν_i and with FWHM linewidth $\Delta\nu_i$, so that

$$S(\nu) = S_{\rm ph} + \sum_{i\in\{85,87\}} S_{\rm at}^{(i)}\frac{(\Delta\nu/2)^2}{(\nu-\nu_i)^2+(\Delta\nu/2)^2} \tag{2.44}$$

where

$$S_{\mathrm{at}}^{(i)}(\nu) = \frac{4G^2\Re^2P^2}{\pi\Delta\nu/2}\mathrm{var}\ \Theta_{\mathrm{FR}}^{(i)}. \tag{2.45}$$

gives, combined with Eqs. (2.41) and (2.42), the atomic noise contribution of the i-th species to the power spectral density of a Faraday rotation measurement, as a function of atomic density and optical detuning. The S_{ph} contribution to the spectrum is the photon shot noise power, which has been already defined in Eqs. (2.6) and (2.24) for a coherent and polarization squeezed probe, respectively. In chapters (4) and (5) we will refer several times to the theory introduced in this section.

2.4 Nonlinear magneto-optical rotation (NMOR)

After the discovery of the laser, it became possible to investigate magneto-optical effects within a regime of interaction between strong light fields and atomic media. Among different nonlinear processes [6], in 1974 a light intensity dependent Faraday rotation of the polarization plane, the so-called nonlinear magneto-optical rotation (NMOR), was discovered by W. Gawlik and co-workers [5, 74]. Nowadays, some of the most sensitive optical magnetometers are based on NMOR [75] and the narrowest feature in the magnetic resonance is related to the ground-state atomic coherence time, which can be increased when alkali vapours are confined with a buffer gas [76, 77] or in anti-relaxation coated cells [75, 78]. Techniques based on modulation in amplitude (AMOR) [79] or frequency (FM-NMOR) [80] of the pumping process, have extend the near-zero field NMOR high-sensitivity to a broader dynamic magnetic field range. In chapter (6) we report a shot-noise-limited AMOR magnetometer, with a complete description of both the experiment

and data analysis. In this section we qualitatively describe the physics of the AMOR process and we will refer to more complete references for a full theoretical treatment.

While the linear effects described in the previous section are understood in terms of circular birefringence induced either by Zeeman level shifts or by population unbalance between atomic energy sub-levels (as in SNS), nonlinear magneto-optical rotation is more properly explained in terms of probing the light-induced *linear dichroism* of a polarized atomic ensemble, which evolves in the presence of a magnetic field. Although the complete process is usually simultaneous, it is convenient to describe it as occurring in three stages: optical pumping, magnetic field dependent evolution (typically Larmor precession) of the atomic spin and optical probing.

As described in chapter (6) we perform AMOR-based magnetometry by means of amplitude modulated pumping and unmodulated CW probing in a right-angle geometry. Optical pumping with linearly polarized light generates spin alignment, i.e. ground state coherences between Zeeman sub-levels with $\Delta m_F = 2$ [81, 82]. In our experiment the pump beam is locked 20 MHz below the $F = 3 \rightarrow F' = 2$ transition of the ^{85}Rb D_1. The alignment describes a preferred axis, but not a preferred direction along this axis. In the saturated condition the medium becomes transparent to the linear polarization of the pump beam, while can still absorb light with orthogonal polarization, i.e. it acquires the property of linear dichroism. When a magnetic field is applied, the alignment axis precesses at the Larmor frequency Ω_L around the field direction and behaves like a rotating polaroid film [83] that is transparent to light polarized along its axis and slightly absorbent for the orthogonal polarization. The probe beam, which has

the same linear polarization of the pump and propagates along the magnetic field direction, is sensitive to alignment through linear dichroism, when the alignment is neither parallel to nor perpendicular to its polarization, and undergoes nonlinear magneto optical rotation (NMOR) of the polarization plane. As a function of the magnetic field, the NMOR resonance has a sub-natural linewidth equal to $\Gamma_{\rm rel}$, the relaxation rate of the ground state atomic coherence, that provides very high sensitivity of optical magnetometers [75], approaching fundamental limits as we also demonstrate in this thesis [84]. By considering that the aligned atomic state reproduces itself twice in a $1/\Omega_{\rm L}$ time, the NMOR signal also oscillates at $2\Omega_L$, and can be detected directly on a spectrum analyzer or demodulated with a lock-in amplifier to extract the in-phase and quadrature components, as described in chapter (6). In AMOR, amplitude modulated optical pumping at $2\Omega_L$ produces a resonant build-up of spin alignment, as demonstrated in several earlier works [85, 86]. The alignment now behaves as a damped driven oscillator, and in steady state responds at frequency Ω_m with an amplitude and phase relative to the drive that depend on the detuning $\Omega_m - 2\Omega_L$ [87], where Ω_m is the modulation frequency. Indeed, with CW pumping, as the magnetic field is increased the Larmor precession is faster, increasing the angle between the alignment axis and the probe polarization i.e. increasing the NMOR signal amplitude. When the Larmor precession starts to be much larger than the ground-state relaxation rate $\Omega_L \gg \Gamma_{\rm rel}$ the atoms can precess on the order of a full revolution before relaxing and, because of the continuous re-pumping in the same input polarization axis, the atomic polarization begins to average out reducing the signal that is eventually destroyed for CW pumping and strong magnetic fields. This explains the dispersive shape of the NMOR magnetic resonance [75] and the fact that, in order to get high sensitivity for larger magnetic fields, a synchronization of the pumping

process with the Larmor frequency is necessary [79]. In chapter (6)) we define the AMOR rotation signal and the AMOR sensitivity, we study the magnetometer quantum noise and we demonstrate SNL performance at the optimal sensitivity.

A rigorous theoretical treatment of nonlinear magneto-optical effects is quite complex, represents a subject in itself and goes beyond the objectives of this Thesis. The reader can refer to one of the more complete approaches [88], which makes use of the wave propagation equation for the optical field in the medium to relate the atomic density matrix with the changes in the light parameters. Another elegant method that allows one to make a systematic classification of both linear and nonlinear effects is the perturbative approach [6, 88], in which the density matrix is expanded in powers of the light electric-field amplitude.

2.5 Fundamental limits of optical magnetometers

As we described in the previous sections, by probing the magneto-optical evolution of an atomic medium, the polarization rotation signal is a function of the applied magnetic field. Then, in optical magnetometry [7] what is typically reported as *magnetometer sensitivity* is given by:

$$\delta B = \left(\frac{d\phi}{dB}\right)^{-1} \delta\phi \tag{2.46}$$

where $d\phi/dB$ is the slope of the rotation signal versus magnetic field and $\delta\phi$ is the uncertainty on the rotation angle i.e. the phase uncertainty in the polarization interferometer scheme. For near zero magnetic field the slope is given with a good approximation by the ratio $d\phi/dB \approx A/\gamma$ between the rotation signal amplitude A and the resonance width γ. Depending on the magnetometer scheme

and performance, different physical mechanisms affect the resonance linewidth; for istance, in NMOR-based magnetometry, as decribed in the previous section, the narrowest feature is related to the ground-state coherence relaxation rate $\gamma \simeq \Gamma_{\mathrm{rel}}$ so that increasing the coherence lifetime with noble buffer gas [77] or paraffine coated vapor cells [78] improves the magnetometer sensitivity. The amplitude of the rotation signal is proportional to the optical depth and can be improved either by increasing the atomic density or the light-atoms interaction length. The former is obtained by increasing the temperature of the vapor cell and consequently the atomic density (increasing the density has a limit when the dominant spin-relaxation mechanisms becomes either spin-exchange or spin-destruction collisions [89]). The latter is obtained either by using longer vapor cells or through multi-pass vapor cells [10], in which the light probe is reflected hundreds times back and forward before detection, resulting in a significant enhancement of the signal [90]. From Eq. (2.46) it is also evident that a reduction in the phase uncertainty turns into an improved sensitivity. However, the magnetometer sensitivity of Eq. (2.46) is fundamentally limited by two independent quantum noise contributions δB_{at} and δB_{ph}, arising from the quantum nature of both atoms and photons, respectively. The quantum limited sensitivity is given by [7, 89]:

$$\delta B_{ql} = \sqrt{\delta B_{\mathrm{at}}^2 + \delta B_{\mathrm{ph}}^2} \tag{2.47}$$

It should be noted that light-atom coupling via AC Stark shifts can also be a source of additional quantum noise [91].

2.5.1 Atomic projection noise

The atomic contribution, the so-called *spin-projection-noise* (or *atomic shot-noise*) limit is due to the fundamental quantum uncertainty on the measurement of atomic spin projection along a certain axis and, for a measurement time $\tau \gg \Gamma_{\mathrm{rel}}$, it is determined by the total number of atoms N involved in the measurement and by the spin-relaxation rate Γ_{rel}:

$$\delta B_{\mathrm{at}} \approx \frac{\hbar}{g_f \mu_B} \sqrt{\frac{\Gamma_{\mathrm{rel}}}{N\tau}} \tag{2.48}$$

This quantum limit can be understood by considering that a measurement performed with a single atom for a time of $1/\Gamma_{\mathrm{rel}}$ gives a precession angle uncertainty of 1 rad. Using N atoms results in an uncertainty reduction by $\sqrt{N}$, while repeating the measurement multiple times further reduces the uncertainty by the number of measurements that is approximately equal to $\sqrt{\Gamma_{\mathrm{rel}}\tau}$. In different magnetometer schemes, the atomic shot-noise of Eq. (2.48) can be beaten by using either atomic entanglement [92] or atomic spin squeezing [93, 94]. However, as already mentioned, in this thesis we focus on the opportunities given by the polarization squeezing of the light, that can analogously beat the photon shot-noise-limited magnetometer sensitivity, which is defined below.

2.5.2 Photon shot noise

As already described in Section (2.1.2), within a general interferometer scheme, the uncertainty of the phase estimated with coherent states is limited by the photon-shot-noise of Eq. (2.7). By inserting the photon shot noise scaling in Eq. (2.46) we can obtain the quantum noise contribution to the magnetometer

sensitivity [95]:

$$\delta B_{ph} \approx \frac{\hbar}{g_f \mu_B} \frac{\Gamma_{\mathrm{rel}}}{A} \frac{1}{\sqrt{N_{\mathrm{ph}}}} \tag{2.49}$$

When optical magnetometers are limited by the photon shot noise, it is possible to improve the sensitivity below the shot-noise limit of Eq. (2.49) by using squeezed states of light, as described in Section (2.2.3). Application of polarization squeezed-light improved the sensitivity of optical magnetometers up to the level of $\approx 1\,\mathrm{pT}/\sqrt{\mathrm{Hz}}$ [40, 43, 44, 45], still much worse than state of the art sensitivity [8, 10] in the class of low-frequency scalar magnetometers. In chapter 6 we report the first shot-noise-limited optical magnetometer that is suitable for application of squeezed light and, at the same time, has a sensitivity of $70\,\mathrm{fT}/\sqrt{\mathrm{Hz}}$, comparable with the best in class optical magnetometers.

Chapter 3

Experimental setup for squeezed-light atomic spectroscopy

In this chapter we describe in detail the experimental setup that we built at ICFO during my PhD, together with my colleagues Jia Kong and Ricardo Jiménez-Martínez. The setup combines a source of polarization squeezed light with a dense atomic ensemble within a low-noise magnetic environment. While the squeezer was already built [69] and used in previous experiments within our group [40, 96], my work has been focused on the design and building of the apparatus, which consists of vapor cell, oven, heating system, magnetic coils for both uniform and gradient fields and on the study of its interaction with a squeezed light probe. The combined experimental setup is a versatile system for studying quantum effects and limitations of atomic spectroscopy and magnetometry at the picotesla

level of sensitivity with atomic density up to $n = 10^{13}$ atoms/cm^3, while the use of squeezed light can beat the classical limitation to sensitivity given by the photon shot-noise contribution. This chapter 3 gives all the technical details and calibrations of the different components of the apparatus. As first application, we report quantum enhancement of spin noise spectroscopy of dense Rb ensemble using squeezed light, an experiment described in Chapter 4.

3.1 Atomic system and temperature control

In this section we describe the characterization of the Rb vapor cell and the design/construction of the aluminium oven that encloses the vapor cell. We also give all the technical details regarding the heating system and the temperature control.

3.1.1 The vapor cell

Figure 3.1: **Rb Vapor cell**.

In our experiment we used a cylindrical vapor cell (Manufacturer: Precision

Glassblowing) with natural isotopic abundance of ^{85}Rb and ^{87}Rb. The cell, shown in Fig. 3.1, has length of $L_{\text{cell}} = 3$ cm, diameter of $d = 1.27$ cm and fused silica windows with length of $L_{\text{win}} = 3$ mm each and double-side antireflection (AR) coating for 795 nm. In order to increase the atomic spin lifetime, in addition to 25mg of Rb the cell is filled with 100 Torr of N_2 buffer gas. We checked the amount of buffer gas by measuring the absorption spectrum versus detuning of a probe laser. In Fig. (3.2) we report the absorption spectra for the cell with buffer

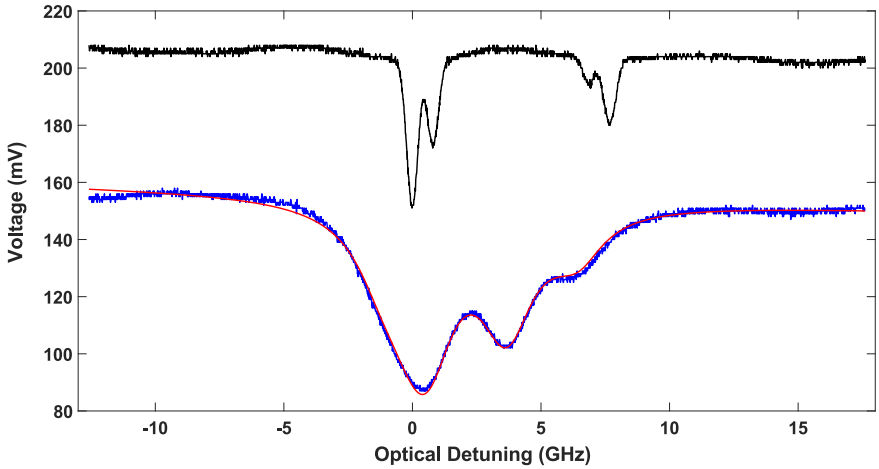

Figure 3.2: **Absorption vs frequency detuning**. Measured absorption spectrum of the cell with buffer gas is in blue, while the performed fit (see text) is in red. A reference spectrum (87Rb isotopically pure cell with no buffer) is in black. The light detuning on the x-axis is measured with respect to the hyperfine transition $F_g = 2 \rightarrow F_e = 1$ of ^{87}Rb D_1 line.

gas and for a reference cell of pure ^{87}Rb. In general, the intensity of a laser beam after absorption through a cell of length L_{cell} with isotopic abundance is given by:

$$I = I_0 \exp[-(\sum \alpha_i) L_{\text{cell}}] \tag{3.1}$$

where I_0 is the beam intensity at the entrance of the medium, the sum is performed over all the available transitions for all the isotopes and α_i is the absorption

coefficient of the individual transition for each species. In our specific case, shown in Fig. (3.2), the laser frequency is scanned around the Rb D_1 line (zero reference at the transition $F_g = 2 \rightarrow F_e = 1$ of ^{87}Rb), there are four available D_1 line transitions for both ^{85}Rb and ^{87}Rb isotopes with transition strengths given in the Appendix B of [97]. By knowing that the D_1 line is significantly broadened by atomic collisions with buffer gas atoms, we neglect the effect of Doppler broadening so that the absorption coefficient for the transition $F \rightarrow F'$ of the isotope with abundance Is can be written as $\alpha_i = \mathrm{OD/L_{cell}} \times \mathrm{Is} \times \mathrm{S_i(F, F')L_i}(\nu)$ in which OD is the optical depth and $L_i(\nu)$ is a pure Lorentzian function given by:

$$L_i = \frac{\gamma^2/4}{(\nu - \nu_{\mathrm{coll}} - \nu_i)^2 + \gamma^2/4} \tag{3.2}$$

where γ is the FWHM pressure-broadened linewidth, ν_{coll} is the transition frequency shift due to collisions with the buffer gas, $S_i(F, F')$ and ν_i are transition strength and detuning of the $F \rightarrow F'$ transition relative to the reference transition $F_g = 2 \rightarrow F_e = 1$ of ^{87}Rb D_1 line, respectively. Then, in order to obtain the experimental values of γ and ν_{coll}, we perform a fit (see Fig. (3.2)) of the measured absorption spectrum (in Volt units) with the fit function:

$$V(\nu) = A + B\nu\left(\exp\Big[-\mathrm{OD}\Big(0.7217\sum_{\mathrm{i}}\mathrm{S_i(F, F')L_i}(\nu) + 0.2783\sum_{\mathrm{j}}\mathrm{S_j(F, F')L_j}(\nu)\Big)\Big]\right) \tag{3.3}$$

in which A is an offset, B takes into account the laser intensity dependence on optical frequency, i and j indices run over the four available transitions for ^{85}Rb and ^{87}Rb, respectively. From the fit with free parameters $(A, B, \mathrm{OD}, \gamma, \nu_{\mathrm{coll}})$ we obtained an optical linewidth $\gamma = 2.29$GHz, a collisional shift $\nu_{coll} = -1.19$GHz and an optical depth OD = 1.1. By considering that $\mathrm{OD} = \sigma \mathrm{nL_{cell}}$, the mea-

sured pressure broadened cross section is $\sigma = 2.4 \times 10^{12}$ cm^2 and $L_{\text{cell}} = 3cm$, the described measurement gives also an atomic density value of $n = 2 \times 10^{11}$ atoms/cm^3. The measured values of linewidth and shift due to collisions with buffer gas atoms are in good agreement with theoretical expectations based on [98] (broadening of 2.3GHz and shift of -1GHz) for a buffer gas pressure of 100 Torr.

3.1.2 Oven

The vapor cell is enclosed in an aluminium oven that, thanks to high thermal conductivity $k_T \approx 200\text{Wm}^{-1}\text{K}^{-1}$, is heated up through conduction with a heating circuit that we describe in detail in the next section (3.1.3). The oven constists

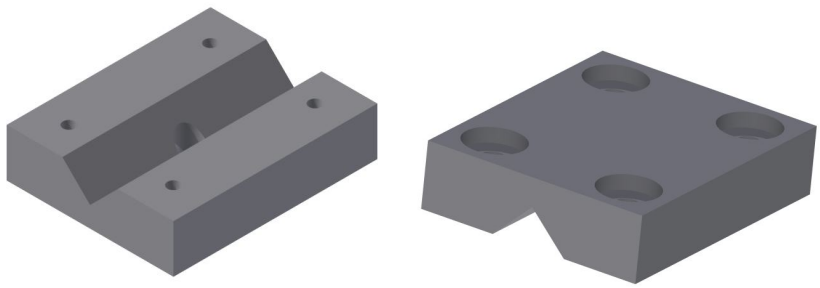

(a) Oven bottom part (b) Oven top part

Figure 3.3: Aluminium Oven design pictures.

of two independent parts of length $l = 5.5$cm and width $w = 4.5$cm, machined by the ICFO mechanical workshop, that are shown in Figs. (3.3a) and (3.3b). The technical drawings, including holes dimensions, are reported in the Appendix. Both parts of the oven are machined with a v-groove structure, so that the vapor cell can stay in mechanical equilibrium over the bottom part, as shown in Fig. (7.2), while the top part is attached to the first through non-magnetic screws, in

order to surround the cell volume and to keep, at the same time, free space for transverse and longitudinal laser beam propagation. The cell's stem goes through a hole, machined at the center of the bottom part of the oven, as shown in Figs. (3.3a) and (7.2).

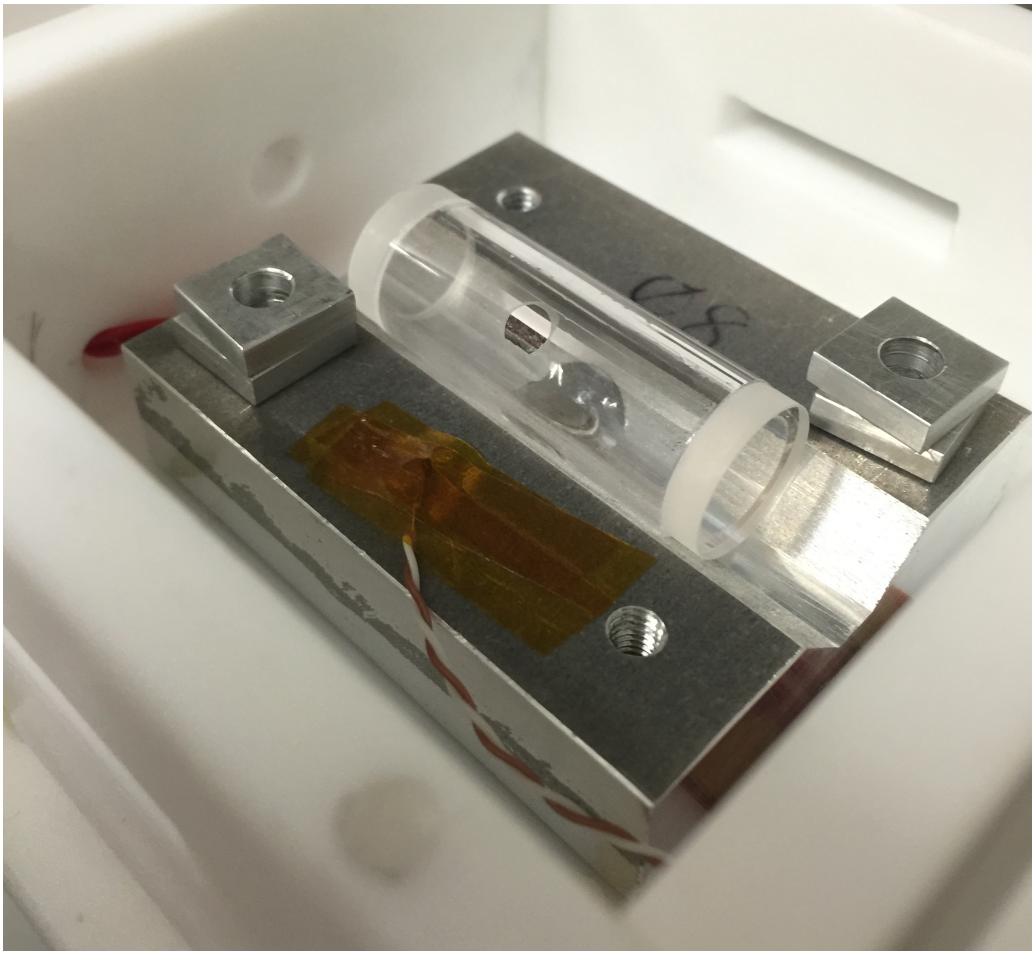

Figure 3.4: **Aluminium oven**. Top view of the vapor cell over the bottom part of the aluminium oven. The combined system is thermally isolated by a Teflon box. A thermocouple sensor is attached to the oven through Kapton tape and it monitors the temperature as described in Section (3.1.3).

The system composed by the aluminium oven and the Rb vapor cell is thermally isolated from the environment by means of a Teflon box connected to rings

that are machined in order to fit inside the innermost acrylic tube of the overall apparatus, described in section (3.2). In Fig. (3.5a) we report the picture of the system that includes the Teflon box (open in the photograph), the aluminium oven and the vapor cell. The Teflon box is machined with longitudinal holes of diameter $D = 1$cm (side view in Fig. 3.5c) and transverse windows (side view in Fig. 3.5d) to enable laser propagation in both directions. In addition, as shown in Figs. (3.5a), transverse holes allow the wires, of both thermocouple and heaters, to be passed out of the oven for electrical connections. In the experiment described in Chapter 4, carried out with this apparatus, the Rb vapor is in thermal equilibrium (no optical pumping) and we probe the atoms just with a single laser beam in the longitudinal direction (coordinate system defined in Section 3.2).

3.1.3 Heating circuit and temperature stabilization

The density of the Rb vapor is increased by heating up the aluminium oven that surrounds the cell. The heating system is shown in Fig. (3.6). A tranformer reduces the 250 VAC from the laboratory power line to a lower voltage of 115AC Volt that is applied to a load of five Katpon heaters connected in series. Each heater (Model: KHLV-101/(10) from Omega) has area of 1in^2, impedance of 83.6Ω and is specified for power up to 10 Watt/in^2. Then, when a 115 VAC is applied to the load, a total electrical power of 25W is released. Four out of five heaters are placed underneath the aluminium oven (See Fig. 3.5a) and they are overlapped in pairs, so that the current in the top heater flows in the opposite direction with respect to the bottom one and the residual generated magnetic fields are mutually cancelled, as shown in Fig. 3.7. A fifth heater is also wired in series to the first four but it is outside of both the oven and the magnetic shielding, so that it com-

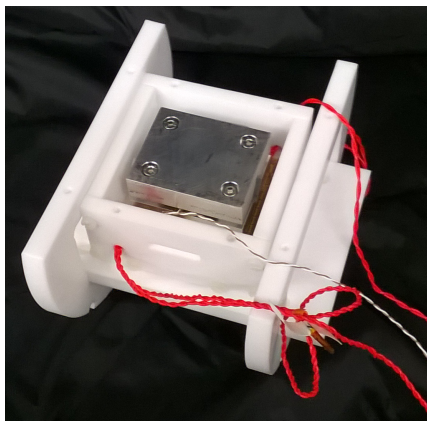

(a) Aluminium oven inside the Teflon box

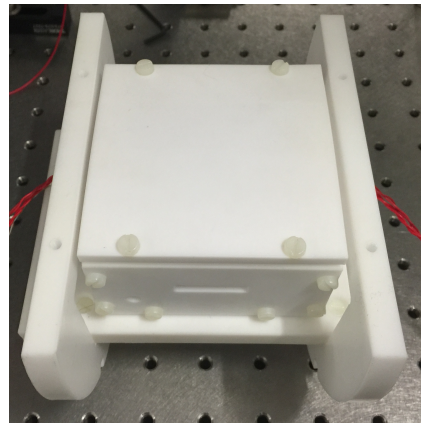

(b) Top view

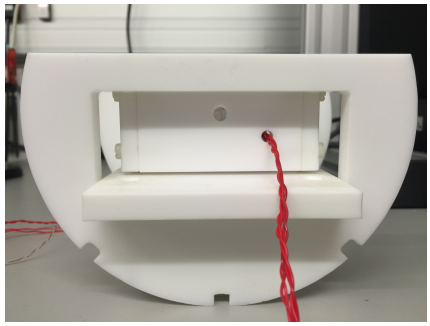

(c) Longitudinal side view

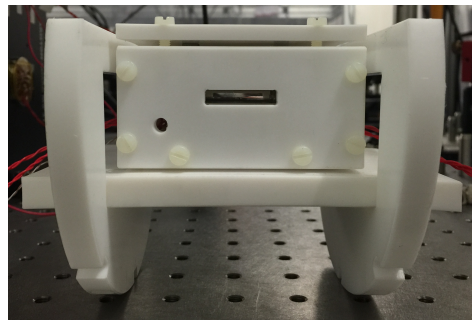

(d) Transverse side view

Figure 3.5: **Teflon box for thermal isolation**. The aluminium oven that encloses the vapor cell is attached to a Teflon box for thermal isolation and supported by Teflon rings.

pletes the circuit's load but does not contribute to the oven/vapor cell heating, as depicted in Fig. (3.6). The temperature inside the oven is monitored by a type-T thermocouple (Model: CT-Z2-PFA-T-2 from LabFacility) that is attached to the oven at the height of the probe beam propagation through the vapor cell (see Fig. 7.2). The thermocouple voltage output is electrically connected to a PID feedback/control circuit of a digital temperature controller (Model: CN9111A from Omega) that alternatively switches ON/OFF a relay output allowing to the 115 VAC to be applied or not to the circuit load, in order to reach the temperature

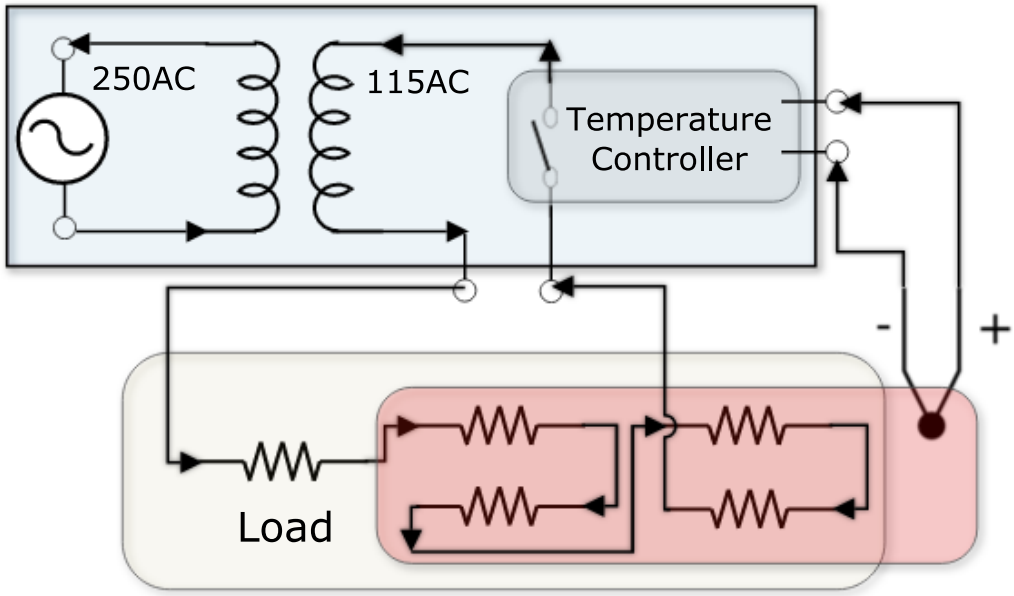

Figure 3.6: **Heating Circuit**. The heating system consists of a transformer, a load of five Kapton heaters, a thermocouple sensor and a temperature controller (see text for details). The rows indicate the direction of the current's flow. The blue region includes components that are inside an isolation box made of aluminium with electrical input (to the temperature controller) and output (to the load circuit) for the thermocouple and the 115AC voltages, respectively. The yellow region includes the circuit load. The red region encloses the components (four heaters and thermocouple's sensor) that are in thermal contact with the aluminium oven, inside the magnetic shielding within a Teflon isolation box. A fifth heater is outside of the magnetic shielding and it is used both as a monitor of the proper operation of the circuit and as a source (from its extremes) of a trigger voltage for the data acquisition.

setpoint and/or to keep it stable. As shown in Figs. (3.8a) and (3.8b), by using the described heating system the temperature reaches the setpoint from five to ten minutes, the higher the temperature the longer the stabilization time, and afterwards remains stable within a $\pm 1°C$ uncertainty. While we tested temperature up to 180°C, in the main experiment described in Chapter 4 we heated the vapor cell up to 120°C. Under stable conditions, the current flows into the circuit, through the relay control, one second over ten, the 10% of the time. The accessible kapton heater outside the shielding, is used both as a safety monitor and, most

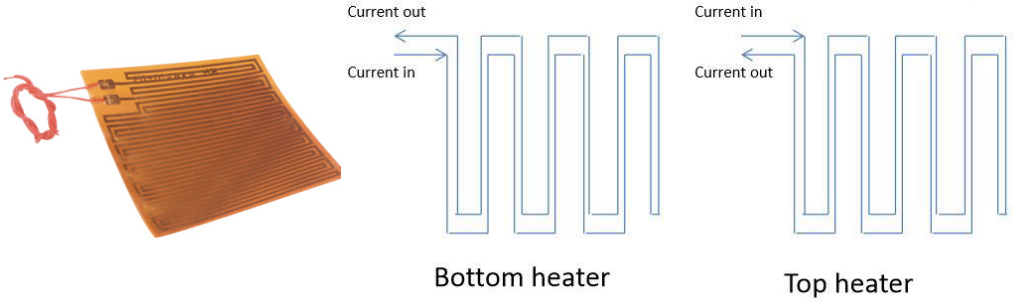

Figure 3.7: **Kapton heater**. The four heaters are in thermal contact with the bottom part of the aluminium oven, they
are connected in series and overlapped in pairs with opposite current flow, as depicted here, in order to minimize residual magnetic fields.

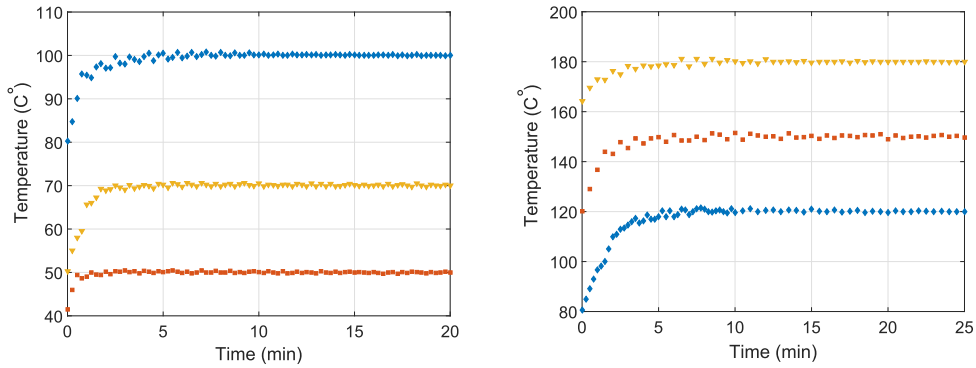

(a) Low Temperature Stabilization (b) High Temperature Stabilization

Figure 3.8: Temperature versus time.

importantly, as a trigger for the data acquisition. In fact, we take the voltage across the heater in order to generate a signal that trigger the data acquisition while no current flows through the heaters.

3.2 Magnetic shielding and magnetic coils

Magneto-optical effects, like Faraday rotation, are at the core of atomic measurements as those described in this Thesis like spin noise spectroscopy and optical

magnetometry. Then, a very low-noise magnetic environment is required in order to reach quantum-limited sensitivity of such atomic sensors. In this section we describe the geometry and the characterization of the magnetic shielding, necessary to achieve the picotesla level of sensitivity, and we give all the details on design, construction and calibration of the magnetic coils for the generation of both uniform and gradient magnetic fields.

3.2.1 Magnetic Shielding

In the apparatus we built at ICFO, the atomic system and the magnetic coils, that we describe in the next subsection (3.2.2), are magnetically shielded from the environment (mainly from the Earth's magnetic field) through four cylindrical mu-metal layers whose diameters and thickness are given in Table (3.1) (Manufacturer: magneticshields.uk). The main figure of merit here is the magnetic shielding factor $S = B_{ext}/B_{int}$, which is defined as the ratio of the magnetic field B_{ext} applied to a certain volume in absence of magnetic shielding to the field B_{int} measured inside the shielded volume. An estimate of the total shielding factor of a series of n shield layers can be found by using the simple approximate expression [99]:

$$S_{tot} = S_n \prod_{i=1}^{n-1} S_i \Big[1 - \Big(\frac{D_i}{D_{i+1}}\Big)^k\Big] \tag{3.4}$$

where D_i is diameter of the ith shielding layer and k depends on the shield geometry: $k = 3$ for spherical shells, $k = 2$ for cylindrical layers as in our case. The individual layer shielding factor is given by:

$$S_i = \mu_i t_i / D_i \tag{3.5}$$

where μ_i, t_i and D_i are magnetic permeability (relative to the free space) and thickness of the ith shielding layer.

Shield parameters			Estimated Shielding			Measured Shielding	
i	D_i (mm)	t_i (mm)	$\mu = 10^4$	$\mu = 2 \times 10^4$	$\mu = 10^5$	DC	AC
1	203.2	1.5	74	148	738	179	115
2	254	1.5	59	118	591	104	43
3	304.8	1	33	66	328	337	127
4	355.6	1	28	56	281	120	67
Total Shielding S_n ($\times 10^6$)			0.1	1.9	1173.8	22	1.2

Table 3.1: **Magnetic Shielding** In this table we report the geometrical parameters of the mu-metal layers together with the individual and overall shielding factor, both estimated and measured.

In Fig. (3.9) we report the scheme used for measuring the shielding factor for AC/DC applied magnetic field. We applied a known magnetic field to the center of the volume of the individual shielding layer. By means of a fluxgate magnetometer with 10 pT sensitivity (Model: Mag-03 MCUP range 100 from Bartington Instruments) we measured (see caption of Fig. (3.9) for details) the generated field B_{ext} in absence of the shielded volume and the field B_{int} inside the cylindrical layer at the same position. Thus we obtained the shielding factor S_i of the individual mu-metal layer. By comparing the measured shielding factors with the theoretical values given by Eqs. (3.4) and (3.5), we found a good agreement for values of magnetic permeability that vary for different layers from 1.7×10^4 to 1×10^5 for an applied DC B-field and from 7.2×10^3 to 3.8×10^4 for an applied B-field oscillating at 72 Hz. Form this, we infer an averaged magnetic permeability values of $\mu = 4.5 \times 10^4$ and $\mu = 1.95 \times 10^4$, respectively. By inserting the measured shielding factors (see Table (3.1)) in Eqs. (3.4) and (3.5) we obtain a total magnetic shielding factor of $S_{tot} = 2.19 \times 10^7$ and $S_{tot} = 1.2 \times 10^6$ for the DC/AC case, respectively. Then, the contribution from the Earth's magnetic field

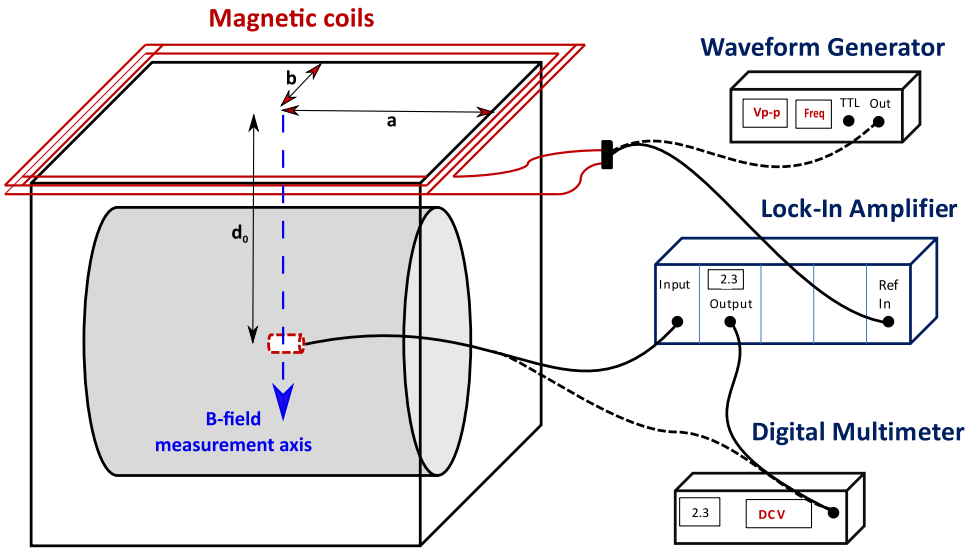

Figure 3.9: **Shielding factor measurement scheme**. We apply a known voltage to a set of rectangular coils from the output of a Waveform Generator/Lock-in-amplifier (LIA) for generating a DC/AC magnetic field, respectively. By knowing coils geometry (a, b), applied voltage and coils impedance we calculated the generated field at a distance d_0 from the center of the rectangular coils, in free unshielded space, through the law of Biot-Savart. We found good agreement with the experimental value B_{ext}, measured by means of a fluxgate magnetometer along the axis of the generated field (blue dashed line). The fluxgate output is fed into a digital multimeter directly in the DC case, after demodulation by the LIA (at the same 72Hz reference frequency) in the AC measurement. We then placed the individual shielding layer, we measured the field B_{int} at the same position inside the shielded voulme and we obtained the shielding factor $S = B_{ext}/B_{int}$. We followed the same procedure for the four individual layers by obtaining experimental values given in Table (3.1).

$B_E \approx 50\mu T$ (or other field of similar strength outside the shielding) is shielded to the uniform level of $B_E/S_{tot} = 2.27$pT.

Each mu-metal layer consists of a tubular body with transverse holes (designed for transverse laser beam propagation) and two endcaps, attachable and removable by friction, with three holes designed for the longitudinal propagation of a laser beam and for allowing the wires (of both coils and heating system) to go through, as shown in Fig. (3.10a). The overall magnetic shielding stands

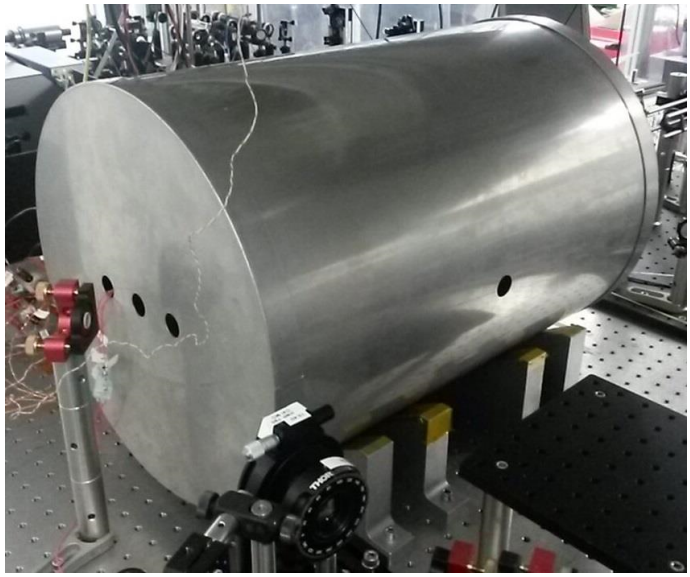

(a) **Magnetic shielding**. Overall mu-metal magnetic shielding with cylindrical body and endcaps. The holes allow transverse and longitudinal propagation of laser beams.

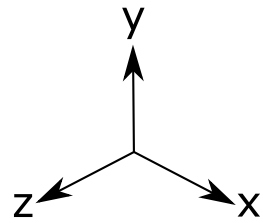

(b) **Coordinate system**.

Figure 3.10: Magnetic shielding and coordinate system. The zero position (0,0,0) corresponds to the geometrical center of the cylindrical vapor cell as well as of the tubular shielding. See also Fig. 3.15b.

in mechanical equilibrium over four aluminium mounts that are screwed to the optical table. In this way the entire system is stable in a fixed position, but could also be moved easily to another region of optical table. In Fig. (3.10b) we define the coordinate system where the z direction corresponds to the laser propagation direction through the Rb vapor cell while the (0,0,0) position corresponds to the geometrical center of both the vapor cell and the magnetic shielding. We will refer to this coordinate system in the next section as well as throughout the whole Thesis.

3.2.2 Uniform fields and gradient Coils

In order to make our setup versatile for different experimental configurations, we have designed and built different coil geometries for generating uniform magnetic fields and gradients in the three spatial directions. By referring to the coordinate system of Fig. (3.10b), in our apparatus, inside the magnetic shielding, we can apply to the region covering the vapor cell volume the three DC fields:

$$\Big\{B_x, B_y, B_z\Big\} \tag{3.6}$$

and their respective gradients with respect to the probe propagation direction z:

$$\Big\{\frac{\partial B_x}{\partial z}, \frac{\partial B_y}{\partial z}, \frac{\partial B_z}{\partial z}\Big\} \tag{3.7}$$

Coils design and fabrication

In order to make the coils independent and easily removable, we have wrapped them around channels that have been machined by the ICFO mechanical workshop over three cylindrical acrylic tubes (Manufacturer: Plasting (IT)) with different geometries that we describe afterwards in this section. Two out of the three acrylic tubes, after being machined, are shown in Figs. (3.11a) and (3.11b).

Let's describe first the geometry of the coils for the three DC magnetic fields $\Big\{B_z, B_x, B_y\Big\}$. We can generate the longitudinal field B_z through a solenoid and the transverse fields B_x, B_y by means of two pairs of saddle shaped coils [100]. These geometries are shown in Figs. (3.12a) and (3.12c), respectively. Just one pair of saddle coils is shown in Fig. (3.12c) for the generation of the B_x field.

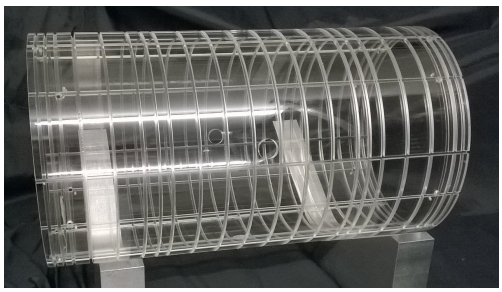

(a) Solenoid coil geometry

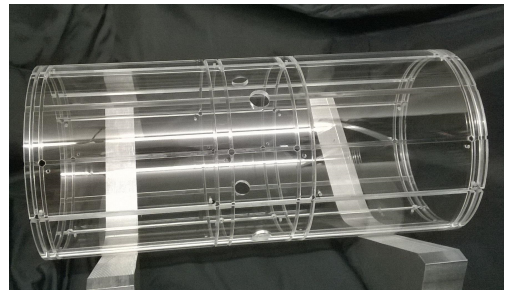

(b) Saddle coils geometry

Figure 3.11: Acrylic tubes machined with channels of the desired geometry before coils wrapping.

Another copy of saddle coils with the same dimensions, just rotated by $\pi/2$ degrees around the z axis, generates the B_y field. Both saddle coils for the generation of B_x, B_y fields are wrapped across the same acrylic tube, shown in Fig. (3.11b). At the origin (the geometric center of the coil), the magnetic field generated by a saddle coil is [100]:

$$\vec{B}_x(0,0,0) = \frac{4\mu_o NI}{\pi}\frac{h}{D^2}(s^{-1/2} + s^{-3/2})\sin(\phi/2)\vec{x} \tag{3.8}$$

where $\vec{x}$ is a unit vector in the x direction, $\mu_o = 4\pi \times 10^{-7}$ is the free space magnetic permeability, N is the number of turns in both coils, I is the current in the wire, and:

$$s = 1 + (\frac{h}{D})^2 \tag{3.9}$$

We designed two identical pairs of saddle coils with height $h = 34$cm, diameter $D = 19.86$cm and angle $\phi = 12.82°$. These values provide an expected magnetic field at the center of the coils of $B_x(0,0,0) = 7.514\mu$T for one coil turn $N = 1$ and per unit of current $I = 1A$. The same theoretical value applies to the $B_y(0,0,0)$ field, being the coil geometry the same.

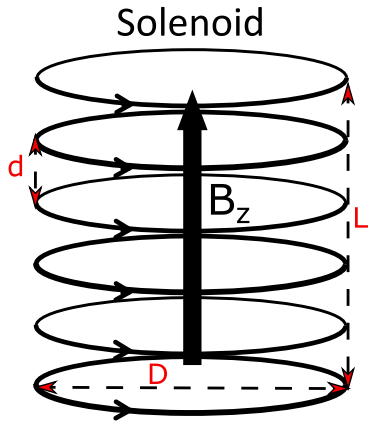

(a) Solenoid geometry

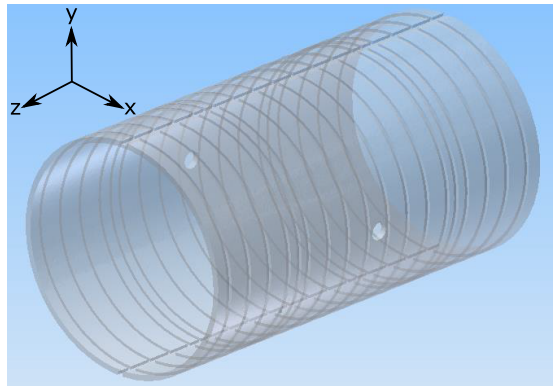

(b) Design picture of the tube machined for the Solenoid coil

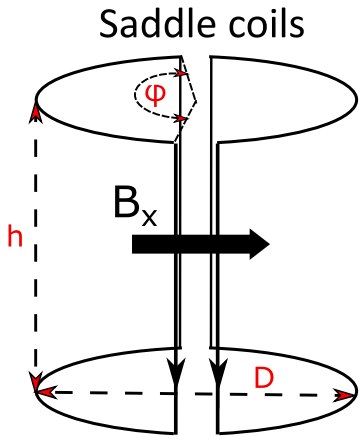

(c) Saddle coil geometry

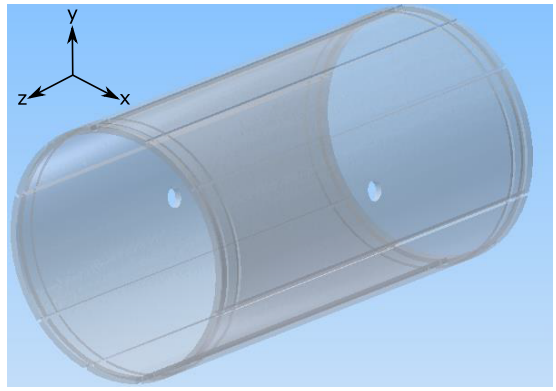

(d) Design picture of the tube machined for the Saddle coils

Figure 3.12: Geometries for the generation of DC B-fields. The black arrows on the coils indicate the versus of the current's flow. (a) The solenoid generates the B_z field. (b) Design of the acrylic tube that supports the solenoid and an anti-Helmholtz coils pair (see text) (c) A saddle coil pair generates the B_x field. (d) Design of the acrylic tube that supports two pairs of saddle coils, rotated by $\pi/2$ degrees around the z axis, for the generation of the transverse B_x, B_y fields.

On the other hand, the magnetic field generated by a circular coil along the z-axis is:

$$\vec{B}_z(0,0,z) = \frac{\mu_o}{4\pi}\frac{2\pi R^2 NI}{(z^2+R^2)^{3/2}}\vec{i} \tag{3.10}$$

where $\vec{i}$ is a unit vector in the z direction, N is the number of turns of the coil and $R = D/2$ is the coil radius. We designed a solenoid with $N_{coils} = 16$, spacing between adjacent coils $d = 2$cm, diameter $D = 19.86$cm and length $L = 30$cm. Then, by adding the contributions of Eq. (3.10) given by the $N_{coils} = 16$ at different on-axis distances, we calculated a magnetic field generated from the solenoid, at the center of the coordinate system, of $B_z(0,0,0) = 54.94\mu$T, per turn and per unit of current $I = 1A$.

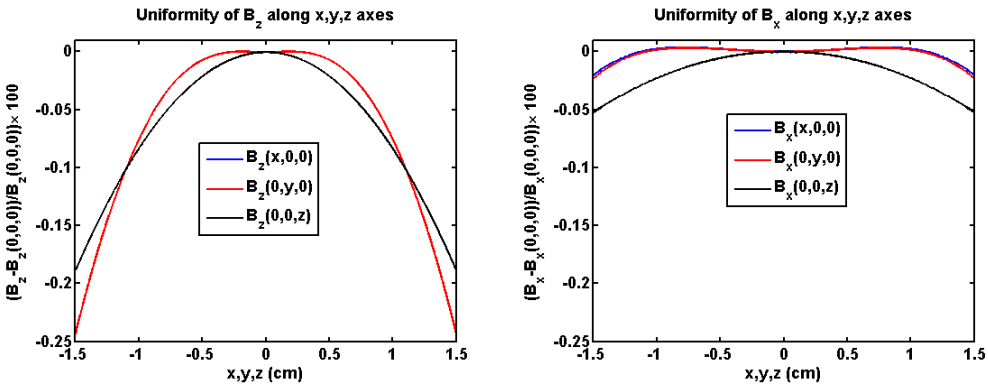

(a) Solenoid uniformity (b) Saddle coils uniformity

Figure 3.13: Spatial variation of the magnetic field generated by the solenoid and the saddle coils

We can also estimate the theoretical uniformity of the generated fields with respect to the three spatial directions. In Figs. (3.13a) and (3.13b) we show the spatial variation of the magnetic field generated by the solenoid and the saddle coils, respectively. The change is relative to the field generated at the center of the the coordinate system $\Big\{B_z(0,0,0), B_x(0,0,0)\Big\}$, while the position changes over a distance of 3cm. Within the vapor cell volume, we calculated a uniformity up to 0.25% for the solenoid field B_z and up to 0.05% for the saddle coils fields $\Big\{B_x, B_y\Big\}$.

Let's now describe the geometry of the coils for the generation of the three magnetic field gradients $\left\{\frac{\partial B_x}{\partial z}, \frac{\partial B_y}{\partial z}, \frac{\partial B_z}{\partial z}\right\}$. We can generate the longitudinal field gradient $\frac{\partial B_x}{\partial z}$ through a pair of anti-Helmholtz coils, in which the electrical current flows in opposite direction, as shown in Fig. (3.14a). The generated field is null at the center of the coils system and depends linearly on the z-position. Furthermore, we generate the transvere field gradient $\frac{\partial B_x}{\partial z}$ with respect to the beam propagation direction z by means of two pairs of saddle coils that carry electrical current in opposite direction as shown in Fig. (3.14b). The generated field is null at the center of the saddle coils system while it increases/decreases linearly for positive/negative x-position. As for the DC y-field, the $\frac{\partial B_y}{\partial z}$ gradient is generated with a second set of saddle coils, identical to those shown in Fig. (3.14b), rotated by $\pi/2$ degrees around the z axis.

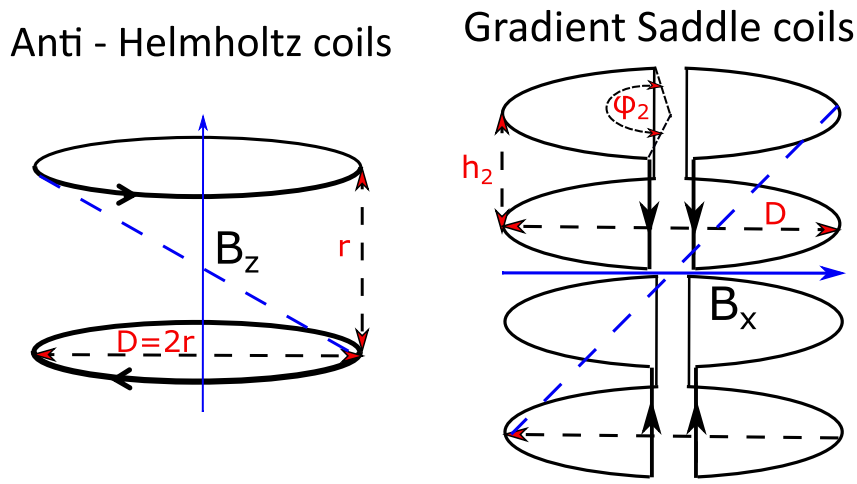

(a) Anti-Helmholtz coils geometry (b) Gradient Saddle coils geometry

Figure 3.14: Geometries for the generation of the magnetic field gradients. The black arrows on the coils indicate the versus of the current's flow (see text for details).

All the coils are made of enamelled copper wire with outer diameter of 0.63mm and resistance of 0.07Ohm/m (Model Number: ECW0.56 in Farnell

Spain) and they are fixed to the tube channels through a 2-part epoxy (Double Bubble, Manufacturer: Loctite). The solenoid and the anti-Helmoltz coils are wrapped around the largest acrylic tube (Dimensions: Outer Diameter of 200mm, Inner Diameter of 190mm, Length of 355 mm), the two pairs of saddle coils that generate the transverse DC fields $\left\{B_x, B_y\right\}$ are wrapped around the middle acrylic tube (Dimensions: OD=185mm, ID=175mm, L=355 mm), while the saddle coils pairs that generate the gradients $\left\{\frac{\partial B_x}{\partial z}, \frac{\partial B_y}{\partial z}\right\}$ are wrapped around the smallest acrylic tube (Dimensions: OD=164mm, ID=154mm, L=355 mm). Then, the three tubes are inserted concentrically inside the four mu-metal layers magnetic shielding as shown in Fig. (3.15a). The rounded Teflon slab that encloses oven and vapor cell, as previously described, is then interlocked at the center of the innermost acrylic tube as depicted in Fig. (3.15b), so that the vapor cell stands at the center of the coordinate system.

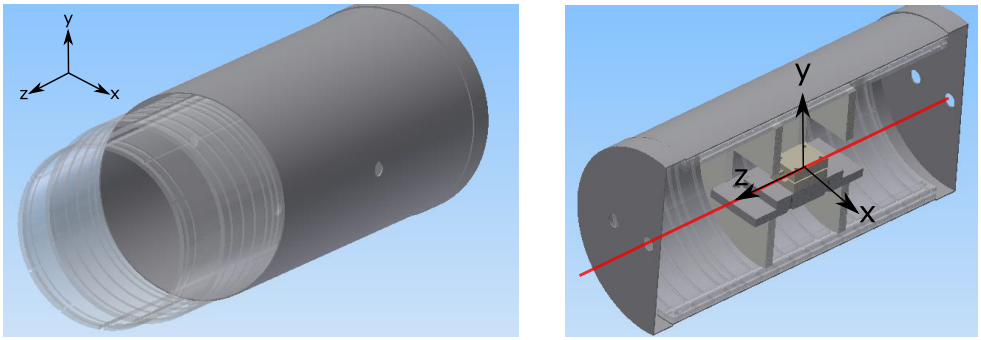

(a) Acrylic tubes and Shielding layout (b) Oven and acrylic tubes layout

Figure 3.15: Geometry of the apparatus that includes the vapor cell inside the oven, surrounded and supported by the Teflon box, and placed within the three machined acrylic tubes that hold the magnetic coils and are fixed inside the four mu-metal layers magnetic chielding.

Coils calibration

We calibrated the constructed magnetic coils by using a 3-axis fluxgate magnetometer (Model: Mag-03 MCUP range 100 from Bartington Instruments) to measure the different DC field components $\left\{B_x, B_y, B_z\right\}$ versus z-position and current. In absence of the vapor cell, the fluxgate was mounted on a post that can go through the central hole of the shielding endcaps. The post holder was fixed on a double translation stage along the z-axis, the probe beam propagation direction, so that the fluxgate sensor could be translated from the center of the coordinate system of a distance ±3cm, covering the vapor cell length. These measurements have been performed with the acrylic tubes that support the coils fixed concentrically inside the overall magnetic shielding with all the mu-metal endcaps in place. We report the effective field components, obtained by subtracting the background field from the total field, measured when electrical current is applied to different coils.

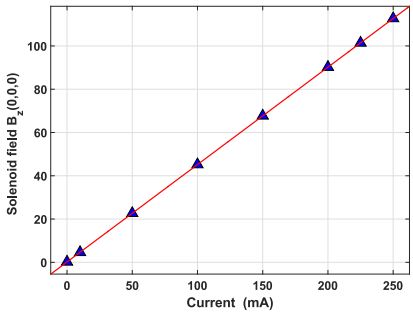

(a) $B_z(0,0,0)$ field generated by the solenoid versus electrical current. Blue triangles show data points, the red line a linear fit.

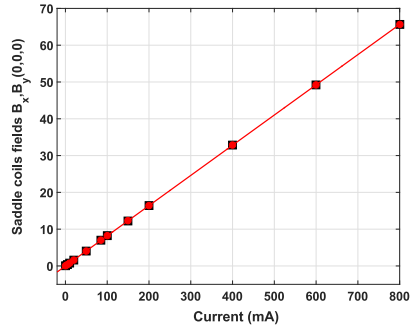

(b) $B_x(0,0,0)$ (red circles) and $B_y(0,0,0)$ (black squares) generated by the DC saddle coils versus electrical current. The red line is a linear fit.

Figure 3.16: Magnetic field components versus current intensity.

In Figs. (3.16a) and (3.16b) we report the magnetic field components $\left\{B_z, B_x, B_y\right\}$,

generated by the DC coils, versus electrical current. As expected from Eqs. (3.8) and (3.10), the magnetic field strength increases linearly with the intensity of current through the coils. For the B_z field, generated by the solenoid with $N = 8$ turns, we measured a slope of 0.449μT/mA, which is in a good agreement (2.2% error) with the theoretical value of 0.439μT/mA, obtained from Eq. (3.10) for $N_{coils} = 16$ and $N = 8$ turns. For the B_x, B_y fields, independently generated by two pairs of saddle coils with $N = 11$ turns, we measured a slope of 0.082μT/mA, that also agrees (0.7% error) with its theoretical value, given by Eq. (3.8) with $N = 11$.

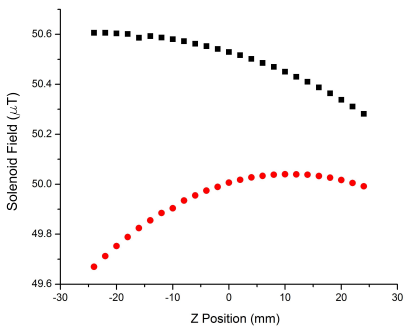

(a) $B_z(0, 0, z)$ solenoid field versus z-position at current I=100mA. *Black points*: all end-caps attached to the tubular shielding. *Red points*: shielding end-caps removed from one side.

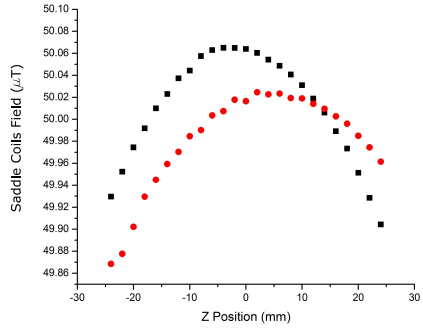

(b) $B_x(0, 0, z)$ (red circles) and $B_y(0, 0, z)$ (black squares) saddle coils fields versus z-position at constant current I=600mA.

Figure 3.17: Magnetic field components versus z-position.

In Fig. (3.17) we report the measured DC field components versus the z-position. For the longitudinal field B_z, generated by the solenoid, we applied a current of $100mA$ and we measured the field strength at different position $\pm$3cm of the fluxgate sensor along the z-axis, as shown in Fig. (3.17a). Over the spatial region of interest, $\pm$1.5cm equal to the 3 cm length of the vapor cell, we measured a B_z field inhomogeneity of about 10 nT/mm. We also show that by removing

the endcaps from one side of the tubular shielding both the strength and the homogeneity of the generated field change, because of the unshielded environment magnetic field. For the B_x, B_y fields, we applied a current of 600mA and we measured the field components over the same length along the z-axis. For both fields generated by the saddle coils, we measured an inhomogeneity of about 2 nT/mm along $\pm$1.5cm from the center of the coordinate system $\frac{\partial B_x}{\partial z}$.

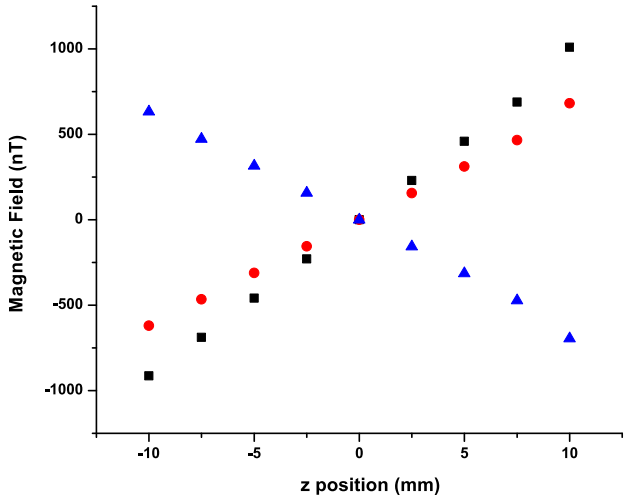

Figure 3.18: **Magnetic field gradients.** Magnetic fields B_z (black squares), B_x (red circles) and B_y (blue triangles) generated by the gradient coils versus the z-axis position. The fields are measured by a 3-axis fluxgate sensor with 10 picotesla sensitivity. The negative slope of the B_y field is due to the opposite versus of the fluxgate y-sensor with respect to the direction chosen in the experiment reference.

To complete the calibration section, in Fig. (3.18) we show the magnetic field components generated by the gradient coils versus the z-position. For the gradient of the longitudinal field B_z, generated by the anti-Helmholtz coils pair shown in Fig. (3.14a), we measured a slope of 94.13 nT/mm with applied constant current of 100mA. For the gradients of the field components $\left\{B_x, B_y\right\}$, generated by two identical pairs of saddle coils as in Fig. (3.14b), we measured a slope of

63.72 nT/mm and 64.8 nT/mm, respectively. By varying the intensity of current through the coils we have a control on the slopes of the field gradients in the three directions. While this complete coil calibration and characterization is necessary for future work with the described apparatus, for the spin noise spectroscopy experiment, described in the Chapter 4, we just applied the transverse DC field B_x and we compensate the gradient of the same field component along the laser beam propagation direction.

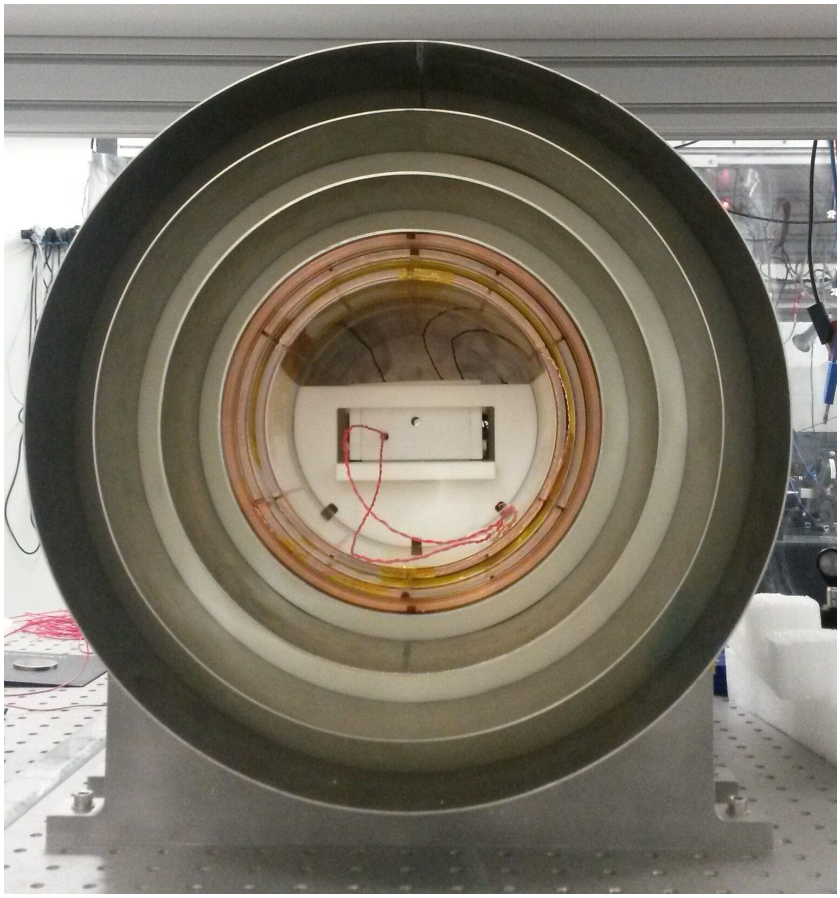

Figure 3.19: **Overall Atomic Setup** Transverse view of the atomic and magnetic system formed by the vapor cell, the oven, the Teflon isolation box, the magnetic coils and the magnetic shielding.

We conclude this section by showing in Fig. (3.19) the transverse view of

the complete apparatus that includes the vapor cell inside the oven, the Teflon isolation box and support, the three acrylic tubes that hold the magnetic coils and the 4-layers magnetic shielding. In the next section we describe how the atomic system is probed either with coherent or squeezed light.

3.3 Generation and detection of polarization squeezing

As explained in chapter (2), a polarization interferometer allows one to obtain information on the atomic sample by detecting the polarization rotation of a linearly polarized probe beam. Such a rotation angle depends on the magneto-optical properties of the atomic ensemble. Then the degree of freedom that carries all the measurement information is the light polarization and the measured observables are the Stokes polarization operators. Polarization squeezing is then necessary in order to reduce the polarization quantum noise. In Fig. (3.20) we show the full experimental apparatus that combines a source of polarization squeezing with the setup for atomic spectroscopy in a low-noise magnetic environment, previously described. While the full experiment and data analysis are described in Chapter 5, in this section we present details on the generation, detection and stabilization of polarization squeezed light.

3.3.1 The squeezer

The source of squeezing is based on an optical parametric oscillator (OPO) that has been designed and built by A. Predojević and it is presented in details in

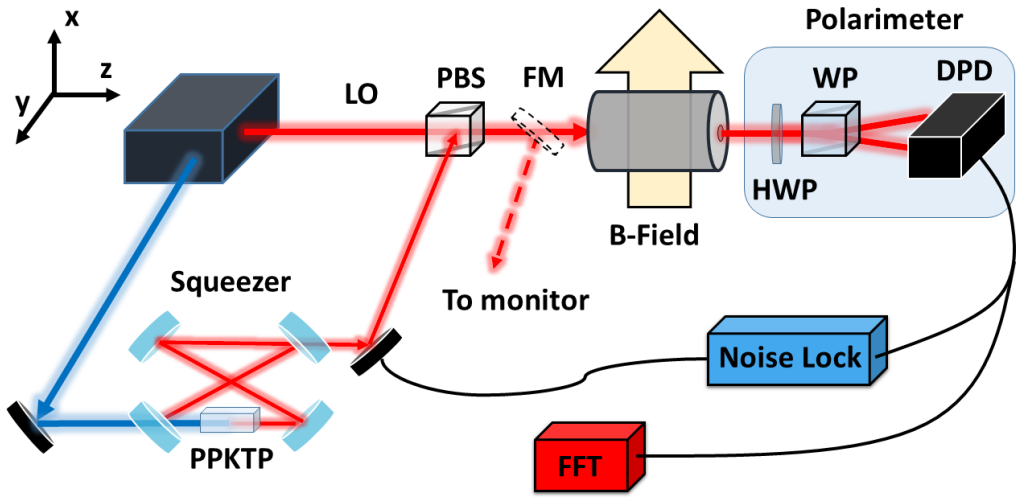

Figure 3.20: **Experimental setup for Squeezed-light atomic spectroscopy** The overall setup includes the laser source, the squeezer, a monitor for the detection of squeezing before the atomic interaction and a second polarimeter for the detection of the signal after the atomic interaction. The detector differential output is fed into both the FFT spectrum analyzer and the quantum noise lock circuit for the squeezing phase stabilization, as described in the text. **Experimental schematic** LO - local oscillator, PBS - polarizing beam splitter, DPD - differential photo detector, FM - flip mirror, HWP - half wave-plate, WP - Wollaston prism, FFT - fast Fourier transform analyzer.

[69, 101]. The nonlinear process that occurs within the OPO is a conventional spontaneous parametric down-conversion (SPDC) in a type-I phase matched PPKTP crystal. The full-optical setup for squeezing generation, in absence of atomic interaction, is shown in Fig. (3.21). Our laser source (TA-SHG Toptica) is an external-cavity diode laser at 794.7nm, tunable over the D_1 line or ^{85}Rb. A first laser output is spatially filtered through a polarization maintaining fiber and it is fed into the double fiber interferometer system for the laser frequency stabilization, that we describe in section (3.4). A second laser output, from the same source, passes through a tapered amplifier and it is split into two parts: the weaker is spatially filtered with a single mode fiber and works as local oscillator (LO).

The stronger is frequency doubled to 397.4nm, is spatially filtered by means of a

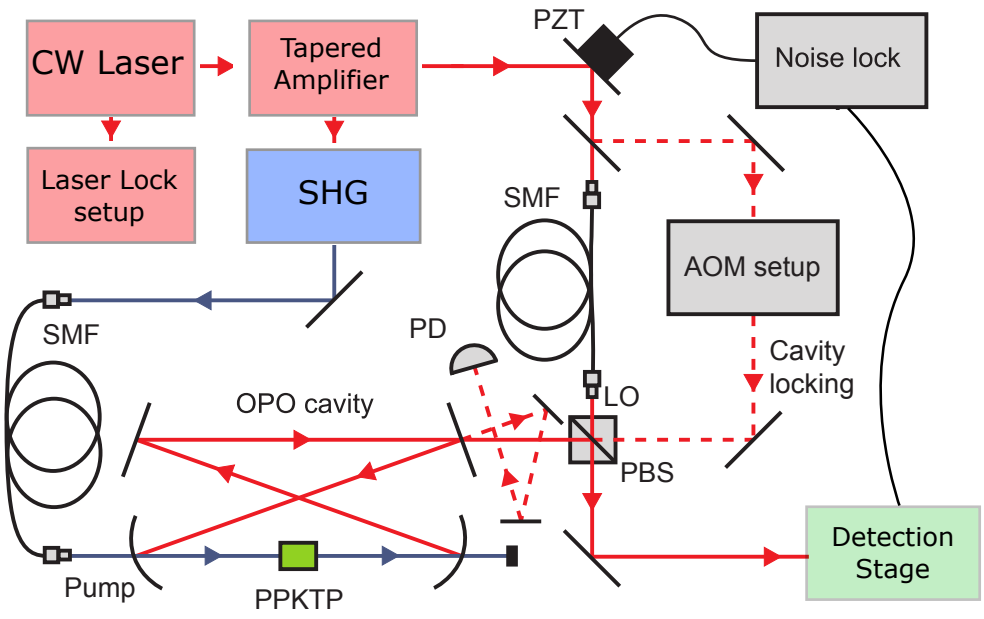

Figure 3.21: **Squeezed light generation**. SHG - second harmonic generation, OPO- optical parametric oscillator, PPKTP - phase matched nonlinear crystal, LO - local oscillator beam, PZT - Piezo transducer, PBS - polarizing beam splitter, AOM - acousto optical modulator, HWP - half-wave plate, SMF - single mode fiber, PD - photodiode.

single mode fiber, then it works as pump of the OPO in which squeezed vacuum is generated through SPDC in the V polarization at the same LO frequency. By mixing the generated squeezed vacuum state with the horizontally-polarized LO coherent state by means of a polarizing beam splitter (PBS), as shown in Fig. (3.21), we obtain polarization squeezing from amplitude squeezing. By scanning the phase relation between the two beams, trough a piezo-electric actuator on the LO path, we generate squeezing fluctuations in the diagonal or circular polarization basis that correspond to the Stokes parameters S_2 and S_3 (See Chapter 1). The double detection stage (before and after the atomic interaction) and the quantum noise lock are described in next section. A photo of the OPO cavity

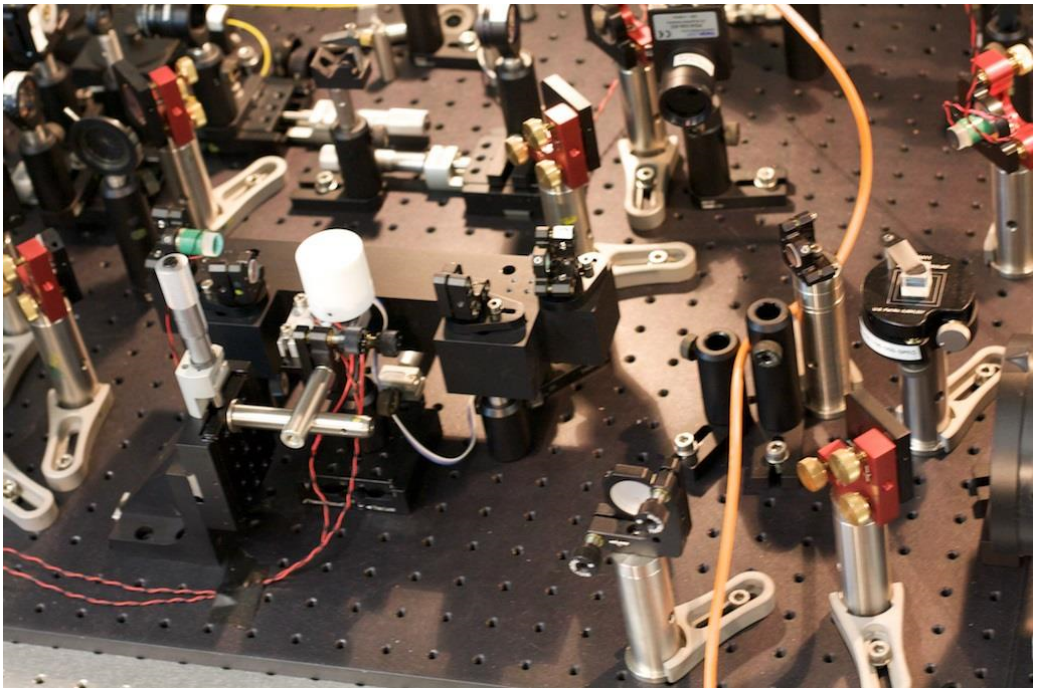

Figure 3.22: **The Squeezer (OPO)**. A photo of the OPO cavity that we used for generate squeezed vacuum. The vacuum is then combined on a PBS (to the right of the picture) with a bright local oscillator (LO) in order to generate polarization squeezing.

is shown in Fig. (3.22). To stabilize the length of the OPO we use a modified Pound-Drever-Hall (PDH) technique [102]. The laser is current-modulated, and thus frequency-modulated, at 20 MHz, as required by the PDH technique. A part of the laser source at 795 nm is used as locking beam and passes through a double-pass acousto-optic modulator (AOM) that adds an adjustable offset (630MHz) to its frequency, to make it resonant to a higher order transverse mode of the cavity with H polarization, orthogonal to the OPO output. As shown in Fig. (3.21), this beam enters the OPO cavity from a mode counter-propagating to the squeezed vacuum. This allows us to stabilize the cavity with no contamination of the squeezed vacuum by the locking beam, which is simultaneously at a different frequency, polarization, spatial mode, and direction of propagation. The nonlinear

crystal is birefringent, which implies that the cavity resonates at different frequencies for orthogonal polarization modes. We adjust the locking-beam frequency to make the cavity resonate simultaneously for both the squeezed vacuum and the locking-beam modes. We use then the error signal given by the locking beam to stabilize the cavity length, to keep the cavity resonant to the squeezed vacuum mode. More details about the cavity locking are given in [40, 103].

3.3.2 Detection and quantum noise lock

The squeezing is detected by a conventional balanced detection setup that consists of an half-waveplate at 22.5°, a second optical element that splits the horizontal and vertical polarization components and two photodiodes that collect the two beams. We use commercial balanced detector (PDB450A-DC Thorlabs) in which the signals from the two photodiodes are electronically subtracted and the differential signal amplified to give a single output that we monitor simultaneously on both a scope and a spectrum analyzer. In our experiment we use two different balanced detectors. The first, whose scheme and photo are shown in Figs. (3.23a) and (3.23b) respectively, is used as a monitor of the squeezing *before* the atomic interaction (see Fig. 3.20). In this detector the polarization components are separated by a polarizing beam splitter (PBS), then the two beams are focused into the photodiodes and two AR-coated (HR$[710-850\text{nm}]> 99.9\%$) plano mirrors (Number: 108198 from Layertec) send back the photons reflected from the photodiodes windows, in order to increase the quantum efficiency up to 88%, as reported in [101], in which the same detection scheme was already implemented. We send the probe light to this monitor detector by means of a flip mirror as shown in Fig. (3.20). A second polarimeter setup, whose scheme and photo are

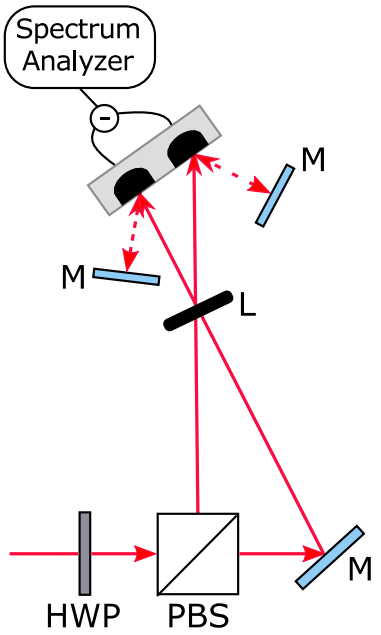

(a) **Monitor polarimeter scheme,** L - Lens, M - AR-coated plano mirror, HWP - Half wave plate, PBS - Polarizing beam splitter

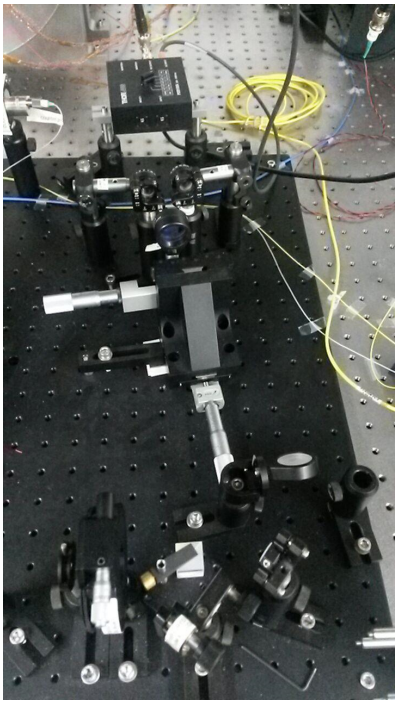

(b) **Photo of the monitor polarimeter.** Note that the lens L is mounted on a micrometer translation stage.

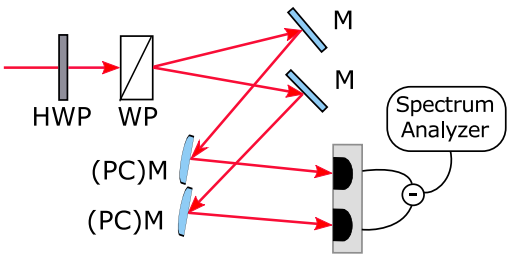

(c) **Detection polarimeter scheme.** HWP - Half wave plate, WP - Wollastone prism, M - Plano AR-coated mirror, (PC)M - Plano-concave AR-coated mirror

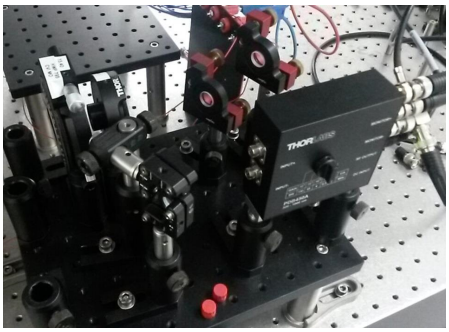

(d) **Photo of the detection polarimeter.** The PDB detector is in a vertical configuration.

Figure 3.23: **Double polarimeter detection stage**. We show schematic and photos of the two polarimeter stages before (monitor) and after (signal detection) the atomic interaction.

shown in Figs. (3.23c) and (3.23d) respectively, is used to detect the probe light *after* the atomic interaction, as schematically shown in Fig. (3.20). In this second setup the optical element that splits the two polarization is a Wollaston prism and we removed the glass windows from the photodiodes in order to minimize the reflection and increase the quantum efficieny to 92%. Furthermore, the orthogonally polarized beams are focused by two AR-coated (HR[710 − 8805nm]> 99.9%) plano-concave mirrors (Number: 102548 from Layertec) to the photodiode surfaces at an angle of about 3°, in order to avoid back reflection into the setup and the OPO cavity when the squeezed light is used as probe. Both balanced detectors have a switchable bandwidth and transimpedance gain. In our experiment we used a gain of $G = 10^6$V/A corresponding to a 300kHz bandwidth. Indeed, as decribed in Chapter 4, the spin noise spectroscopy experiment is performed for magnetic fields that correspond to a Larmor precession frequency smaller than 100kHz. The differential output signal is fed into a spectrum analyzer that record the polarization noise trace in time with zero span mode. In fig. (3.24) we show the recorded squeezing noise oscillations obtained by scanning the phase of the coherent LO with a piezo-electric actuator and acquired at room temperature with the first monitor balanced detector, before the atomic interaction. We generate a maximum squeezing of 3.2dB measured at a central frequency of 100kHz with resolution and video bandwidth of 10kHz and 10Hz respectively. At room temperature, after the atomic interaction, we measured the same amount of quantum noise suppression with the second balanced detection setup. However, by increasing the atomic density of the Rb atomic ensemble, the amount of absorption of the off-resonance probe beam increases up to a maximum of 30% at the largest investigated atomic density ($n = 1.3 \times 10^{13}$ atoms/cm^3). Then, the amount of squeezing is partially reduced by absorption from the atomic ensemble and this is

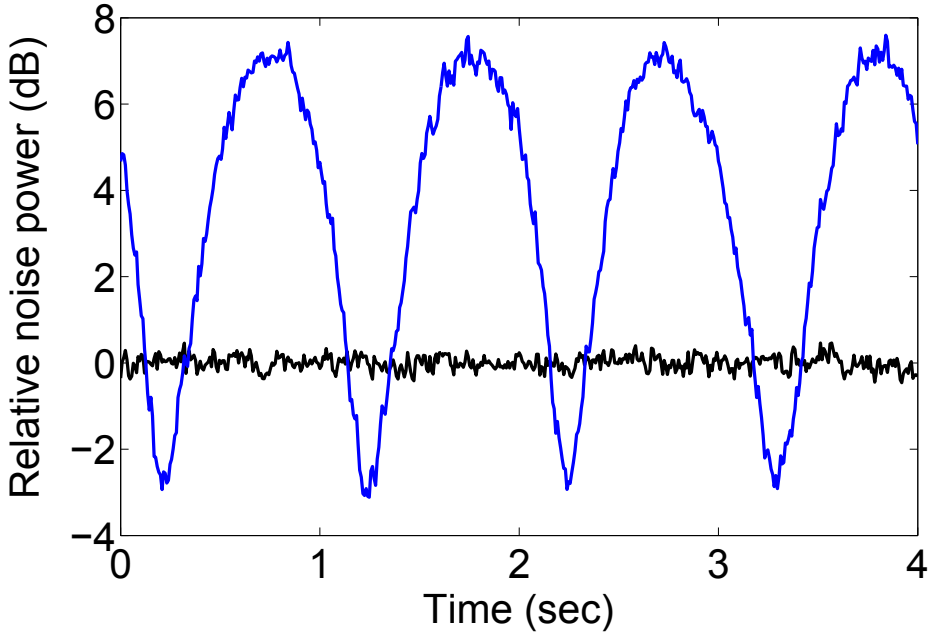

Figure 3.24: **Room-temperature squeezing oscillations**. Polarization noise power measured by the monitor detector. Center frequency 100 kHz, zero-span mode, RBW=10kHz, VBW=10Hz. The black horizontal trace shows the photon shot noise level for a coherent probe with the OPO off and it is taken as a reference at 0dB. The blue trace represents the quantum oscillations below (squeezing) and above (anti-squeezing) the shot-noise level, acquired with the OPO on as the LO phase is scanned.

actually the only detrimental effect in the high-density scenario, as we describe in details in Chapter 4. At the largest investigated density the amount of squeezing, after the atomic interaction, is about 2dB out of the 3.2dB of injected squeezed light.

In Fig. (3.25) we show the squeezing oscillations measured by the second polarimeter after the atomic interaction at a density $n = 2.4 \times 10^{12}$ cm^{-3}, for which 3dB of shot noise suppression is obtained, out of the 3.2dB squeezed light probe. Being the squeezing a phase-dependent process, the maximum polarization squeezing is kept stable by a quantum noise lock that stabilizes the piezo-translator on the LO optical path. While the piezo is scanning at a very low frequency of

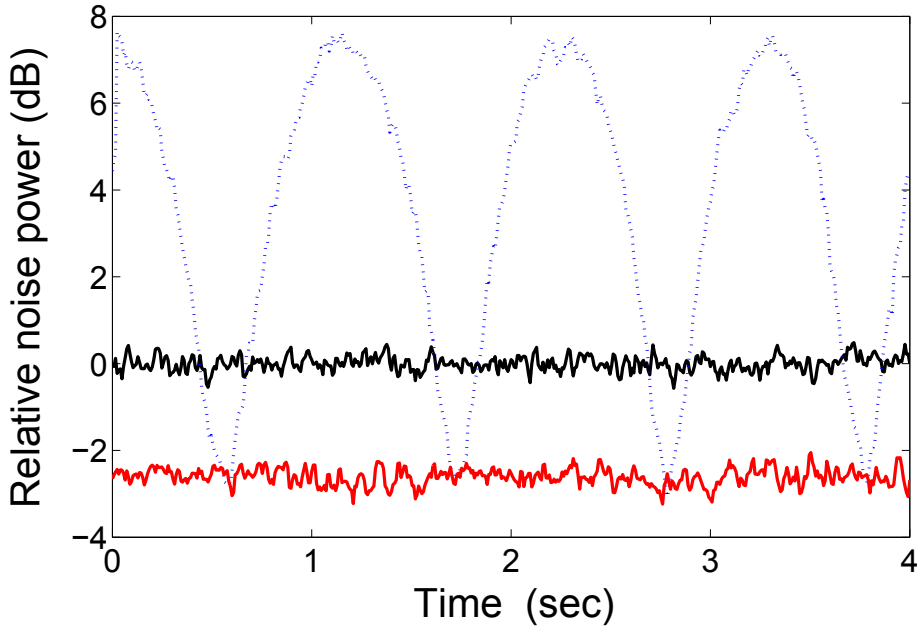

Figure 3.25: **Stabilized squeezing after the atomic interaction**. Polarization noise power measured after atomic interaction at density $n = 2.4\times10^{12}$ cm^{-3}. Center frequency 100 kHz, zero-span mode, RBW=10kHz, VBW=10Hz. The black trace shows the photon shot noise level for a coherent probe, the blue trace represents squezing oscillations as the LO phase is scanned, the red trace is the sub-shot noise level of −3dB after the phase lock to the maximum squeezing.

about 1.3 Hz we can reproduce the noise oscillations, as the spectrum analyzer does, by plugging the balanced detector output to a multiplier circuit that squares the differential signal and, after frequency filtering and amplification described in [104], gives the squeezing oscillations from which we obtain en error signal. While in [104] a side-of-fringe locking was sufficient to maintain a constant phase regardless of its value, in this experiment we need the right phase that gives the minimum in the polarization noise oscillations. In order to do that we add a faster modulation of 709 Hz from a lock-in-amplifier (LIA) to the pump piezo-translator and we demodulated the oscillating signal at the same LIA reference frequency with a phase of 94.89° by obtaining a dispersive error signal with the zero voltage

corresponding to the minimum of the squeezing oscillation. This error signal is then fed to a FPGA-based PID controller that applies a feedback on the LO piezo to maintain the phase stable to the minimum of the squeezing oscillations, as shown in Fig. (3.25).

3.3.3 Optimization of the source and detection losses

An important difference of the experiment described in this Thesis with respect to prior experiments of our group [69, 40] is the wavelength of the generated polarization squeezed light. In fact, the spin noise spectroscopy (SNS) technique is based on getting information about the physical properties of an atomic vapor or a solid state system by keeping it *unperturbed*. This means that, in a typical Faraday-rotation based measurement, the probe beam must be off-resonance in order to minimize absorption from the sample and not to perturb nor even optically pump the atomic ensemble out from the equilibrium thermal state. After modifying the laser frequency from resonance to the off-resonance condition, we had to recover the crystal phase-matching condition for the new wavelength by varying the crystal temperature. We did this by optimizing the gain of the optical parametric amplification (OPA) of a seed beam at the laser frequency, resonant with the OPO, in presence of the pump beam at double the frequency. The parametric gain is defined in [101] as $G = (1-\mu^2)^{-2}$ with $\mu = \sqrt{P/P_{th}}$, where P is the optical pump power and P_{th} is the OPO threshold power. For completeness, for a given gain, the theoretical maximum squeezing spectrum is given by:

$$S(\Omega) = 1 - \frac{4\eta|\mu|Q}{(1+|\mu|)^2 + \Omega^2} \tag{3.11}$$

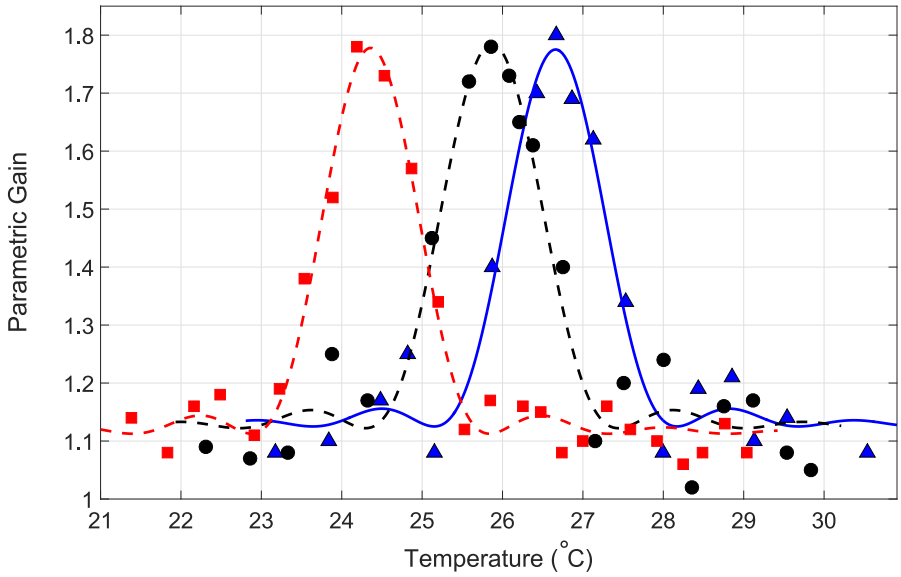

Figure 3.26: **Parametric gain versus crystal temperature**. We show the SPDC parametric gain versus the PPKTP crystal temperature for laser wavelengths of 377072.3 GHz (red squares), 377106.6 GHz (black circles) and 377127.3 GHz (blue triangles). The data are fitted with a function proportional to the $sinc(\Delta k L_c/2)$, where Δk is the SPDC phase mismatch and $L_c = 1$cm is the crystal length [103].

where $\eta = 0.9$ iis the cavity escape efficieny, Q is the detector quantum efficiency and Ω is the detection frequency. In Fig. (3.26) we show the measured parametric gain of the SPDC process in the OPO at three different laser frequencies, measured with a commercial wave-meter. The down-converted photons have half frequency of the pump beam through energy conservation of the SPDC process. As you can see from our measurement, the maximum reachable gain ($\simeq 1.8$) is not affected by the frequency change that is indeed smaller than the crystal efficiency frequency bandwidth. After this optimization we keep the crystal at a temperature of 26°C that satisfies the phase-matching condition for a wavelength of 794.718nm, corresponding to a frequency of $377127,3$ GHz that is 20GHz off-resonance with respect to the ^{85}Rb D_1 resonance central line. We keep this laser frequency in

the main experiment described in the next chapter. Under optimal conditions of phase-matching and cavity alignment, the main experimental limitation to the amount of generated squeezing is the optical pump power. We obtain the maximum amount of squeezing of 3.2dB with a pump power of $P_{pump} = 45$mW. A larger amount of laser power would increase the amount of squeezing until a limit given by the crystal damage threshold and other detrimental effects like thermal lensing [101]. Different losses contributions affect the squeezing in its generation, propagation and detection stages. The total detection efficiency is 85.6% and it includes escape efficiency (96%), the homodyne efficiency of mode macthing between squeezed vacuum and LO (98%), transmission efficiency through high-reflectivity optical elements (99%) and balanced detection quantum efficiency (92%). More details about the cavity losses and limitations are given in prior works [101, 69] and are beyond the scope of this thesis.

3.4 Laser frequency stabilization

All prior works with squeezed light carried out in our lab [69, 40, 96] used probe light close to the Rb absorption resonance. Then, in all these experiments the laser frequency was locked using a combination of saturated absorption spectroscopy (SAS) of a Rb vapor and the Pound-Drever-Hall [102] technique. As references, atomic lines are very stable but give low signal to noise ratios and a limited selection of frequencies. As already mentioned in the previous section, in our experiment we need to lock the laser frequency far from resonance, at about 20 GHz from the ^{85}Rb D_1 resonance line. To solve this problem, we have developed a long-term laser frequency stabilization system based on fiber interferometers. The system is described in details in our publication by Jia Kong et al. [105]. It uses

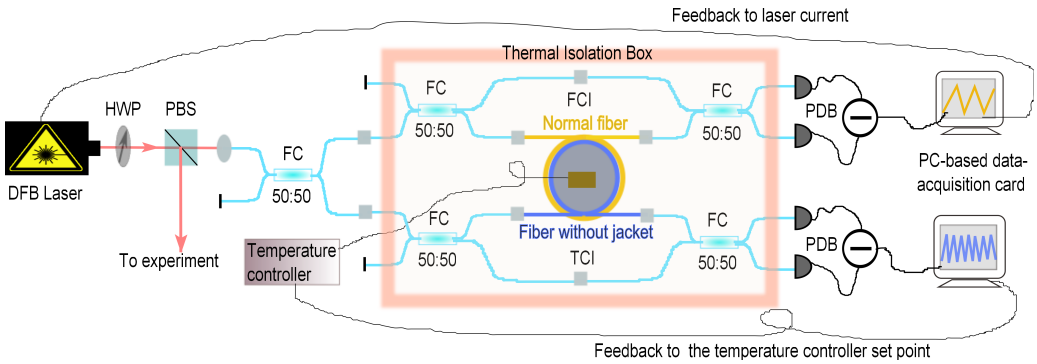

Figure 3.27: **Schematic of laser frequency locking system**. Using a half-wave plate (HWP) and a polarizing beam splitter (PBS), a few 10s of μW of power from the laser to be stabilized, at 795 nm, is injected into a fiber system containing two unequal-path Mach-Zehnder interferometers. Each interferometer is composed of two 50:50 fiber couplers (FC) and an additional 5 m fiber to imbalance the paths. In the frequency control interferometer (FCI) the extra fiber is a jacketed single mode fiber, while for the temperature control interferometer (TCI), it is a polarization maintaining fiber without jacket. The fibers are wound around a 10 cm diameter aluminum cylinder fitted with a resistive heater and a resistive temperature sensor. In each interferometer the output powers are collected on a Thorlabs balanced amplified photodetector (PDB450C), providing signals that are used for feedback, either to the laser current, or to the set-point of a temperature controller from Wavelength Electronics (model HTC1500) by a digital controller (PC-based data-acquisition card). The interferometers are enclosed in a insulation layer of extruded polystyrene foam.

only the target laser, without any other transfer lock from other references, and it is based on a pair of 5m fiber Mach-Zehnder interferometers. The "frequency control interferometer" (FCI) is used to sense and stabilize the laser frequency, while a second "temperature control interfetometer" (TCI), by using a jacketless fiber, is used to sense and eliminate fluctuations in the temperature of the thermal reservoir to which both interferometers are attached. In Fig. (3.27) we show the experimental setup for such laser frequency stabilization from ([105]), in which the laser source was a distributed-feedback (DFB) diode laser at 795 nm. In the experiment described in this Thesis we used exactly the same locking setup of Fig. (3.27) with an external-cavity diode laser at 794.7nm as laser source, as described in section (3.3.1) and depicted in Fig. (3.21).

Chapter 4

Squeezed-light spin noise spectroscopy

In this chapter we report quantum enhancement of Faraday rotation spin noise spectroscopy by polarization squeezing of the probe beam. As described in the previous chapter (3), we use natural abundance of Rb in 100 Torr of N_2 buffer gas and squeezed light from a sub-threshold optical parametric oscillator stabilized 20 GHzto the blue of the D_1 resonance. We observe that an input squeezing of 3.0 dB improves the signal-to-noise ratio by 1.5 dB to 2.6 dB over the combined (power)$\otimes$(number density) ranges (0.5 mW to 4.0 mW)$\otimes$(1.5×10^{12}cm^{-3} to 1.3×10^{13}cm^{-3}), covering the ranges used in optimized spin noise spectroscopy experiments. We also show that squeezing improves the trade-off between statistical sensitivity and systematic errors due to line broadening, a qualitative new quantum advantage with respect to previous applications of squeezed light. The described experiment has been carried out at ICFO and it has been published in

[72]. Its theoretical Appendix, reported in section (2.3.4), has been written by Ricardo Jiménez-Martínez.

4.1 Introduction

The presence of intrinsic fluctuations of a spin system in thermal equilibrium was first predicted by Bloch [23] and experimentally demonstrated in the 1980's by Aleksandrov and Zapasskii [35]. In the last decade, "spin noise spectroscopy" (SNS) has emerged as a powerful technique for determining physical properties of an *unperturbed* spin system from its noise power spectrum [24, 25]. SNS has allowed measurement of g-factors, nuclear spin, isotope abundance ratios and relaxation rates of alkali atoms [26, 27], g-factors, relaxation times and doping concentration of electrons in semiconductors [28, 106, 107, 108, 109] and localized holes in quantum dot ensembles [29, 110] including single hole spin detection [111]. Recently, SNS has been used to study complex optical transitions and broadening processes [66, 112], coherent phenomena beyond linear response [113] and cross-correlations of heterogeneous spin systems [47, 114].

Spin noise has been measured with nuclear magnetic resonance [115, 116] and magnetic force microscopy [30, 31, 117], but the most sensitive and widely used detection technique is Faraday rotation (FR) [35, 26, 27], in which the spin noise is mapped onto the polarization of an off-resonant probe. In FR-SNS, spin noise near the Larmor frequency competes with quantum noise [39] of the detected photons, i.e., the optical shot noise. The main figure of merit is η, the peak power spectral density (PSD) due to spin noise over the PSD due to shot noise, called "signal strength" [118] or the "signal-to-noise ratio" (SNR). Reported SNR for

single-pass atomic ensembles ranges from 0 dB to 13 dB [26, 46], and up to 21 dB in atomic multi-pass cells [90]. Due to weaker coupling to the probe beam, reported SNR ranges from -50 dB to -20 dB in semiconductor systems (See Table 1 in [118]). Several works have studied how to improve the polarimetric sensitivity [119] or to cancel technical noise sources [28, 106, 108], but without altering the fundamental tradeoff between sensitivity and broadening processes [119].

For small optical power P and atomic density n, SNR is linear in each: $\eta \propto nP$. At higher values, light scattering and atomic collisions broaden the spin noise resonances, and thus introduce systematic errors in measurements, e.g. of relaxation rates, that are derived from the SNS linewidth [26, 27, 28]. This trade-off between statistical sensitivity and line broadening is a fundamental limitation of the technique, with its origin in quantum noise properties of the atomic and optical parts of the system.

Here we work in a high-density regime, with atomic number densities up to $n \sim 10^{13}\text{cm}^{-3}$, covering the range of recent experiments with optimized atomic instruments [26, 27, 46, 47]. Earlier studies in this regime have observed non-trivial interactions between optical quantum noise and nonlinear magneto-optical rotation (NMOR) of a on-resonance probe [45] including increased measurement noise as a result of input squeezing for densities above $n \approx 2 \times 10^{11}\text{cm}^{-3}$ [43]. It is thus not obvious that squeezing will improve a high-density Faraday rotation measurement [24, 7], as it does for lower densities [39, 40]. In contrast, here we observe that squeezing does in fact improve both the signal to noise ratio and the sensitivity/line broadening trade-off in SNS, over the full practical range of the technique. It is worth noting that we work with an un-polarized atomic ensemble

and off-resonant probing, as required for the non-perturbative SNS technique. This may explain the difference between our results and prior experiments [43, 45].

4.2 Mode of operation

We optically probe the atomic ensemble via Faraday rotation (FR) and obtain a signal proportional to the on-axis projection of the collective spin of the Rb group of atoms in thermal equilibrium. The collective spin precesses in response to an external transverse magnetic field and experiences a stochastic motion as required by the fluctuation-dissipation theorem [14, 118]. For rubidium, which has two isotopes ^{85}Rb and ^{87}Rb, and shot-noise limited detection [84], the power spectrum of the FR signal is given by a double Lorentzian function:

$$S(\nu) = S_{\rm ph} + \sum_{i\in\{85,87\}} S_{\rm at}^{(i)} \frac{(\Delta\nu_i/2)^2}{(\nu-\nu_L^{(i)})^2 + (\Delta\nu_i/2)^2}, \tag{4.1}$$

where $S_{\rm ph} \propto P\xi^2$ is the (frequency-independent) shot-noise contribution at power P and ξ^2 is the squeezing factor. The sum on i is over atomic mass, $\nu_L^{(i)}$ and $\Delta\nu_i$ are the (linear) Larmor frequency and FWHM width, respectively. $S_{\rm at}^{(i)}$ is the height of Lorentzian spin noise contribution of the i-th species. Exact expressions of these quantities have been already defined in section (2.3.4) and are reported again in the next section (4.3). We probe the atomic ensemble with coherent and polarization squeezed respectively. By fitting the measured spin noise spectra with equation (4.1), we estimate signal-to-noise ratio $\eta_i \equiv S_{\rm at}^{(i)}/S_{\rm ph}$ and resonance linewidth $\Delta\nu_i$ and we compute the quantum advantages due to the polarization squeezing of the probe. In section (4.5) we fully described the data analysis and the experimental results.

4.3 Theory

In what follows we remind expressions for the shot-noise background, $S_{\rm ph}$, and the height of the Lorentzian spin noise, $S_{\rm at}^{(i)}$, appearing in the function used to fit the power spectral density (PSD) of the polarimeter output as described in Section 4.5. These have been already derived in section (2.3.4). Using these expressions we obtain the signal-to-noise ratio (SNR) $\eta_i = S_{\rm at}^{(i)}/S_{\rm ph}$ which is used to estimate η for ^{85}Rb as a function of probe light power and density. In generating these estimates we use the parameters quoted in Table 4.1.

4.3.1 Detector signal

In our experiment we analyze $S(\nu)$, the power spectral density (PSD) of $V_{\rm DPD}$, the output voltage of the polarimeter detector described in Chapter (3), expressed in V^2/Hz. Because the scalar signal is acquired by combining polarization rotation information over $\mathcal{A}$, the area of the beam, we write the signal as

$$V_{\rm DPD}(t) = 2G\Re[P\Theta_{\rm FR}(t) + P_{\rm SN}(t)], \tag{4.2}$$

where $G = 10^6$ V/A is the transimpedance gain, $P = \int_{\mathcal{A}} dxdy\, \mathcal{I}(x,y)$ is the total power of the beam reaching the detector with intensity $\mathcal{I}(x,y)$, and $\Theta_{\rm FR} \ll 1$ is the Faraday rotation (FR) angle as defined in Eq. (2.35) below. $\Re = Qq/E_{\rm ph}$ is the detector responsivity, where Q denotes the quantum-efficiency of the detector, $E_{\rm ph} = \hbar\omega = 2.4910^{-19}$J is the photon energy at 795 nm, and $q = 1.610^{-19}$C. $P_{\rm SN}$ is a white-noise component due to shot noise, that we compute in the next section.

4.3.2 Photon shot-noise

The contribution from photon shot-noise to $S(\nu)$ is given by

$$S_{\mathrm{ph}} = 2G^2 q(\Re P)\xi^2, \tag{4.3}$$

where ξ^2 represents the light-squeezing parameter.

Figure 4.1 shows S_{ph}, as estimated by fitting the measured spin noise spectrum, at different atomic densities for a coherent probe (hollow symbols) and squeezed probe (filled symbols). The dashed lines and solid lines in Fig. 4.1 correspond to a fit of the data using Eq. (4.3), with Q and ξ^2 as the free parameter in the fit for coherent-probe and squeezed-probe data, respectively. From the coherent-probe data, for which $\xi^2 = 1$, we obtain $Q = 0.87$. The different slopes observed for the squeezing-probe data can be explained by the degradation of squeezing due to light absorption, given by [39]

$$\xi^2 = 1 - (1 - \xi_0^2)\exp[-\mathrm{OD}], \tag{4.4}$$

where OD is the optical depth experienced by the light beam. For our experimental conditions $\xi_0^2 = 0.55$, obtained by fitting the measured ξ^2 to Eq. (4.4) and can be considered as the squeezing parameter of the transmitted light when the cell is at room temperature.

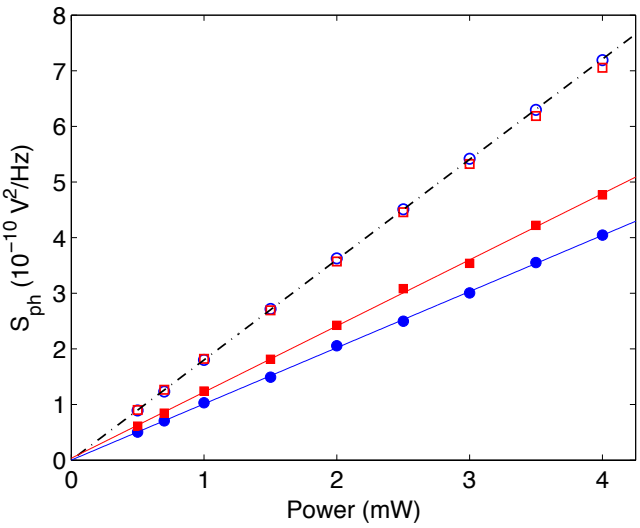

Figure 4.1: Shot-noise background, $S_{\rm ph}$, as a function of probe power reaching the detector for coherent probe (hollow symbols) and squeezed probe (filled symbols) at densities of 2.4×10^{12} cm^{-3} (blue) and 9.3×10^{12} cm^{-3} (red).

4.3.3 Atomic noise

The spin noise oscillates at the Larmor frequency ν_i and with FWHM linewidth $\Delta\nu_i$, so that

$$S(\nu) = S_{\rm ph} + \sum_{i\in\{85,87\}} S_{\rm at}^{(i)} \frac{(\Delta\nu/2)^2}{(\nu-\nu_i)^2 + (\Delta\nu/2)^2} \tag{4.5}$$

where

$$S_{\rm at}^{(i)}(\nu) = \frac{4G^2\Re^2P^2}{\pi\Delta\nu/2}\text{var }\Theta_{\rm FR}^{(i)}. \tag{4.6}$$

From the fitted amplitude $S_{\rm at}^{(85)}$, and FWHM $\Delta\nu_{85}$ of the Rb^{85} spin noise spectrum we compute var $\Theta_{\rm FR}^{(85)}$ using Eq. (4.6). These data are shown in Fig. 4.2 as a function of the Rb-vapor density n. The solid line in Fig. 4.2 corresponds to a fit of the data using Eq. (2.42) with κ_{85}^2 as the free parameter and with $N_{85} = 0.72\ nA_{\rm eff}L_{\rm cell}$, here $A_{\rm eff} = 0.054$ cm^2 and $L_{\rm cell} = 3$ cm. From the fit we

Parameter	Value	Unit
Q	0.87	—
$\alpha/(2\pi)$	57.8	$\mathrm{Hz}/(10^{12}\mathrm{cm}^{-3})$
$\beta/(2\pi)$	63	Hz/mW
$\Gamma_0/2\pi$	501	Hz
σ_0	2.4×10^{-12}	cm^2
κ^2	5.0×10^{-4}	—
A_{eff}	0.0544	cm^2
$\Delta\nu_{\mathrm{light}}$	2.4	GHz

Table 4.1: Parameters used in computing η. See text for details.

obtain $\kappa_{85}^2 = 5 \times 10^{-4}$, to be compared with the value of 3.7×10^{-4} obtained by evaluating Eq. (2.41) with a detuning of $\nu' - \nu'_{85} = -20\,\mathrm{GHz}$ and optical linewidth $\Delta\nu_{\mathrm{light}} = 2.4\,\mathrm{GHz}$, and using $\sigma_0 = 2.410^{-12} cm^2$.

Width of the magnetic line

For ^{85}Rb the FWHM width of the magnetic line is $\Delta\nu = \Gamma/\pi$, where $\Gamma = 1/T_2$ is the spin relaxation rate that can be approximated by [120]:

$$\frac{1}{T_2} = \Gamma_0 + \alpha n + \beta P, \tag{4.7}$$

where αn and βP are the contributions from atomic collisions and power-broadening, respectively, with n being the Rb-vapor density, P the optical power of the probe beam, and Γ_0 the spin relaxation due to other mechanisms, including buffer-gas collisions and the finite residence time of the atoms in the light beam.

To estimate the power broadening and collisional-broadening parameters we fit the measured $\Delta\nu_{85}$ using Eq. (4.7). From the fit we obtain a collisional broadening parameter $\alpha/(2\pi) = 57.8\mathrm{Hz}/10^{12} cm^3$, a power-broadening parame-

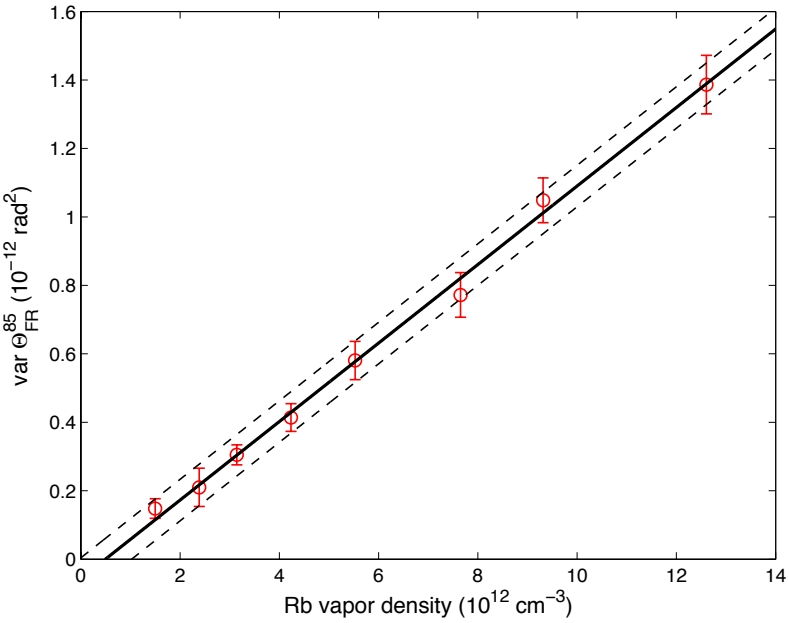

Figure 4.2: var $\Theta_{FR}^{(85)}$ as a function of atomic density for a coherent probe. The solid line indicates a linear fit to the data. Dashed lines show the best fit $\pm 3\sigma$ statistical uncertainty in the fit offset.

ter $\beta/(2\pi) = 63\text{Hz/mW}$, and $\Gamma_0/(2\pi) = 501$ Hz.

4.3.4 SNR

Using equations (4.3), (2.42), (4.6), and (4.7) we obtain the following expression for the SNR $\eta_i \equiv S_{\text{at}}^{(i)}/S_{\text{ph}}$

$$\eta_i = \frac{P}{\hbar\omega}\frac{4Q}{\xi^2}\frac{\sigma_0^2}{A_{\text{eff}}^2}\frac{\kappa_i^2 N_i}{\Gamma}, \tag{4.8}$$

where $N_i = n_i A_{\text{eff}} L_{\text{cell}}$, thus arriving to:

$$\eta_i \equiv \frac{S_{\text{at}}^{(i)}}{S_{\text{ph}}} = \frac{P}{\hbar\omega}\frac{4Q}{\xi^2}\frac{\sigma_0^2}{A_{\text{eff}}^2}\frac{\kappa_i^2 n_i L_{\text{cell}} A_{\text{eff}}}{\Gamma}, \tag{4.9}$$

where $\Gamma = 1/T_2$ is the spin relaxation rate defined above.

From Eqs. (4.9) and (4.7) we see that it is in principle possible to increase η by increasing either the optical probe power or the atomic density. However both of these actions result in additional broadening of the linewidth $\Delta\nu$. As one main use of SNS is to measure relaxation processes in an unperturbed spin system [26, 27], this additional broadening represents a systematic shift of the measured variable (the linewidth) [113]. On the other hand, Eqs. (4.9) and (4.7) predict that squeezing boosts η without additional shifts, providing a quantum advantage irrespective of the other experimental parameters.

4.4 Experimental Setup

The experimental setup is shown schematically in Fig. 4.3 (a) and it has been already described in detail within chapter (3). In this section we recall its main properties.

A polarization-squeezed probe beam is generated as in [37] by combining local oscillator (LO) laser light with orthogonally polarized squeezed vacuum using a parametric oscillator described in [69], cavity locking system as in [104], and a quantum noise lock (to ensure the measured Stokes component is the squeezed component) described in [121, 40]. The probe frequency is stabilized to 20 GHz to the blue of the ^{85}Rb D_1 unshifted line using the system of [105]. Adjusting the LO power changes the probe power P without changing the degree of squeezing. To perform conventional FR-SNS with the coherent LO [66] we simply turn off the squeezer. The effective size of the probe beam is $0.054\,\mathrm{cm}^2$.

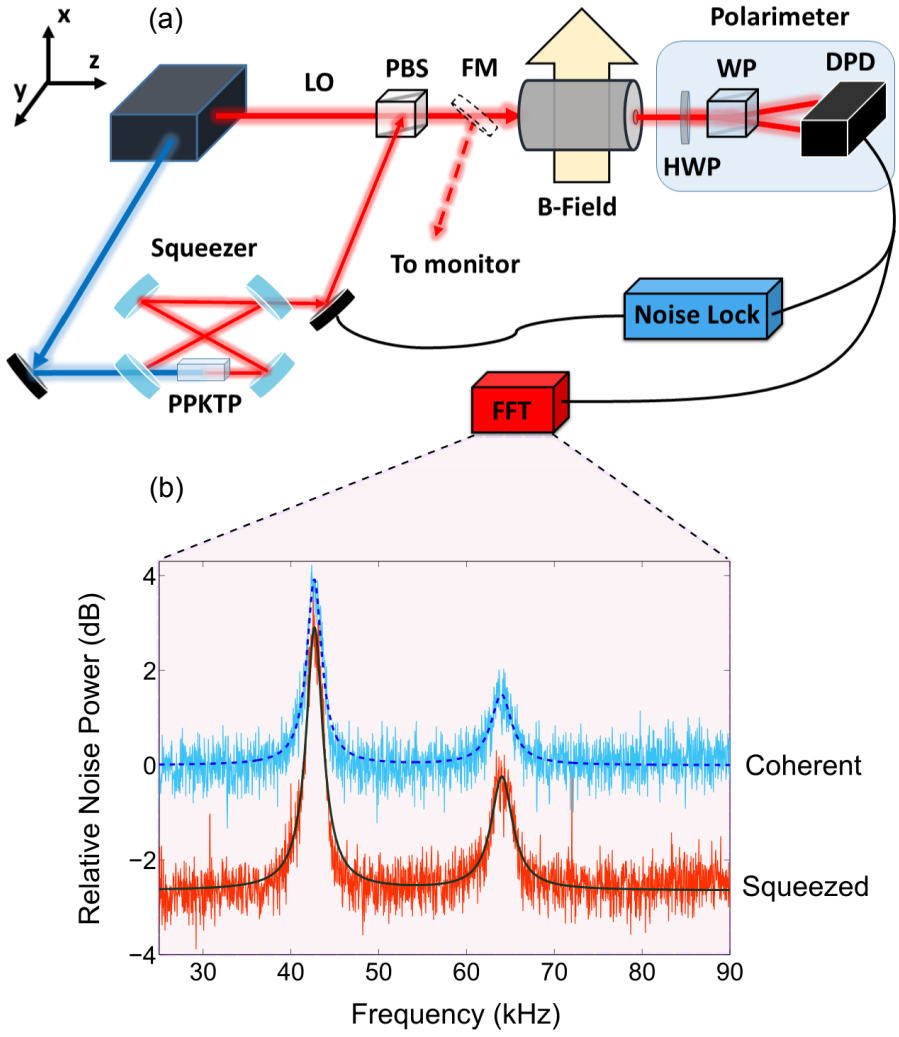

Figure 4.3: **Squeezed-light spin noise spectroscopy. (a) Experimental schematic**. LO - local oscillator, PBS - polarizing beam splitter, DPD - differential photo detector, FM - flip mirror, HWP - half wave-plate, WP - Wollaston prism, FFT - fast Fourier transform analyzer. **(b) SNS Spectra**. Averaged spin noise spectra at $T = 90°$ ($n = 2.4 \times 10^{12}$ cm^{-3}) acquired with coherent probe (cyan) and polarization squeezed probe (red) respectively. The spectra shown are averages of 10 spectra, each representing 0.5 s of acquisition organized into bins of width 10 Hz. 0 dB on the power scale corresponds to -95.57 dBV/Hz at the detector. Dashed and continuous smooth curves show fits by Eq. (4.1) to the coherent and squeezed spectra, respectively. Optical power $P = 2.5$ mW, magnetic field $B_x = 5.6\mu$T.

The atomic system consists of an ovenized cylindrical vapor cell of length $L_{\text{cell}} = 3\,\text{cm}$ and diameter $d = 1\,\text{cm}$, with natural isotopic abundance Rb and 100 Torr of N_2 buffer gas. Density is controlled by oven temperature and calibrated by absorption at 20 GHz detuning. We alternate five-second acquisition periods with electrical heating of the oven. Before the cell, measured squeezing at a sideband frequency of 40 kHz is 3.0 dB, while squeezing after the cell ranges from 2.6 dB to 1.5 dB at the highest density. These numbers are consistent with expected loss of squeezing due to absorption of the off-resonance probe.

We apply a transverse DC field $B_x = 5.6\,\mu\text{T}$ and minimize the gradient $\partial B_x/\partial z$ by minimizing the width of the SNS resonances. The oven and coils are inside four layers of high-permeability magnetic shielding. We detect the probe beam with a polarimeter consisting of a half-waveplate, Wollaston prism and differential photodetector (DPD). The output is recorded by a 24-bit digitizer with 200 kHz sampling rate and a PC computes the power spectrum.

In Fig. 4.3 (b) we show typical spectra using coherent and polarization squeezed probes. As expected from Eq. (4.1) we observe the two atomic noise contributions from ^{85}Rb and ^{87}Rb centered at Larmor frequencies ν_L^{85} and ν_L^{87} above a uniform shot noise background. Squeezing reduces the shot noise level without evident change to the spin noise contribution, resulting into a SNR improvement with unaltered FWHM width.

4.5 Data analysis and results

At any given optical power and atomic density we acquire 100 individual spin noise spectra and fit them with Eq. (4.1) to obtain the parameters S_{ph} and $S_{\text{at}}^{(i)}$,

$\nu_L^{(i)}$, $\Delta\nu_{(i)}$, and the derived $\eta = S_{\rm at}^{(i)}/S_{\rm ph}$, for $i \in \{85, 87\}$. Due to imperfect stability of the quantum noise lock, it is necessary to reject about 10 percentof the traces, identified by the condition $\chi \equiv \int d\nu\, S(\nu) > 1.03\bar{\chi}$, where the integral is taken over a featureless window between $80 - 90$ kHz, not included in the fitting, and $\bar{\chi}$ is the average of χ over the 100 spectra.

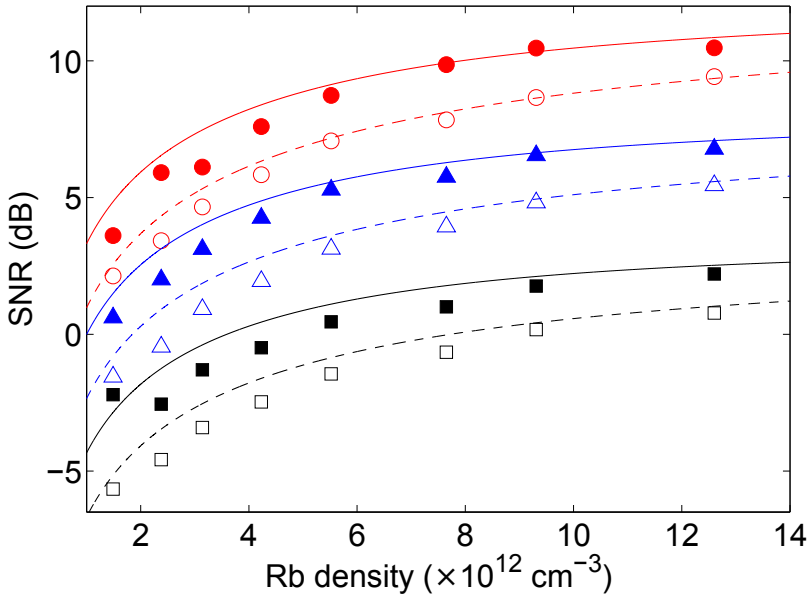

Figure 4.4: **SNR Enhancement**. SNR η versus atomic density for coherent probes (empty markers) and polarization squeezed probes (filled markers), respectively. We show three optical powers of $P = 0.5\,$mW (squares), $P = 1.5\,$mW (triangles) and $P = 4\,$mW (circles). Predicted η from Eq. (4.9) is plotted for coherent (dashed lines) and squeezed (continuous lines) probing, taking into account the reduction of squeezing versus density due to absorption at the probe frequency. The discrepancy between theoretical curves and experimental data is due to uncertainty on density estimation.

In Fig. 4.4 we show measured ^{85}Rb SNR versus n, the Rb number density, for coherent and squeezed probes at $P = 500\,\mu$W and $P = 4\,$mW, which bound our investigated power range, and at the intermediate $P = 1.5\,$mW. The temperature range is $T = 85\,^\circ$C – $120\,^\circ$C. As expected from Eq. (4.9), the SNR increases with both increasing density and increasing power. Squeezing enhances the SNR by a

factor ranging from 2.6 dB at $n = 1.5 \times 10^{12}\text{cm}^{-3}$ to 1.5 dB at $n = 1.3 \times 10^{13}\text{cm}^{-3}$, with the difference due to greater absorption at higher density. This latter number is higher than the densities used in other alkali SNS works [26, 27, 47], and at this density we observe collisional broadening $\alpha n/(2\pi) = 760\,\text{Hz}$, larger than $\Gamma_0/(2\pi) = 501\,\text{Hz}$. We are thus in a regime where a feature of interest (the linewidth) is already strongly disturbed. Analogous observations apply to the investigated probe power range. In this sense the regime we investigate is fully practical for SNS applications [66, 25]. Moreover, the model described in section (4.3) shows that the benefit of squeezing extends until the optical absorption becomes strong and the squeezing is lost. The theoretical SNR for squeezed and coherent probes (curves of Fig. 4.4) converge at a density of $n \approx 1.3 \times 10^{14}$ cm^{-3} (temperature larger than $T = 160°$), much above the investigated and practical range of interest. This is our first main result: polarization squeezing significantly improves the SNR of spin noise spectroscopy over the full practical range of power and density without any detrimental effect.

Furthermore, in Fig. 4.5 we show ^{85}Rb SNR η_{85} and FWHM linewidth $\Delta\nu_{85}$ versus optical power for three different experimental situations: $n = 0.5 \times 10^{13}\text{cm}^{-3}$ (squeezed only) and, with roughly twice the density, at $n = 0.9 \times 10^{13}\text{cm}^{-3}$ (coherent and squeezed). At the higher density, squeezing improves the SNR with respect to the coherent probe without significantly changing the linewidth. At the lower density, squeezing gives the same SNR as the coherent probe gives with the higher density, but with significantly less perturbation of the linewidth. These behaviors are observed over the full investigated power range.

A similar behavior occurs if we compare SNR and linewidth versus atomic density at different probe power levels. Fig. 4.5 (a) already shows that squeezing

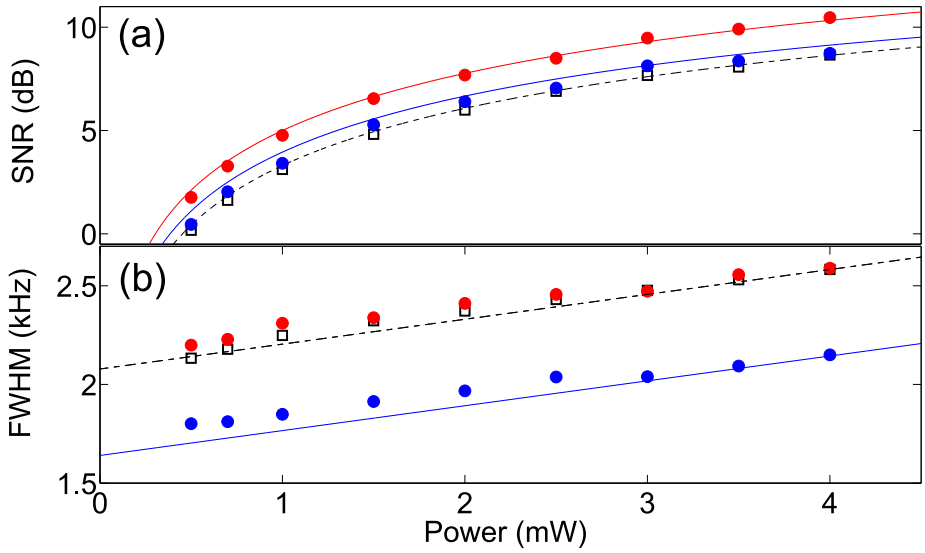

Figure 4.5: **Collisional broadening reduction (a)** SNR η versus optical power for coherent (empty black squares) and polarization squeezed (filled red circles) probing at $n = 0.9 \times 10^{13}$ cm^{-3} and just for squeezed probe (filled blue circles) at lower density $n = 0.5 \times 10^{13}$ cm^{-3}. Theoretical SNR from Eq. (4.9) is shown for coherent (dashed lines) and squeezed (continuous lines) probing. **(b)** FWHM linewidth $\Delta\nu_{85}$ vs probe power for the same conditions of (a). Theoretical FHWM widths from Eq. (4.7) are plotted for coherent (dashed line) and squeezed (continuous line) probing, respectively.

allows us to get the same classical SNR by using about half of the power, resulting in a reduced power broadening. For completeness in Fig. 4.6 we show the FWHM linewidth versus Rb density for $P = 2$ mW and $P = 4$ mW where the SNR with squeezing at $P = 2$ mW is equal to the SNR with coherent probing at $P = 4$ mW. The linewidth reduction with power is smaller than that seen Fig. 4.5 (b), because the collisional broadening is greater than the broadening due to probe scattering and, in these experimental conditions, dominates the broadening. In Figs. 4.5 and 4.6 we show our second main result: due to line broadening reduction, squeezing can reduce systematic errors at no cost to figures of merit such as statistical sensitivity. To our knowledge, this is both the first description of the possibility to reduce systematic errors with squeezing, and its first observation in experiment.

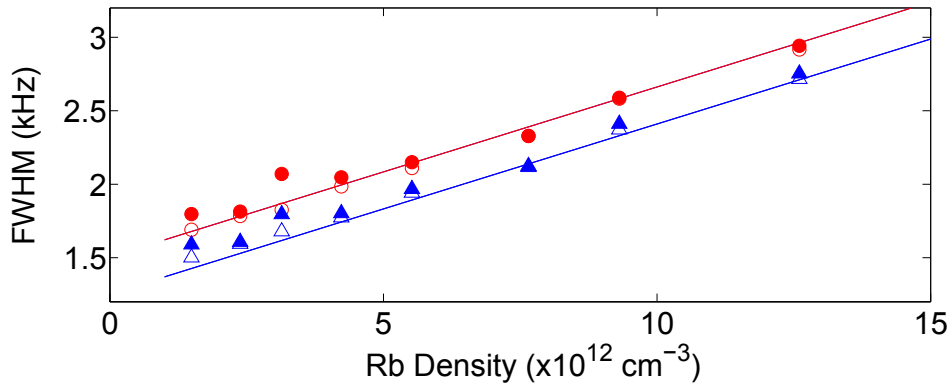

Figure 4.6: **Power broadening reduction** FWHM linewidth $\Delta\nu_{85}$ vs Rb density for coherent (empty markers) and polarization squeezed (filled markers) probing at optical powers of $P = 4$ mW (red circles) and $P = 2$ mW (blue triangles). Theoretical FHWM widths from Eq. (4.7) are plotted.

4.6 Conclusions

We have studied the application of polarization-squeezed light to spin noise spectroscopy of atomic ensembles over the full practical range of density and probe power. We observe that squeezing improves the signal-to-noise ratio by an amount comparable to the applied squeezing, in contrast to prior experiments [43] that showed the opposite behavior: increased measurement noise due to squeezing above a critical density. We demonstrate that by using a crystal-based squeezer and off-resonant probing of an un-polarized ensemble, differently from [43, 45], optical and atomic quantum noise add incoherently without any coupling. Moreover, squeezing improves the trade-off between statistical noise and line broadening by giving performance not available with classical probes at any power level.

Our results provide clear evidence that squeezing can improve Faraday-rotation-based SNS measurements, with a broad range of applications in atomic and solid state physics [66, 25]. This advantage over the full practical parameter range

for SNS is promising for similar advantages in high-performance magnetometers, gravimeters, and clocks.

Chapter 5

Quantum limits of noise spectroscopies

In this chapter we study noise spectroscopy from the perspective of estimation theory and, considering optically-detected noise spectroscopies, derive quantum limits for the sensitivity of the technique, which is identified with the covariance of the fit parameters. The question we want to answer here is: what are the shot noise and atomic noise contributions to the uncertainty in the fit parameters? We note that this is *not* the same question as "what is the shot noise contribution to $S(\nu)$" which is usually asked in works about squeezing. That question is the interesting one if you want to consider for example a communications or sensing scenario in which you expect a signal at a given frequency ν and you want to know how much noise background there is at that frequency. This is different in two ways: First, as described in the previous chapter (4), our "signal" is actually a noise level, so what counts as our "noise" is the *uncertainty* in the power noise

spectrum. Second, we are looking for the covariance on fit parameters, which will end up combining uncertainty from different parts of the spectrum. Because of the quantum origin of such uncertainty, we will refer to the covariance bound as standard quantum limit (SQL). The data for spin-noise spectroscopy in natural abundance Rb vapor, obtained from the measurements described in the previous chapter (4), are found to agree very well with theory, demonstrating spin noise spectroscopy at the SQL. We study the high-density and high-probe-power regimes, giving quantum limits also in optimized regimes. We finally confirm the shot noise limitation to the SQL of the technique, by reporting parameter estimation below the SQL via polarization squeezing of the probe beam, in agreement with theoretical predictions. The results presented in this chapter are being prepared for submission to a peer-reviewed journal.

5.1 Theory of noise in fitting power spectra

We begin with general statistical observations. Any noise spectroscopy records a dynamical variable $P(t)$, and derives information from the power spectrum $S(\nu)$. For simplicity, we consider the discrete-time version $S_i \equiv S(\nu_i) \equiv |\tilde{P}(\nu_i)|^2$, where $\tilde{P}$ is the discrete Fourier transform of $P(t)$, sampled at times $t = \Delta, 2\Delta, \ldots, T$, so that $\nu_i = i\nu_T$ are the centres of the frequency bins of width $\nu_T \equiv 1/T$. Note that this describes the single-sided power spectral density. With the assumption that $P(t)$ is stationary, i.e. its statistics are t-independent, a simple calculation finds

$$\mathrm{cov}(S_i, S_j) = \langle S_i \rangle^2 \delta_{ij} \tag{5.1}$$

where δ indicates the Kronecker symbol. Eq. (5.1) describes a unit signal-to-noise ratio for S_i, independent of its value, in marked contrast to most physical estimation problems. To reduce the uncertainty of S, two averaging procedures are typically applied: a simple averaging of $N_{\rm ave}$ independent spectra, and coarse-graining of the spectrum, averaging $\nu_{\rm bin}/\nu_T$ adjacent values of S_i to obtain $\bar{S}_j \equiv \langle S_i \rangle_{i\in\mathcal{B}_j}$, where the brackets indicate an average over $\mathcal{B}_j$, the range of frequencies in the jth bin. By simple averaging, and using Eq. (5.1), we find

$$\mathrm{var}(\bar{S}_i) = \frac{\nu_T}{N_{\rm ave}\nu_{\rm bin}}\langle \bar{S}_i \rangle^2 \equiv \frac{1}{N}\langle \bar{S}_i \rangle^2. \tag{5.2}$$

By the central limit theorem, increasing N drives $\bar{S}_i$ toward a normal distribution.

Spectroscopic information is obtained by fitting the power spectrum $\{S_i\}$ with a generic model $f(\nu, \mathbf{v})$, where $\mathbf{v}$ is a vector of parameters. As with S, we will write $f_i \equiv f(\nu_i)$. We consider a maximum likelihood fit, which, since the model is gaussian, is equivalent to minimizing χ^2, defined as:

$$\chi^2(\mathbf{v}) \equiv \sum_i \frac{(f_i(\mathbf{v}) - S_i)^2}{\sigma_i^2} \tag{5.3}$$

where $\sigma_i \equiv \sigma(\nu_i)$ is the frequency dependent standard deviation of $\{S_i\}$ around the mean value $\mu_i = \bar{S}_i = f_i$, by assuming that f is the correct model, so that $f_i = \bar{S}_i$. For a single spectrum and no averaging, as for Eq. (5.1), the standard deviation of $\{S_i\}$ has exactly the same frequency dependence of the spectrum $S(\nu)$ so that $\sigma_i = \mu_i$. The chi-squared minimization is achieved when

$$\partial_j \chi^2(\mathbf{v})\Big|_{\mathbf{v}=\hat{\mathbf{v}}} = 0 \tag{5.4}$$

where ∂_j indicates $\partial/\partial v_j$ and v_j is a component of the parameters vector $\mathbf{v}$. The

carat over $\hat{\mathbf{v}}$ indicates the estimator of $\mathbf{v}$. From here on, we suppress the $\mathbf{v}$ dependence in $f_i(\mathbf{v})$ and we use the Einstein summation convention. Applying the derivative, the optimization condition is

$$\left.\frac{(f_i - S_i)\partial_j f_i}{\sigma_i^2}\right|_{\mathbf{v}=\hat{\mathbf{v}}} = \left.\frac{\partial_j \sigma_i (f_i - S_i)^2}{\sigma_i^3}\right|_{\mathbf{v}=\hat{\mathbf{v}}} \tag{5.5}$$

We can apply the variational principle to understand how a small error in S_i i.e. $S_i = \bar{S}_i + \delta S_i$ produces a corresponding error in the estimator $\hat{v_i} = \bar{v_i} + \delta v_i$. By assuming that the fit function correctly describes the mean spectrum, i.e. $f - \bar{S} = 0$, to mantain the condition of Eq. (5.5) we must have:

$$\frac{(\partial_k f_i)(\partial_j f_i)}{\sigma_i^2}\delta\hat{v_k} = \frac{\partial_j f_i}{\sigma_i^2}\delta S_i \tag{5.6}$$

which is a general result for a noise spectrum $S(\nu)$ that is fitted with the right model $f_i = \bar{S}_i$ and that satisfies Eq. (5.1). In order to obtain an analytical expression for the covariance matrix Γ of the estimator $\hat{\mathbf{v}}$, we define a non-square matrix L:

$$L_{ij} \equiv \frac{\partial_j f_i}{\sigma_i}. \tag{5.7}$$

and, by defining the matrix $M \equiv LL^T$, i.e. $M_{jk} \equiv L_{ji}L_{ki}$, we can rewrite equation (5.6) as:

$$M_{jk}\delta\hat{v}_k = L_{ji}\frac{\delta S_i}{\sigma_i} \tag{5.8}$$

with solution

$$\delta\hat{v}_k = M^{-1}_{kj}L_{ji}\frac{\delta S_i}{\sigma_i} \tag{5.9}$$

Eq. (5.9) relates the uncertainty on the spectrum, i.e. the noise on the noise power, with the uncertainty on the fit parameters.

5.1.1 Theoretical covariance of fit parameters

We now want to calculate the covariance matrix of $\hat{\mathbf{v}}$:

$$\begin{aligned}\Gamma_{jk} &\equiv \langle \hat{v_j}\hat{v_k}^T\rangle - \langle \hat{v_j}\rangle\langle \hat{v_k}^T\rangle = \langle \delta\hat{v_j}\delta\hat{v_k}^T\rangle \\ &= \Big\langle \frac{M^{-1}_{jl}L_{lm}\delta S_m (M^{-1}_{kn}L_{np}\delta S_p)^T}{\sigma_m\sigma_p}\Big\rangle \\ &= \Big\langle M^{-1}_{jl}L_{lm}L_{pn}M^{-1}_{nk}\frac{\delta S_m \delta S_p^T}{\sigma_m\sigma_p}\Big\rangle \end{aligned} \tag{5.10}$$

By using the fact that δS_i are independent random variables and applying Eq. (5.1) we finally get:

$$\begin{aligned}\Gamma_{jk} &= M^{-1}_{jl}L_{lm}L_{pn}M^{-1}_{nk}\delta_{mp} \\ &= M^{-1}_{jl}L_{lm}L_{mn}M^{-1}_{nk} \\ &= M^{-1}_{jl}M^{-1}_{ln}M^{-1}_{nk} = M^{-1}_{jk}\end{aligned} \tag{5.11}$$

On the other hand, the elements M_{jk} of the matrix $M \equiv LL^T$ are given by:

$$\begin{aligned}M_{jk} &= \sum_i \frac{(\partial_j f_i)(\partial_k f_i)}{\sigma_i^2} \\ &= \frac{1}{\delta\nu_T}\sum_i \frac{(\partial_j f_i)(\partial_k f_i)}{\sigma_i^2}\delta\nu_T \\ &= \frac{1}{\delta\nu_T}\int_{\nu_1}^{\nu_2}\frac{(\partial_j f(\nu))(\partial_k f(\nu))}{f^2(\nu)}d\nu\end{aligned} \tag{5.12}$$

where ν_1, ν_2 delimit the frequency range over which the fit $f(\nu)$ is performed and, in the last step, we use $\sigma_i = f_i$ and we consider a continuous spectrum.

The described model is very general and can be applied to any noise spectroscopy experiment. Giving a noise spectrum $S(\nu)$ that satisfies Eq. (5.1) and

an accurate model $f(\nu)$ that depends on a parameters vector $\mathbf{v}$, by combining Eq. (5.12) and Eq. (5.11) one can obtain the analytical covariance matrix $\Gamma = M^{-1}$ of the parameters vector. In particular, the diagonal terms of Γ are the variances of the fit parameter outputs, while the off-diagonal terms give information on their correlations. Hence, the described model provides a powerful tool for a *a priori* knowledge on the experimental conditions that optimize the information achievable through noise spectroscopy, e.g. that minimize the variance on a specific fit parameter.

It is worth noting that the theoretical result, which is obtained by combining Eqs. (5.11) and (5.12), is valid for a continuous spectrum and represents an asymptotic limit, a maximum-likelihood estimation (MLE), for the discrete spectrum described by a multivariate normal distribution with mean $\mu_i = \bar{S}_i = f(\nu_i)$ and covariance matrix $\Sigma_{ij} = N^{-1} f^2(\nu_i)\delta_{ij}$, for which the Cramer-Rao [122, 123] bound is $\Gamma \geq \mathcal{I}^{-1}$ and the Fisher information I is given by [124]:

$$\begin{aligned} \mathcal{I}_{kl} &= \sum_i (\partial_k \mu_i)\Sigma^{-1}(\partial_l \mu_i) + \frac{1}{2}\mathrm{Tr}\left[\Sigma^{-1}(\partial_k \Sigma)\Sigma^{-1}(\partial_l \Sigma)\right] \\ &= N\sum_i (\partial_k f_i) f_i^{-2}(\partial_l f_i) + \frac{1}{2}\sum_i f_i^{-4}(\partial_k f_i^2)(\partial_l f_i^2) \\ &= (N+2)\sum_i f_i^{-2}(\partial_k f_i)(\partial_l f_i). \end{aligned} \tag{5.13}$$

For the asymptotic case, i.e., for large N as defined in Eq. (5.2), the bound becomes $\Gamma = \mathcal{I}^{-1}$ and Eq. (5.13) becomes equal to the continuous limit of Eq. (5.11). In our experiment we acquire individual spectra, i.e. $N_{\mathrm{ave}} = 1$, and we perform a decimation with $\nu_{\mathrm{bin}}/\nu_T = 50$. Then, for our data analysis, $N = 50$ is large enough so that Eqs. (5.13) and (5.11) give the same results.

5.2 Optical noise spectroscopy

We now specialize to the case of optically-detected noise spectroscopy, as in [26, 125, 126, 42, 10]. A dimensionless optical degree of freedom θ, e.g. optical phase, polarization angle or pointing direction, has initial value $\theta^{(\mathrm{in})}(t)$, understood to include fluctuations due to shot noise. After passing through the system under study this variable is $\theta^{(\mathrm{out})}(t) = \phi(t) + \theta^{(\mathrm{in})}(t)$, where the change $\phi(t)$ is proportional to the noisy quantity of interest, e.g. refractive index, magnetization, or distribution of refractive index across the beam profile. In the linear regime, the detected power, typically from a differential measurement, is

$$P(t) = \eta\hbar\omega\Phi[\phi(t) + \theta^{(\mathrm{in})}(t)] \tag{5.14}$$

where Φ is the mean flux of photons reaching the detector and η is the detector quantum efficiency. A Fourier transform of $P(t)$ provides the power noise spectrum $S(\nu)$ that, trough the fluctuation-dissipation theorem, should carry all the information about the system under investigation.

5.2.1 Specifics of atomic response

We now specialize to resonant noise, e.g. spin noise subject to Larmor precession [26] or trapped objects in optical tweezers [127]. In particular, we want to test the model of Eq. (5.11) against the experiment described in the previous chapter (4), in which we detect spontaneous spin fluctuations of a dense Rb vapor via Faraday rotation of a coherent, or polarization squeezed, off-resonance probe beam [72]. Taking the parameters vector $\mathbf{v} = (S_{\mathrm{ph}}, \nu_{85}, S_{\mathrm{at}}^{85}, \Delta\nu_{85})$, where ν_{85} is the resonance frequency, S_{at}^{85} is the atomic noise contribution and $\Delta\nu_{85}$ is the linewidth of the

^{85}Rb resonance, we can fit the frequency portion of noise spectrum $S(\nu)$ around ν_{85} with the Lorentzian funtion:

$$f(\nu) = S_{\rm ph} + S_{\rm at}^{85} \frac{(\frac{\Delta\nu_{85}}{2})^2}{(\nu - \nu_{85})^2 + (\frac{\Delta\nu_{85}}{2})^2} \tag{5.15}$$

that is just the ^{85}Rb contribution of the double Lorentzian function already given in Eq. (4.1). Then, for simplicity, from now on we write $S_{\rm at}^{85} \equiv S_{\rm at}$, $\Delta\nu_{85} \equiv \Delta\nu$ and $\nu_{85} \equiv \nu_L$.

From the fit function of Eq. (5.15) we want to derive the theoretical 4×4 covariance matrix $\Gamma = M^{-1}$, defined in Eq. (5.11), for the parameters $\mathbf{v} = (S_{\rm ph}, \nu_L, S_{at}, \Delta\nu)$ and compare it against the experimental sample covariance matrix. First, we need to calculate the M-matrix of Eq. (5.12) through the partial derivatives of the fit function with respect to the fit parameters:

$$\partial_{[S_{\rm ph}]} f(\nu) = 1 \tag{5.16}$$

$$\partial_{[\nu_L]} f(\nu) = \frac{8 S_{at} \Delta\nu^2 (\nu - \nu_L)}{(\Delta\nu^2 + 4(\nu - \nu_L)^2)^2} \tag{5.17}$$

$$\partial_{[S_{at}]} f(\nu) = \frac{\Delta\nu^2}{\gamma^2 + 4(\nu - \nu_L)^2} \tag{5.18}$$

$$\partial_{[\Delta\nu]} f(\nu) = \frac{8 S_{at} \Delta\nu (\nu - \nu_L)^2}{(\Delta\nu^2 + 4(\nu - \nu_L)^2)^2} \tag{5.19}$$

We note that the above results are independent of the photon shot noise contribution $S_{\rm ph}$. On the other hand, in the calculation of the covariance matrix Γ, the shot noise enters into the denominator of Eq. (5.12) through the uncertainty on the noise spectrum $\sigma(\nu) = f(\nu) = \sigma_{\rm ph} + \sigma_{\rm at}(\nu)$, where $\sigma_\theta = S_{\rm ph}$ and $\sigma_{\rm at}(\nu) = S_{at} \frac{(\frac{\Delta\nu}{2})^2}{(\nu - \nu_L)^2 + (\frac{\Delta\nu}{2})^2}$ are the frequency independent (shot noise) and frequency-dependent (atomic noise) contributions to the uncertainty. Moreover,

in our experimental conditions [72] (see chapter (4)), the Larmor frequency is a constant while the other fit parameters $(S_{\rm ph}, S_{\rm at}, \Delta\nu)$ are functions of optical power P and Rb density n so that, from now on, we conveniently express the covariance matrix itself as $\Gamma = \Gamma(n, P)$. Exact expressions of the parameters $(S_{\rm ph}, S_{\rm at}, \Delta\nu)$ have been already given in Eqs. (4.3), (4.6) and (4.7), respectively.

5.3 Analytical results

By combining Eqs. (4.3,4.6-4.7) with Eqs. (5.16-5.19) and solving the integrals of Eqs. (5.12) over the frequency range $\nu_1 = 33$ kHz - $\nu_2 = 52$ kHz, we can analitically calculate the theoretical covariance matrix $\Gamma^{\rm th}(n, P)$, as a function of optical power and atomic density. A sample of these results is given at the end of this section for fixed values of both density and mean power. Furthermore, because of the quantum origin of the uncertainty on the spin noise spectrum, from now on we refer to the statistical limit $\Gamma^{\rm th}(n, P)$, defined by Eq. (5.11), as standard quantum limit (SQL) of noise spectroscopy.

In Fig. (5.1) we show 2D contour-plots of the diagonal terms $\Gamma^{\rm th}_{22}(n, P)$ and $\Gamma^{\rm th}_{44}(n, P)$, i.e. the variances of the estimated Larmor frequency ν_L and resonance linewidth $\Delta\nu$, versus atomic density and optical power over the parameter range $(1 \times 10^{12}$ cm^{-3} to 2×10^{13} cm$^{-3}) \otimes (1m$W to 20 mW). In the low-density/low-power regime both variances decrease by increasing both degrees of freedom, until reaching an optimal region, i.e. minimum variance. By further increasing either atomic density or probe power, an inversion of the scaling is visible and both variances rise again. In a 2D plot this scaling results in a guitar-plectrum-shaped optimal area for the variances of $(\nu_L, \Delta\nu)$, which are reported in unit of (Hz^2) in

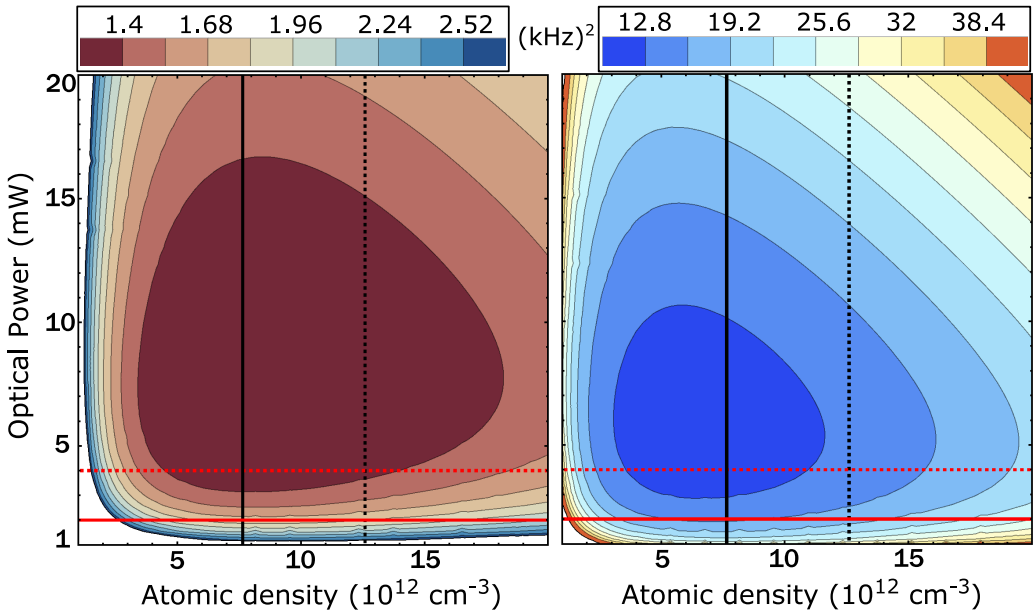

Figure 5.1: **Analytical results. (Left)** Covariance matrix term $\Gamma^{\rm th}_{22}(n, P)$ versus atomic density and optical probe power. **(Right)** Covariance matrix term $\Gamma^{\rm th}_{44}(n, P)$ in the same parameters space. The upper limits of the experimental investigated range are $P = 4$ mW (dashed red line) and ($n = 12.6\ 10^{12}$ cm^{-3}) (dashed black line). Sample data are shown in Figs. (5.3) and (5.4) for $P = 2$ mW (continuous horizontal red line) and $n = 7.65 * 10^{12}$ cm^{-3} (continuous vertical black line) (see text).

the legends of Fig. (5.1). On the other hand, in Fig. (5.2) we show 2D contour-plots of the variances of the estimated atomic $S_{\rm at}$ and shot noise $S_{\rm ph}$ contributions to the power spectrum of Eq. (5.15), given respectively by the covariance matrix diagonal terms $\Gamma^{\rm th}_{33}(n, P)$ and $\Gamma^{\rm th}_{11}(n, P)$, respectively. For these fit parameters the theoretical variance increases monotonically with both power and density, without showing an optimal region or an inversion trend within the investigated parameter range.

The diagonal terms of the covariance matrix, i.e. the variances of the fit parameters, are probably of greatest practical interest because they are the variances of parameters that have been estimated in state-of-the-art SNS experiments for

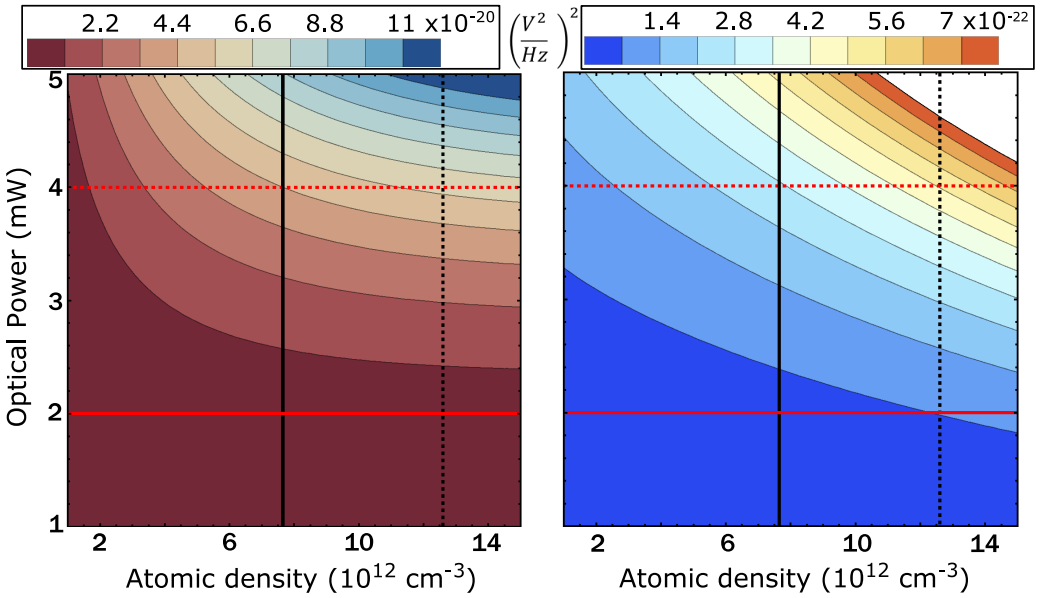

Figure 5.2: **Analytical results. (Left)** Covariance matrix term $\Gamma^{\rm th}_{33}(n, P)$ versus atomic density and optical probe power. **(Right)** Covariance matrix term $\Gamma^{\rm th}_{11}(n, P)$ in the same parameters space. See caption of Fig. 5.1 for horizontal and vertical lines legend.

measuring g-factors, nuclear spin, isotope abundance ratios and relaxation rates of alkali atoms [26, 27] as well as g-factors, relaxation times and doping concentration of electrons in semiconductors [28, 106, 107, 108, 109]. However, here we are also calculating the covariances of the fit parameters that might be important to study correlations between different parameters. For completeness, we compare full theoretical and experimental covariance matrices for fixed values of power $P = 2$ mW and atomic density $n = 7.65 \times 10^{12}$ cm^{-3}. In Figs. (5.1) and (5.2) these values are indicated by horizontal and vertical continuous lines, respectively, and they have been chosen for comparison with the data (see next sections (5.4) and (5.5). In the following we report the theoretical covariance matrix:

$$\Gamma^{\mathrm{th}} = \begin{pmatrix} 0.45\times10^{-22}\,(\mathrm{V^2/Hz})^2 & 0.31\times10^{-12}\,\mathrm{V^2} & 0.78\times10^{-12}\,(\mathrm{V^2/Hz})^2 & -4.82\times10^{-10}\,\mathrm{V^2} \\ 0.31\times10^{-12}\,\mathrm{V^2} & 1741.4\,\mathrm{Hz^2} & 0.32\times10^{-12}\,\mathrm{V^2} & -2.68\times10^{-12}\,\mathrm{Hz^2} \\ 0.78\times10^{-12}\,(\mathrm{V^2/Hz})^2 & 0.32\times10^{-12}\,\mathrm{V^2} & 0.49\times10^{-20}\,\mathrm{V^2} & -66.50\times10^{-10}\,\mathrm{V^2} \\ -4.82\times10^{-10}\,\mathrm{V^2} & -2.68\times10^{-12}\,\mathrm{Hz^2} & -66.50\times10^{-10}\,\mathrm{V^2} & 15\,490.8\,\mathrm{Hz^2} \end{pmatrix}$$

and its standard deviation:

$$\sigma^{\mathrm{th}} = \begin{pmatrix} 0.64\times10^{-23}\,(\mathrm{V^2/Hz})^2 & 27.9\times10^{-12}\,\mathrm{V^2} & 0.48\times10^{-12}\,(\mathrm{V^2/Hz})^2 & 0.96\times10^{-10}\,\mathrm{V^2} \\ 27.9\times10^{-12}\,\mathrm{V^2} & 246.271\,\mathrm{Hz^2} & 292.1\times10^{-12}\,\mathrm{V^2} & 519.38\times10^{-12}\,\mathrm{Hz^2} \\ 0.47\times10^{-12}\,(\mathrm{V^2/Hz})^2 & 292.1\times10^{-12}\,\mathrm{V^2} & 0.07\times10^{-20}\,\mathrm{V^2} & 10.96\times10^{-10}\,\mathrm{V^2} \\ 0.96\times10^{-10}\,\mathrm{V^2} & 519.38\times10^{-12}\,\mathrm{Hz^2} & 10.96\times10^{-10}\,\mathrm{V^2} & 2190.73\,\mathrm{Hz^2} \end{pmatrix}$$

In order to facilitate the reader in the comparison against the experiment, here we also report the experimental sample covariance matrix Γ^{exp}, whose calculation is described in section (5.4), for same power and density values:

$$\Gamma^{\mathrm{exp}} = \begin{pmatrix} 0.45\times10^{-22}\,(\mathrm{V^2/Hz})^2 & 5.22\times10^{-12}\,\mathrm{V^2} & 0.39\times10^{-12}\,(\mathrm{V^2/Hz})^2 & -4.83\times10^{-10}\,\mathrm{V^2} \\ 5.22\times10^{-12}\,\mathrm{V^2} & 2030.6\,\mathrm{Hz^2} & 977.13\times10^{-12}\,\mathrm{V^2} & -1514.33\times10^{-12}\,\mathrm{Hz^2} \\ 0.39\times10^{-12}\,(\mathrm{V^2/Hz})^2 & 977.13\times10^{-12}\,\mathrm{V^2} & 0.49\times10^{-20}\,\mathrm{V^2} & -63.51\times10^{-10}\,\mathrm{V^2} \\ -4.83\times10^{-10}\,\mathrm{V^2} & -1514.33\times10^{-12}\,\mathrm{Hz^2} & -63.51\times10^{-10}\,\mathrm{V^2} & 15\,635.3\,\mathrm{Hz^2} \end{pmatrix}$$

The theoretical covariance matrix Γ^{th} has negative correlations between the resonance linewidth and the other three fit parameters, while the off-diagonal terms that do not involve $\Delta\nu$ are positive, indicating positive correlations among $(\nu_L, S_{\mathrm{ph}}, S_{\mathrm{at}})$. This correlation property holds over all the parameter range (1×10^{12} cm^{-3} to 2×10^{13} cm^{-3}) $\otimes$ ($1m$W to 20 mW) used for the analytical calculations.

The standard deviation σ^{th} is calculated by knowing that the sample covariance matrix Γ of a sample from a multivariate normal distribution follows the Wishart probability density function [128]:

$$P(\Gamma^{\mathrm{th}}) = \det\Gamma^{(m-p-1)/2} e^{-\frac{\mathrm{Tr}[\Gamma^{\mathrm{th}}\Gamma]}{2}} \tag{5.20}$$

with sample size $m = 100$, number of variables $p = 4$ (see section (5.4) for sample data analysis), mean value $\Gamma^{\rm th}$ and variance $\mathrm{var}(\Gamma^{\rm th}) = (\sigma^{\rm th})^2$, where for $\mathrm{var}(M)$ of a generic matrix M we mean the matrix with elements $[\mathrm{var}(M)]_{ij} = \mathrm{var}(M_{ij})$ and for M^2 we mean the matrix with elements $[(M)^2]_{ij} = M_{ij}^2$.

We note that the sample covariance matrix agrees reasonably well with the predicted covariance matrix. The difference $|\Gamma_{ij}^{\rm th} - \Gamma_{ij}^{\rm exp}|$ is $\sim \sigma_{ij}^{\rm th}$ for most elements of the matrix, and the largest discrepancy is $3.3\sigma^{th}$. Comparing also $\Gamma^{\rm th}$, σ^{th} and $\Gamma^{\rm exp}$ obtained for other powers and number densities (not shown), this is a typical result. In the next section (5.4) we compare the experimental diagonal terms $\Gamma_{ii}^{\rm exp}$ against theory as a function of atomic density and optical power and we demonstrate performance of SNS at the SQL.

5.4 Experimental results

As described in both [72] and chapter (4), we experimentally investigated the parameter range $(1.49 \times 10^{12}$ cm^{-3} to 12.6×10^{12} cm$^{-3}) \otimes (500\mu$W to 4 mW) that represents a portion of the, just described, theoretical parameter range and its upper limits are indicated by horizontal ($P = 4$ mW) and vertical ($n = 12.6 \times 10^{12}$ cm^{-3}) dashed lines in Figs. (5.1) and (5.2). Here we show that the experimental range is sufficient to end up on the minimum variance region of both Larmor frequency and resonance linewidth parameters, as predicted in Fig. (5.1).

At any fixed atomic density and optical power, we acquire 100 spin noise spectra and we fit each spectrum with the Lorentzian function of Eq. (5.15) over the spectral region $33-52$ kHz around the ^{85}Rb resonance at $\nu_L = 42.6$ kHz. After performing all the fits, we end up with 100 samples of the vector $\mathbf{v}$. Then, we can

estimate the mean values $\bar{v}_i = (\sum_{k=1}^{100} v_i^{(k)})/100$ for all the vector components as well as the experimental signal-to-noise ratio of Eq. (4.9), as reported in chapter (4) [72]. Here we are interested on the covariance of the fit parameters and we want to test the theoretical model. In order to do that, we obtain the experimental sample covariance matrix $\Gamma^{\rm exp}(n, P)$ by applying $\Gamma_{ij}^{\rm exp}(n, P) = {\rm cov}(v_i, v_j)$ to our sample of multivariate random variables. An example of the full sample covariance matrix for values of power $P = 2$ mW and atomic density $n = 7.65 \times 10^{12}$ cm^{-3} has been already given in the previous section (5.3), where we showed agreement between theory and experiment in units of the theoretical error $\sigma^{\rm th}$. Here we report data for the diagonal terms $\Gamma_{ii}^{\rm exp}$ and we calculate their standard errors by applying the k-statistics approach [129] to the individual distributions of the components of the parameters vector $\mathbf{v}$. For the v_i parameter the k-statistics can be given in terms of the sums of the r-th powers of the distribution as:

$$S_r = \sum_{k=1}^{m} (v_i^{(k)})^r \tag{5.21}$$

where $m = 100$ is again the sample size. Then, following the notation of [129], we can calculate the unbiased estimators (k_2, k_4) of the cumulants (κ_2, κ_4) of the given distribution, which are given by:

$$k_2 = \frac{m(S_2 - S_1^2)}{m(m-1)} \tag{5.22}$$

and

$$k_4 = \frac{-6S_1^4 + 12mS_1^2S_2 - 3m(m-1)S_2^2 - 4m(m+1)S_1S_3 + m^2(m+1)S_4}{m(m-1)(m-2)(m-3)} \tag{5.23}$$

Then, an unbiased estimator for var(k_2), which is the variance of the estimator of

the variance of the distribution, is given by ([129] pp. 189-190):

$$\mathrm{var}(\Gamma_{ii}^{\mathrm{exp}}) = \mathrm{var}(k_2) = \frac{2nk_2^2 + (n-1)k_4}{n(n+1)} \tag{5.24}$$

From Eq. (5.24) we obtain the standard error of the diagonal term of the sample covariance matrix $\Gamma_{ii}^{\mathrm{exp}}$. By performing this calculation with $i = 1$ to 4 we get the error bars that are shown in Figs. (5.3) and (5.4).

In Fig. (5.3) we show the experimental covariance terms $\Gamma_{22}^{\mathrm{exp}}(n)$ (top) and $\Gamma_{44}^{\mathrm{exp}}(n)$ (bottom) versus the atomic density, at the sample optical power $P = 2$ mW (indicated by a continuous red line in Figs. (5.1) and (5.2)). The agreement with the theoretical model is very good and shows that the experiment is performed at the SQL (red continuous curves). Furthermore, the data are consistent with the prediction of an optimal, i.e. minimum variance, region of atomic density around the tested value of $n = 7.65 \times 10^{12}$ cm^{-3}, indicated by vertical continuous lines in Fig. (5.1). We also found that the optimal interval is narrower for the variance of the linewidth (bottom) with respect to that one of the Larmor frequency (top) as expected from the theory and depicted in Fig. (5.1). We point out that predicting a minimum variance in a parameter, estimated by fitting noise spectra, corresponds to the potential *a priori* optimization of state-of-the-art measurements based on noise spectroscopies, not only in atomic [26, 27, 47] and solid state physics [108, 109, 25, 111], but also in other fields of science like, among the others, cell biology [130, 131], geophysics [132] and quantum information processing [133, 134, 135]. In the insets of Fig. (5.3) we report also good agreement between the $\Gamma_{11}^{\mathrm{exp}}$(n) (top) and $\Gamma_{33}^{\mathrm{exp}}$(n) (bottom) terms of the sample covariance matrix and the theoretical SQL. Differently from $\Delta\nu$ and ν_L, the variances of the estimated atomic and photon shot noise contributions increase versus atomic

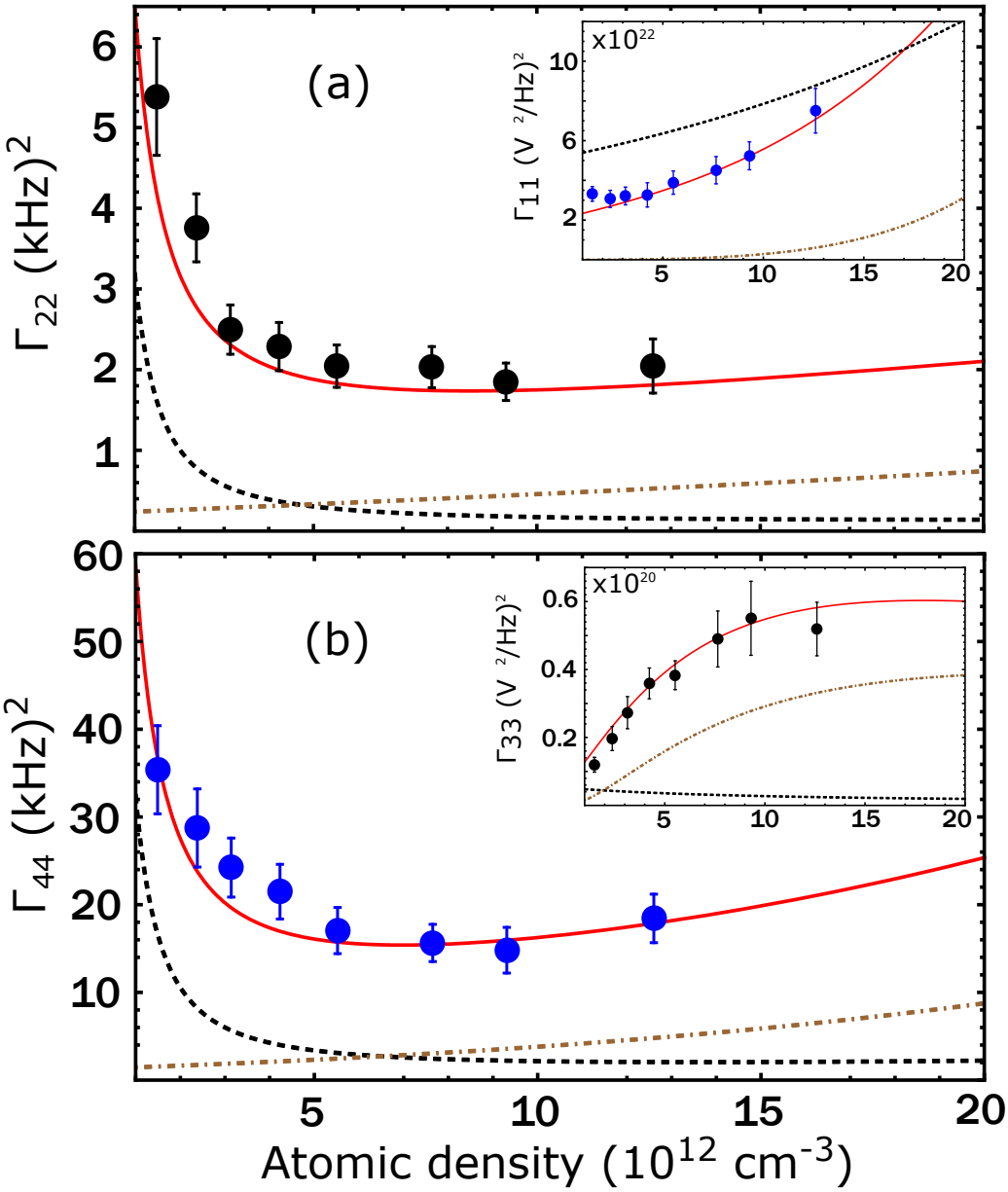

Figure 5.3: **Experimental sample variances.** **(a)** Experimental covariance matrix term $\Gamma_{22}^{\mathrm{exp}}(n)$ (black filled circles). **Inset (a)** Experimental covariance matrix term $\Gamma_{11}^{\mathrm{exp}}(n)$ (blue filled circles). **(b)** Experimental covariance matrix term $\Gamma_{44}^{\mathrm{exp}}(n)$ (blue filled circles) versus atomic density. **Inset (b)** Experimental covariance matrix term $\Gamma_{33}^{\mathrm{exp}}(n)$ (black filled circles). The continuous red lines represent the theoretical bound to the variances (SQL). The fixed optical power for both data and theory is $P = 2$ mW. The dashed and dot-dashed curves show optical-noise-only and atomic spin-noise-only scenarios, respectively. Error bars show the standard errors of the sample covariance term, calculated by applying the k-statistics [129] to the individual parameter distribution (see text).

density over all he investigated range, in agreement with theoretical predictions.

As described in the theoretical section (5.1.1), the standard deviation of the noise spectrum is equal to the fit function $\sigma(\nu) = f(\nu) = \sigma_{\rm ph} + \sigma_{at}(\nu)$ of Eq. (5.15), where $\sigma_{\rm ph} = S_{\rm ph}$ and $\sigma_{at}(\nu) = S_{at}\frac{(\frac{\gamma}{2})^2}{(\nu-\nu_L)^2+(\frac{\gamma}{2})^2}$, and it is crucial in determining the SQL by entering, to the second power, into the denominator of the integrals in Eq. (5.12), while the partial derivatives in the numerator are independent of $S_{\rm ph}$, as shown in Eqs. (5.16-5.19). In all the plots of Fig. (5.3) we show two functions (black dashed and brown dot-dashed) that are obtained by calculating Eq. (5.11) when either the uncertainty $\sigma(\nu) = \sigma_{\rm ph}$ or $\sigma(\nu) = \sigma_{\rm at}(\nu)$ is inserted into the denominator of Eq. (5.12), respectively. The resulting functions show qualitatively that the SQL of optically-detected noise spectroscopy arises from both quantum fluctuations of the probe photons (shot-noise) and intrinsic fluctuations of the investigated system, resonant spin-noise in the specific case. Then, we claim that the increasing of the variances after the optimal region, in the high-density shown in Figs. (5.1) and (5.3), is due to the increased atomic noise contribution to the spectrum uncertainty together with additional linewidth broadening due to atomic collisions [72].

5.5 Improvement by squeezing

A further confirmation of the quantum limitations to the covariance matrix, is that the use of a polarization squeezed probe allows us to perform an estimation beyond the SQL. In Fig. (5.4) we report, as a function of optical power, the variance of the diagonal covariance terms $\Gamma_{44}(\rm P)$ and $\Gamma_{22}(\rm P)$ for a coherent and for a polarization squeezed probe with 2.6 dB ($\xi^2 = 0.55$) of squeezing, at the optimal

atomic density $n = 7.65 \times 10^{12}$ cm^{-3}, as we demonstrated in Fig. (5.3). The improvement in signal-to-noise ratio, due to the quantum shot-noise suppression [72], turns into a reduction of the variance of both the resonance linewidth and Larmor frequency below the SQL. The theoretical model agrees very well with data, acquired up to a power of 4 mW, both for coherent and squeezed probing. The theory also predict squeezing to reduce the variance even for optical power much above the optimal range, as illustrated in (5.4). In the high-power regime, both curves increase because of both the larger contribution to the SQL from the atomic spin noise, which has a quadratic dependence on optical power, as for Eq. (4.6) and additional power broadening of the linewidth [72]. If we just look at the

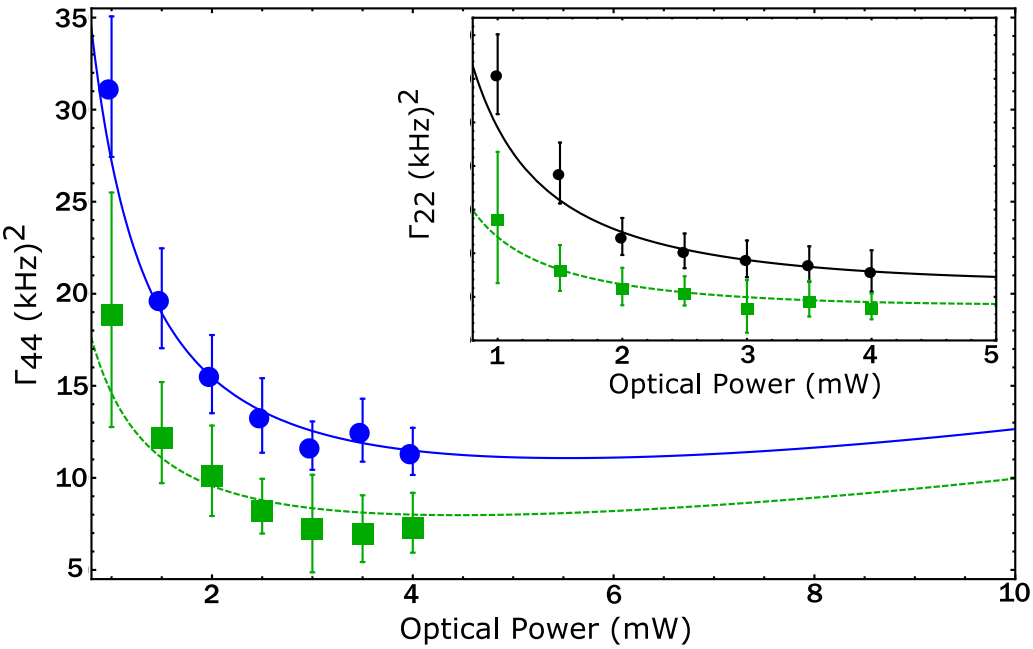

Figure 5.4: **Improvement by squeezing**. Covariance term $\Gamma_{44}^{\exp}(\mathrm{P})$ versus power for coherent (blue circles) and polarization squeezed (green squares) probe, respectively. The theoretical SQL for $\xi^2 = 1$ (coherent probe) and $\xi^2 = 0.55$ (squeezed probe) is shown with continuous and dashed curves, respectively. **Inset** Analogue analysis for the covariance term $\Gamma_{22}^{\exp}(\mathrm{P})$. The fixed atomic density is $n = 7.65 \times 10^{12}$ cm^{-3}. Error bars show the standard errors of the sample covariance term, calculated by applying the k-statistics [129] to the individual parameter distribution (see text).

coherent data, we see that, by increasing the optical probe power, the variance of both variables end up into the optimal area shown in the 2D plots of Fig. (5.1). On the top of that, at same optical power, squeezing reduces both variances under all the investigated parameter range.

5.6 Conclusions

We have presented a novel theoretical model on quantum limits of noise spectroscopy, by deriving a SQL for the covariance matrix of the fit parameters, in the presence of optical probing. We tested the model against data from spin noise spectroscopy of hot Rb vapor and we demonstrated operation at the SQL, in good agreement with theory. The model provides an elegant and simple way to identify optimal experimental conditions that minimize the variance of parameters of interest in noise spectroscopies in different fields like cell biology [130, 131], molecular biophysics [136, 127], geophysics [132], space science [137], and quantum information processing [138, 139, 133, 134, 135]. Our model can be applied to optimize a broad range of SNS applications like measurements of spin lifetime, g-factors and isotope abundances both in atomic and solid state physics. We also identify the quantum nature of the contributions to the SQL and we experimentally demonstrate the overcoming of such limitations by optical squeezing of the probe beam.

Chapter 6

Shot-noise-limited optical magnetometer with sub-picotesla sensitivity at room temperature

In this chapter we report a photon shot-noise-limited (SNL) optical magnetometer based on amplitude modulated optical rotation (AMOR) using a room-temperature ^{85}Rb vapor in a cell with anti-relaxation coating. The instrument achieves a room-temperature sensitivity of 70 fT/$\sqrt{\text{Hz}}$ at a DC field of $B = 7.6$ μT. Experimental scaling of noise with optical power, in agreement with theoretical predictions, confirms the SNL behaviour from 5 μT to 75 μT. While no quantum resources of light were used in this setup, the combination of best-in-class sensitivity and SNL operation makes the system a promising candidate for application of squeezed light

to a state-of-the-art atomic magnetometer. The described experiment has been carried out at the Institute of Physics of the Jagiellonian University (Krakow) in collaboration with the group of Prof. Wojciech Gawlik and it has been published in [84].

6.1 Introduction

Optical magnetometers [80, 7, 89] are currently the most sensitive devices for measuring low-frequency magnetic fields and have many applications, from medical diagnostics and biomagnetism [11, 12, 13], to the detection of fields in space [17, 18], to tests of fundamental physics [19, 20, 21]. Quantum-enhanced sensitivity of optical magnetometers has been recently demonstrated using squeezing [46, 40, 43]. Quantum enhancement of a best-in-class magnetometer, i.e. of an instrument with unsurpassed sensitivity for a given parameter range, is a natural next step after these proof-of-principle demonstrations. This kind of enhancement was recently shown in gravitational wave detection, when the LIGO H1 detector was enhanced with squeezed light [41].

In this chapter we demonstrate a shot-noise-limited magnetometer that simultaneously is well-adapted for sensitivity enhancement with squeezed light, as in [40, 43], and has detection noise of 70 fT/$\sqrt{\text{Hz}}$ at a field of 7.6 μT. For the given field strength and room-temperature atomic density of $n = 1.27 \times 10^{10}$ atoms/cm^3 [140], this is among the best reported magnetometer sensitivity including those using amplitude [85, 95], frequency [141, 142] and polarization [143] modulation strategies. With two orders of magnitudes higher atomic density, a heated-cell scalar magnetometer (cell temperature 160° C) showed a noise level below 10 fT/$\sqrt{\text{Hz}}$ in the same field range [144]. Sub-femtotesla spin-exchange-relaxation-

free (SERF) magnetometers, e.g. [8, 10], are not comparable here because they operate only at near-zero field.

After introducing the magnetometer mode of operation, we describe the experimental setup, we define the magnetometer sensitivity and we report its experimental optimization. In the last section we make a detailed and redundant analysis of the quantum versus classical noise contributions, including both theoretical calculation of the expected shot noise level and an independent, fully experimental analysis based on scaling of measured noise with optical power. These agree and indicate the potential to improve the sensitivity of this system by up to 6 dB using polarization squeezing.

6.2 Amplitude modulated optical rotation (AMOR) magnetometry

Our magnetometer is based on the process of nonlinear magneto-optical rotation (NMOR), also known as nonlinear Faraday rotation [5, 80]. In this process, already introduced in chapter (2), resonant or near-resonant light produces spin coherence by optical pumping, and the spin coherence in turn produces Faraday rotation, either of the optical pumping beam itself [79], or of a separate probe beam [85], leading to a detectable signal indicating the Larmor frequency and thus the magnitude of the field. Modulation of the pumping, either in frequency (FM NMOR) [6], amplitude (AMOR) [79] or circular polarization [143] produces a resonant buildup of atomic polarization with minimal disturbance to the spin coherence. The modulation strategy significantly increases the magnetic dynamic range, i.e., the ratio between the largest detectable signal, which in

NMOR can reach the geophysical field range [141, 86], and the lowest detectable signal. NMOR can give high sensitivity, due to the long ground-state coherence times, and hence narrow resonances, that arise when alkali vapours are confined with a buffer gas [76, 77] or in anti-relaxation coated cells [75, 78].

As previously introduced in chapter (2), the sensitivity of optical magnetometers is ultimately limited by two fundamental noise sources: the atomic projection noise and the optical shot-noise [80, 7]. When atomic projection noise is limiting, quantum non-demolition measurement [93, 145, 46, 146], atomic entanglement [92] and spin squeezing [94] can improve sensitivity for measurements within the atomic coherence time [46] and for non-exponential relaxation processes [147]. Similarly, optical squeezing can improve sensitivity when photonic shot noise is limiting [40, 43]. Prior works on AMOR [95] and FM NMOR [142] have shown experimental sensitivity about one order of magnitude above (i.e. worse than) the predicted fundamental sensitivity. Other magnetometers based on oscillating field-driven Zeeman resonance [144], M_x method [148] or intensity-modulated (IM) pumping [149], have approached the photon shot-noise level, but still have a significant technical noise component. In contrast, we report an AMOR magnetometer in which all other noise sources are significantly below shot noise from 5 μT to 75 μT, as needed for squeezed-light enhancement.

6.3 Experimental setup

The experimental scheme is shown in Fig. 6.1. A sample of isotopically-pure ^{85}Rb is contained in a spherical vapor cell of 10 cm diameter, with no buffer gas. The cell is at room temperature ($\sim 25°$C) corresponding to ^{85}Rb atomic density of $n = 1.27 \times 10^{10}$ atoms/cm^3 [140]. The inner cell walls are coated with

an antirelaxation (paraffin) layer that prevents atoms from depolarizing upon collision with the walls and prolongs the ground-state Zeeman coherence lifetime to $\simeq 100$ ms.

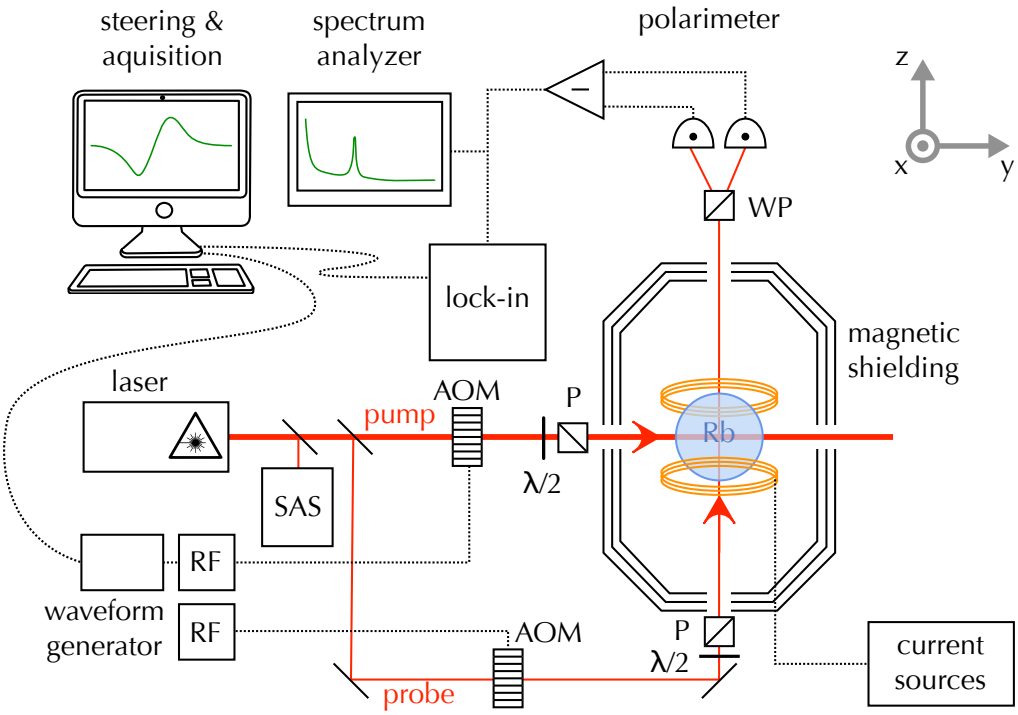

Figure 6.1: **Experimental Setup**. SAS – saturated-absorption-spectroscopy frequency reference, AOM – acousto-optical modulator with the RF driver, $\lambda/2$ – half-wave plate, P – polarizer, WP – Wollaston prism. The oscillator that drives the AOM of the pump beam is amplitude modulated with a sine-wave of frequency $\Omega_m/2\pi$ by the waveform generator.

The cell is inside a "box solenoid," a cubical box made of printed-circuit-board material, with three mutually perpendicular sets of printed wires, each in a solenoidal pattern. Together with an accompanying ferrite box, which extends the effective length of the solenoid based on the method of images for magneto-statics, we can generate a uniform field along the three directions. In this experiment we generate a constant magnetic field along the z-axis, which is also the probe beam

direction, while the coils in the perpendicular directions are used to compensate the residual transverse magnetic field. Residual magnetic field gradients are compensated by a set of three mutually perpendicular anti-Helmoltz coils wound around the box. This setup was kept inside three nested layers of μ-metal shields, giving a whole magnetic shielding of $\sim 10^6$ efficiency.

The light source for both probing and pumping is an extended-cavity diode laser whose frequency is stabilized by saturated absorption spectroscopy at 20 MHz below the $F = 3 \rightarrow F' = 2$ transition of the ^{85}Rb D_1 line. The laser beam is split into pump and probe beams that pass through acousto-optic modulators independently driven by two 80 MHz RF signals so that, before reaching the atoms, the frequency is additionally red-detuned 80 MHz away from the $F = 3 \rightarrow F' = 2$ transition. Additionally, the intensity of the pump beam is sinusoidally modulated with frequency $\Omega_m/2\pi$. [1] Both pump and probe have a beam diameter of 1mm at the center of the vapor cell.

Both beams are vertically polarized (x-direction in Fig. 6.1) with high-quality crystal polarizers to ensure pure linear polarization and the light intensity that interacts with the atoms can be adjusted with half-wave plates situated in front of the polarizers. The pump beam passes through the cell in the y direction, perpendicular to the z-axis bias field. When the pumping modulation frequency coincides with twice the Larmor precession frequency, a large precessing alignment accumulates in the $x-y$ plane. The pump power is set to 60μW. The probe beam propagates through the atomic vapor cell along the z-axis, i.e. parallel to the field, and experiences Faraday rotation (NMOR) of the polarization plane due to the

[1] The AOM along the probe beam path makes the setup suitable also for single-beam NMOR but is not necessary in the strategy followed in this paper, where just the pump beam needs to be amplitude modulated.

precessing alignment. The optimal probe power changes from 80.5 μW to 620 μW, depending on the employed detector's gain.

Polarization rotation is detected with a balanced polarimeter consisting of a Wollaston prism set at an angle of 45° with respect to the vertical and a fiber-coupled variable gain balanced photo-detector (PDB) (Thorlabs PDB150A DC). The differential output is analyzed with a radio-frequency (RF) spectrum analyzer (SA) (RIGOL DSA1030A) or demodulated at $\Omega_m/2\pi$ with a lock-in amplifier (Stanford Research Systems model SR844). The in-phase and quadrature output signals are then stored on a computer for later analysis. As explained in section (6.5), both SA and lock-in signals are used to determine the magnetometer sensitivity. Throughout this work we used SA resolution bandwidth RBW= 30 Hz and video bandwidth VBW= 30 Hz.

6.4 AMOR signal and magnetic sensitivity

As anticipated in chapter (2.4) the AMOR signal is generated by means of amplitude modulated pumping and unmodulated CW probing in a right-angle geometry. Optical pumping with linearly polarized light generates spin alignment, i.e. ground state coherences between Zeeman sub-levels with $\Delta m_F = 2$ [81, 82]. The alignment describes a preferred axis, but not a preferred direction along this axis. The signal due to alignment oscillates at twice the Larmor frequency due to this additional symmetry, i.e., at $2\Omega_L = 2g_F\mu_0 B/\hbar$ where g_F is the Landé factor and μ_0 is the Bohr magneton. Amplitude modulated optical pumping at $2\Omega_L$ produces a resonant build-up of spin alignment, as demonstrated in several earlier works [85, 86]. The alignment behaves as a damped driven oscillator, and

in steady state responds at frequency Ω_m with an amplitude and phase relative to the drive that depend on the detuning $\Omega_m - 2\Omega_L$ [87]. As described in chapter (6), the weak probe is sensitive to alignment through linear dichroism, i.e., linearly polarized light parallel to the alignment experiences less absorption [89]. When the alignment is neither parallel to nor perpendicular to the probe polarization, this dichroism rotates the probe polarization. This rotation signal also oscillates at $2\Omega_L$, and we demodulate it with the lock-in amplifier to extract the in-phase and quadrature components, shown in Fig. 6.2 for a representative magnetic field intensity of $B = 10.8$ μT.

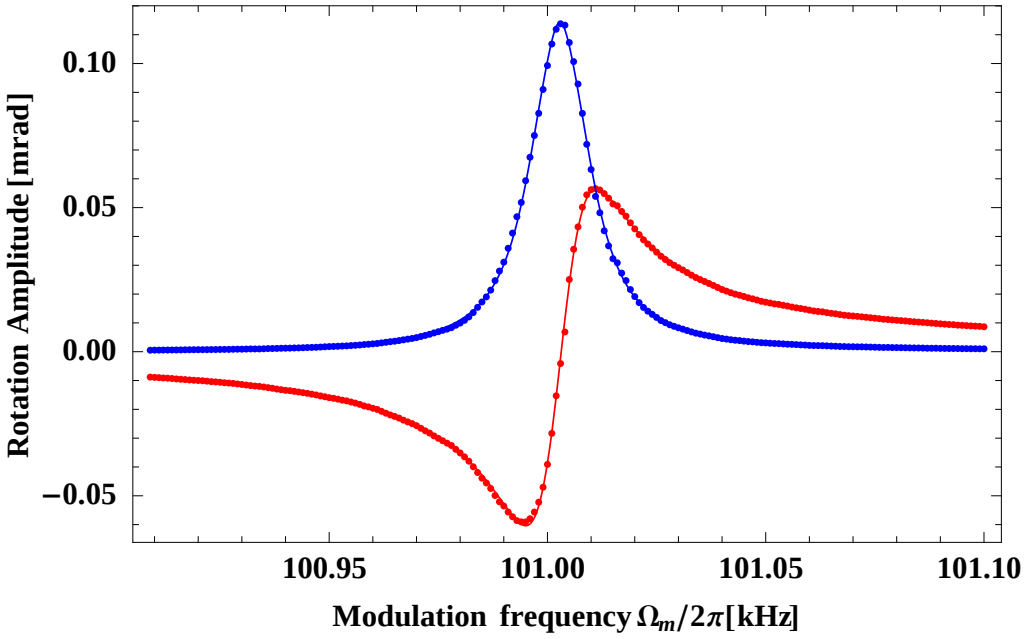

Figure 6.2: **AMOR Signals versus Modulation Frequency**. In-Phase ϕ_{P} (blue) and quadrature ϕ_{Q} (red) output signals of the lock-in amplifier for $B = 10.8\mu$T, $P_{probe} = 80\mu$W and $P_{pump} = 60\mu$W. The modulation/demodulation frequency $\Omega_m/2\pi$ is scanned around the resonance condition $\Omega_m = 2\Omega_L(\Delta = 0)$. Experimental data are fitted by dispersive (red) and absorptive (blue) Lorentzian curves. From the fit we obtain resonance frequency and FWHM width $\gamma = \Gamma/2\pi$.

The optical rotation angle is an oscillating function at the modulation fre-

quency Ω_m with the amplitude dependence well described by a single-Lorentzian in the small field approximation

$$\begin{aligned}\phi(t) &= \phi_0 \mathrm{Re}\left[\frac{i\Gamma/2}{\Delta + i\Gamma/2} e^{i\Omega_m t}\right] + \delta\phi(t) \\ &= \phi_\mathrm{P} \cos(\Omega_m t) + \phi_\mathrm{Q} \sin(\Omega_m t) + \delta\phi(t) \end{aligned} \tag{6.1}$$

where ϕ_0 is the maximum rotation angle, which depends on the optical detuning, cell dimension, and pump power. The detuning between the modulation frequency and $2\Omega_L$ is $\Delta \equiv \Omega_m - 2\Omega_L$ while Γ is the FWHM line width due to relaxation, pumping, and nonlinear Zeeman shifts [2]. The symbols ϕ_P and ϕ_Q are the in-phase and quadrature components, respectively, directly observable by demodulation at Ω_m. The photon shot noise contribution, $\delta\phi(t)$, is a white noise with a power spectral density $S_\phi(\omega) = 1/(2\Phi_\mathrm{ph})$ [142, 95, 89], where Φ_ph is the flux of photons arriving to the detector.

We note that on resonance, i.e. with $\Delta = 0$, the signal consists of a cosine wave at frequency Ω_m with amplitude ϕ_0, plus a white-noise background due to $\delta\phi(t)$. In the balanced condition, and with $\phi_0 \ll \pi$, the polarimeter signal is $\propto \phi(t)$. When recorded on a spectrum analyzer with resolution bandwidth RBW, the signal shows a peak power spectral density $S_\mathrm{sig} = g_\mathrm{det}^2 \phi_0^2/(2\mathrm{RBW})$, where g_det is the gain relating rotation angle to RF amplitude at the SA (the factor of one half represents a mean value of $\langle\cos^2\rangle = 1/2$). A typical RF spectrum of the AMOR resonance recorded in our measurements is shown in Figure 6.3. The signal peak rises above a flat background $S_\mathrm{bg} = g_\mathrm{det}^2 \overline{\delta\phi}^2/2$, where $\overline{\delta\phi}^2 = S_\phi$ is

[2] The single-Lorentzian approximation should fail at large B, when the resonance splits into several lines due to the nonlinear Zeeman shift. This was not observed at the field strengths used in this work. Even at 75μT, the response was well approximated as a single Lorentzian. This suggests a strong line-broadening accompanied the nonlinear Zeeman shift.

the spectral noise density of the phase, so that $\overline{\delta\phi}$ has units rad/$\sqrt{\text{Hz}}$ (the factor of two reflects the fact that only one quadrature contributes to the noise of the demodulated signal, while both are recorded by the SA). The signal-to-noise ratio SNR is given by $\text{SNR}^2 \equiv \text{RBW} S_{\text{sig}}/S_{\text{bg}} = \phi_0^2/\overline{\delta\phi}^2$, which is independent of g_{det} and RBW and can be directly measured.

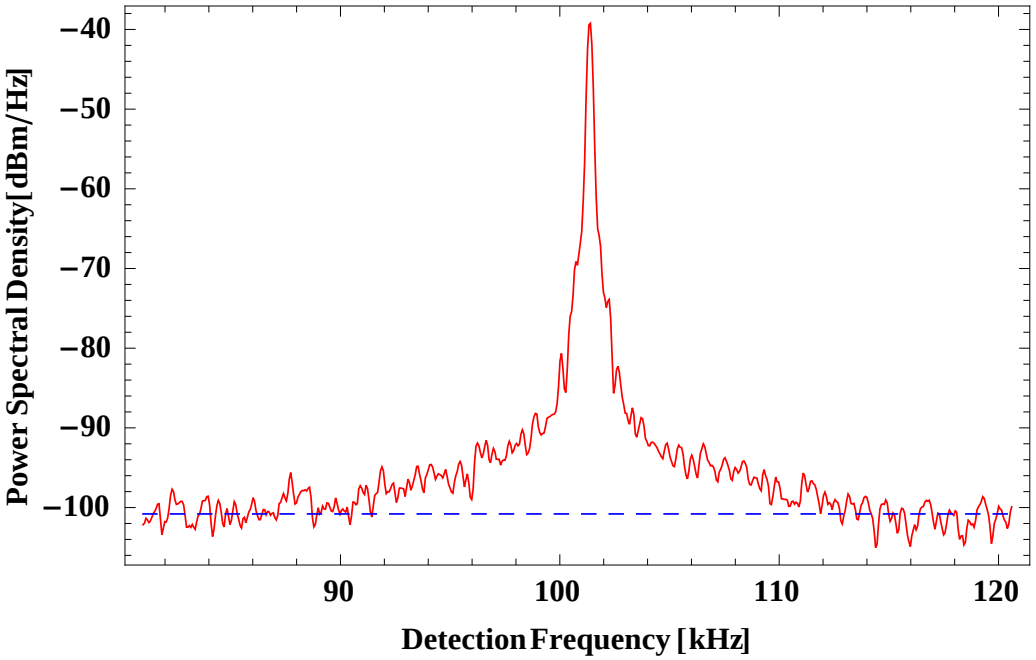

Figure 6.3: **AMOR Magnetometer Resonance Spectrum**. Spectrum of the rotation signal acquired on SA at the resonance condition $\Omega_m = 2\Omega_L$ with RBW= 30Hz, VBW= 30Hz and a PDB nominal gain G= 10^6V/A. The red curve shows the signal spectrum $S(\Omega) \equiv S_{\text{sig}}$ with a magnetic field of $B = 10.8\mu$T and 40kHz span frequency around Ω_m, while the blue dashed line indicates the background noise level, i.e. $S(\Omega) \equiv S_{\text{bg}}$ acquired with $B = 0$ and averaged over a 4kHz range around Ω_m.

The magnetic sensitivity can be related to SNR by noting that the slope of the quadrature component on resonance is

$$\frac{d\phi_{\text{Q}}}{dB} = \frac{g_F \mu_0}{\pi\hbar}\frac{\phi_0}{\gamma}. \tag{6.2}$$

where the width $\gamma \equiv \Gamma/2\pi$ has unit of Hz. Considering that on resonance $\Omega_m = 2\Omega_L = 2g_F\mu_0 B/\hbar$, we find the noise in magnetic units, i.e., the sensitivity

$$\delta B = \left|\frac{d\phi_{\rm Q}}{dB}\right|^{-1} \overline{\delta\phi} = \frac{\pi\hbar}{g_F\mu_0}\frac{\gamma}{\rm SNR}, \tag{6.3}$$

with units $\mathrm{T}/\sqrt{\mathrm{Hz}}$.

As described in the next section, using this method to measure the sensitivity we find δB as low as 70 $\mathrm{fT}/\sqrt{\mathrm{Hz}}$. For comparison, the atomic projection noise contribution to the overall measurement is: [80, 7]:

$$\delta B_{at} \simeq \frac{\hbar\pi}{g_F\mu_0}\sqrt{\frac{\gamma}{N_{\rm at}\Delta\tau}} \tag{6.4}$$

where N_{at} is the number of atoms involved in the measurement. With our cell volume of $4\pi R^3/3$, $R \approx 5$ cm, atomic density $n = 1.27\times10^{10}$ atoms/cm^3, measured relaxation rate $\gamma \approx 10$ Hz and $\Delta\tau = 1$s time of measurement we find $\delta B_{at} \simeq 0.134$ $\mathrm{fT}/\sqrt{\mathrm{Hz}}$. This value is two orders of magnitude lower than the observed sensitivity, justifying our earlier step of ignoring this contribution. If all other noise sources have lower amplitude than the shot noise, then the magnetometer can be expected to be photon shot-noise-limited. In Section 6.6 we demonstrate that, in the experimental conditions that optimize the sensitivity, this is indeed the case.

6.5 Optimization of the magnetometer sensitivity

In this section we examine different setup parameters in order to find the optimal conditions maximising the magnetometric sensitivity.

In our configuration, with a pump and probe of the same frequency, laser tuning affects the pumping efficiency, the rotation signal corresponding to a given degree of atomic alignment, and the probe absorption. In addition, the pump power increases both the amplitude and the width of the rotation signal. To optimize these parameters, we first adjust the gradient fields to minimize the broadening due to magnetic field inhomogeneities [150], and then optimize the laser frequency and pump power to maximize the slope of the AMOR signal. The optimum conditions, which we use throughout this work, occur at the detuning of 100 MHz to the red of the $F = 3 \rightarrow F' = 2$ transition and 60 μW of pump power.

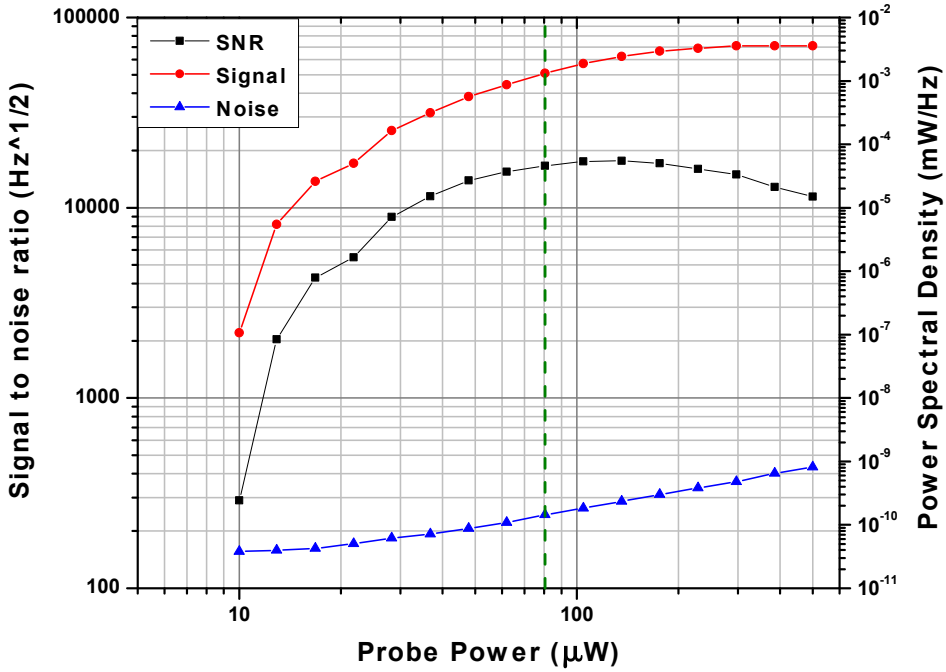

Figure 6.4: **Magnetometer SNR**. Signal-to-Noise ratio versus optical probe power. The modulation frequency was 71 kHz ($B = 7.6$ μT). The green dashed line indicates the probe power value of 80.5 μW that maximizes the sensitivity. This condition does not correspond to the best SNR because of the trade-off with the width trend (see Eq. 6.3).

To measure the magnetometric sensitivity for a given probe power and field strength, we first set the detuning and pump power to the optimal values discussed above. We then set a constant current in the solenoidal coil along the z-axis, and minimize the width of the AMOR resonance with the help of the gradient coils. Demodulation of the signal yields the in-phase and quadrature components of the resonance versus Ω_m, as depicted in Fig. 6.2. By fitting a Lorentzian to these curves, the central resonance modulation frequency $\Omega_m = 2\Omega_L$ ($\Delta = 0$) and width γ are obtained. Keeping then Ω_m fixed and maximizing the in-phase component allows one to measure the spectrum as in Fig. 6.3 and to extract $S_{\rm sig}(\Omega_m) = \phi_0^2/\mathrm{RBW}$. A second spectrum is taken with the B-field set near zero. This moves the resonance peak far away from Ω_m, so that $S(\Omega_m)$ now gives the background noise $\delta\phi^2_{RMS}$. In analogy with previous works [95, 151] the experimental sensitivity, defined by equation 6.3, can be calculated in terms of the width (FWHM) and signal-to-noise ratio. The magnetometric sensitivity of the instrument was measured in the range from 5 μT to 75 μT. We employ two detector bandwidths, 300 kHz and 5 MHz, corresponding respectively to nominal transimpedance gains of 10^6 V/A and 10^5 V/A.

Typical results, taken at a field of 7.6 μT (modulation frequency of 71 kHz, detector gain setting 10^6 V/A) are shown in Figs. 6.4 and 6.5. In Fig. 6.4 we present signal $S_{\rm sig}$ and noise $S_{\rm bg}$ power spectral densities with the resulting signal-to-noise ratio (SNR) as a function of the probe power. Signal grows with the probe power until saturation occurs. In contrast, noise grows monotonically, so that the SNR has an optimal value before the signal saturates. Fig. 6.5 depicts the slope ϕ_0/γ and the sensitivity δB, calculated using equation 6.3, as a function of probe power, also acquired with $B = 7.6$ μT. An optimum sensitivity of 70

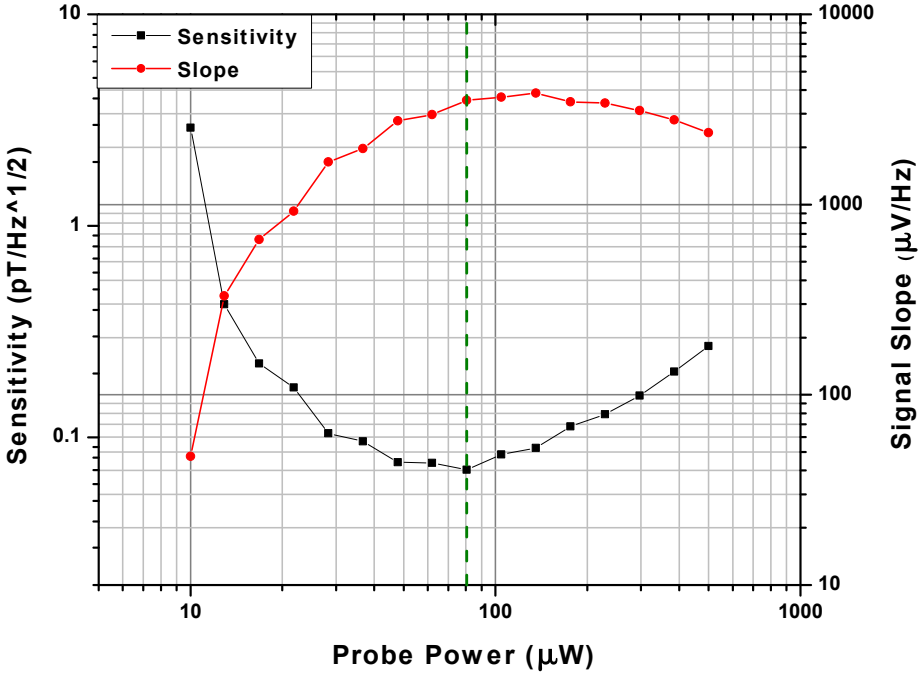

Figure 6.5: **Magnetometer Sensitivity**. Signal slope ϕ_0/γ and magnetometer sensitivity versus optical probe power. The sensitivity is computed as in Eq. 6.3 using the width from the demodulated signal, as in Fig. 6.2, and the measured SNR, as in Fig. 6.3. The green dashed line indicates the probe power that gives the best sensitivity of 70 fT/$\sqrt{\text{Hz}}$ for a modulation frequency of 71 kHz ($B = 7.6$ μT)

.

fT/$\sqrt{\text{Hz}}$ is observed at a probe power of 80.5 μW [3] and remains within 10% of this value between 50 μW and 100 μW [4].

[3] Although this probe power exceeded the pump power of 60 μW, the increased resonance broadening is compensated by higher signal amplitude and results in a better net sensitivity. Moreover, for the gain setting of 10^5 V/A we find the optimal probe power to be as high as 620μW.

[4] While optimized sensitivity value of 70 fT/$\sqrt{\text{Hz}}$ is observed below 10.8 μT at higher fields this number rises significantly, roughly as B^4, reaching 250 pT/$\sqrt{\text{Hz}}$ at 75 μT ($\Omega_m = 700$ kHz). The observed reduction of the sensitivity for larger fields is related to the nonlinear Zeeman effect (NLZ) [89, 141, 86]. Saturation of the ferrite shielding cube at high fields and high-order magnetic field gradients that are not compensated in the current experimental setup could also contribute to the sensitivity worsening and need further investigation.

6.6 Quantum noise analysis

Here we report the results of two noise analyses: the first characterises the probing and detection system, without an atomic contribution. This was performed by probing at the optimal laser detuning but with the pump beam off. The second analysis characterizes the magnetometer under the experimental conditions that optimize the sensitivity, as described in section (6.5).

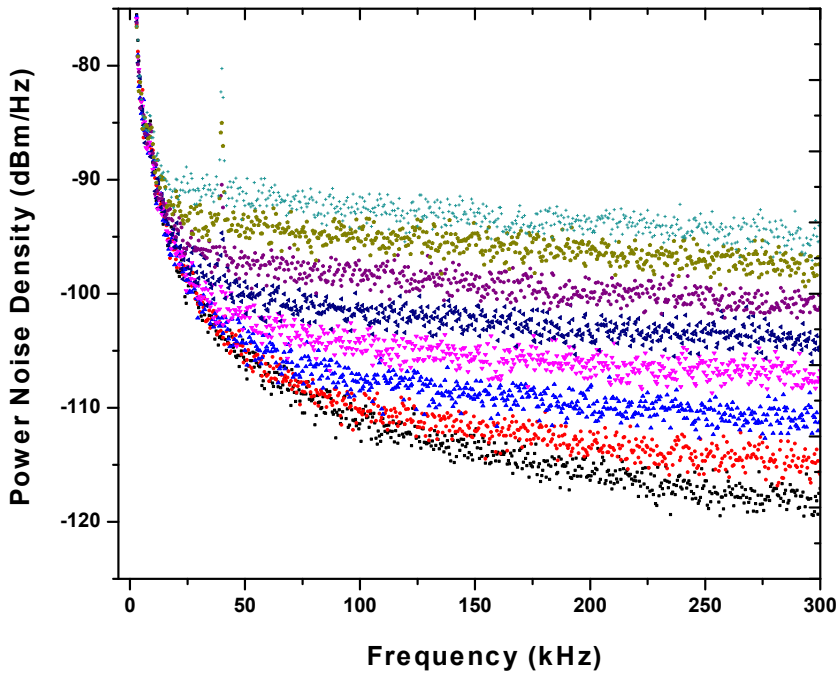

Figure 6.6: **Low-Frequency Detection Noise**. Noise spectra of the PDB differential output acquired with mean optical power of $P = 0, 10, 20, 50, 100, 200, 400, 700\mu$W, from bottom to top. G= 10^6 V/A and BW= 300 kHz.

In a linear detection system, the noise power N of the electronic output will

depend on the average light power P as

$$N = AP^0 + BP^1 + CP^2, \tag{6.5}$$

where A, B and C are constants. The three terms of this polynomial are the "electronic noise" (stemming, e.g. from the detector electronics), the shot noise, and the "technical noise" contributions, respectively [52, 152]. The laser source can contribute to technical noise, e.g. through power fluctuations if the detection is imbalanced or if its optical elements are unstable. By determining the noise scaling as the function of light intensity, we can identify the dominating noise source. When $BP^1 > AP^0$ and $BP^1 > CP^2$, we say the system is shot-noise limited, in the sense that the shot noise is the largest noise contribution. These two inequalities define the range of powers $B/C > P > A/B$ in which the system is SNL. If $B/C < A/B$, the system is not SNL for any power. This definition of SNL can be extended to include more stringent conditions that might arise in applications. For any given $k \geq 1$, we can consider powers satisfying the inequalities $B/(kC) > P > (kA)/B$, i.e. powers such that the shot-noise contribution is a factor k larger than both the electronic noise and the technical noise contributions. For instance, for $k = 2$, the photonic noise is 3 dB higher than the other two contributions of Eq. (6.5).

For a given field B, and thus the Larmor precession or modulation frequency, the noise of interest is $N = S(\Omega_m)$, the noise spectral density at the demodulation frequency Ω_m. Using the SA we collect output noise spectra for several probe intensities. The data shown in Figs. 6.6 and 6.7 reveal the resulting scaling of the noise level. The electronic noise floor in the two Figures differs because of the different employed detector's gain. In the next step we examine the scaling of the

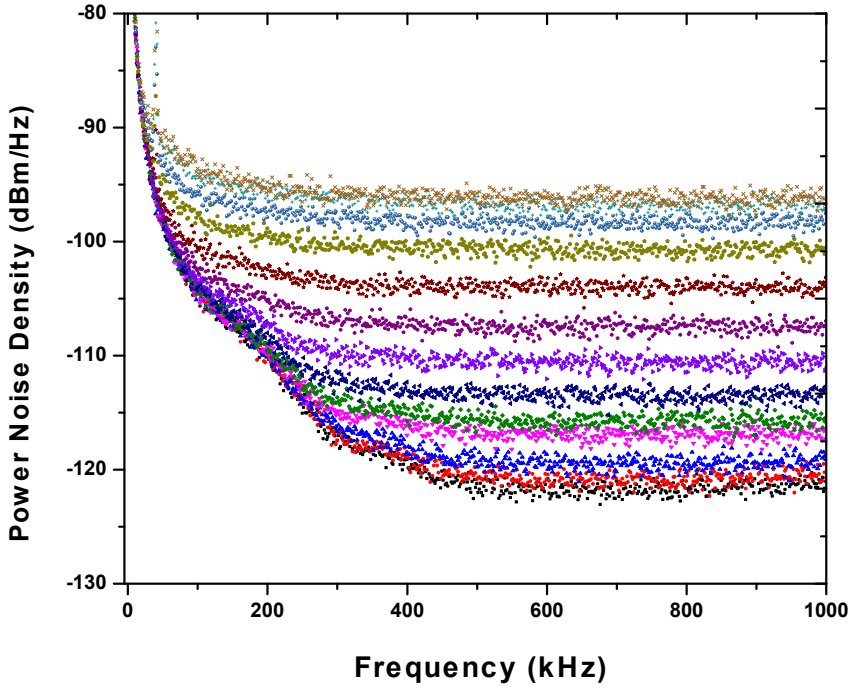

Figure 6.7: **High-Frequency Detection Noise**. Noise spectra of the PDB differential output acquired with mean optical power of $P = 0, 10, 20, 50, 70, 125, 250, 500, 1000, 2000, 3000, 4500\mu$W, from bottom to top. G= 10^5 V/A and BW= 5 MHz.

noise level.

For any given detection frequency Ω_m (that will be the modulation/demodulation frequency in the magnetometer operation mode), we can then fit the polynomial of Eq. (6.5), and find the range of powers and frequencies over which the detection system is SNL.

In Figure 6.8 we show an example of this analysis for a detection frequency of 48.5 kHz. We can see that scaling of the noise amplitude is different for different intensity ranges. The red area represents the SNL range. This is the

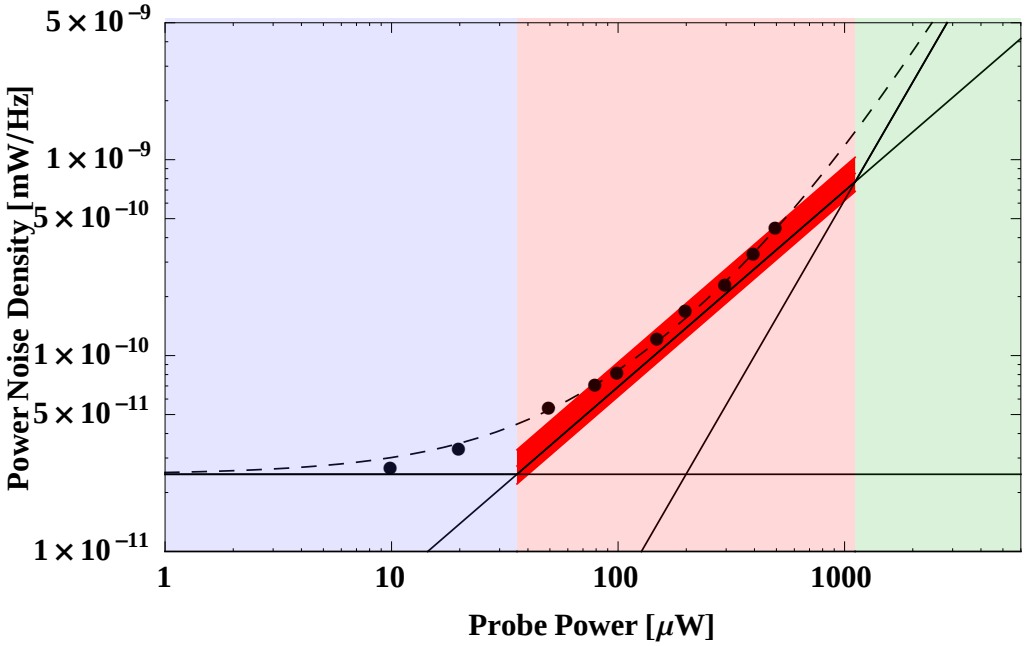

Figure 6.8: **SNL Power Range**. At 48.5 kHz detection frequency the coefficients of shot-noise (linear scaling) and technical noise (quadratic scaling) are obtained by fitting data (black points) with the polynomial function of Eq. 6.5 (dashed line), whose intercept is the electronic noise level (constant), measured at zero power. The red central area corresponds to the experimental SNL power range. We obtain good agreement with the theoretical shot-noise level (see text for calculation) represented by a red line with thickness due to the 10% uncertainty on the PDB nominal gain $G = 10^6$ V/A.

only power range in which quantum noise reduction via probe squeezing could significantly enhance the magnetometer sensitivity. We find good agreement between the observed shot noise level and the predicted value [52] (in W/Hz): $N(\bar{P}, \Omega) = G^2(\Omega) 2\bar{i}e/R$, where e is the electron charge, $R = 50$ Ohm is the SA input impedance and $G(\Omega)$ is detector gain at frequency Ω. Due to impedance matching at the detector, the PDB150A transimpedance gain is only half the nominal value when used with the SA. The frequency dependence can be neglected because our signal frequency of 48.5 kHz is far below the detector's 300 kHz nominal 3 dB bandwidth. We thus take $G(\Omega) = (10^6 \pm 10^5)/2$ V/A, which represents

the manufacturer's specification. The photocurrent is $\bar{i} = \bar{P}e/(h\nu\eta_{det})$ where $\bar{P}$ is the averaged optical power and $\eta_{det} = 0.88$ is the detector quantum efficiency.

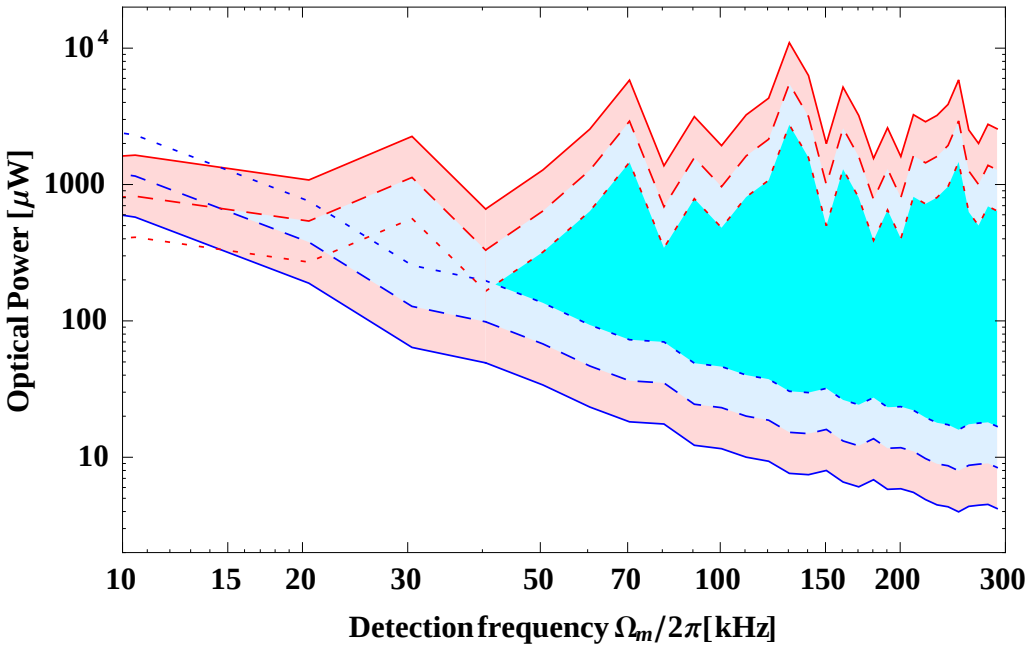

Figure 6.9: **SNL Power Range for low frequencies**. Blue and red curves show $(kA)/B$ and $B/(kC)$, the lower and upper limits, respectively, of the SNL range with $k = 1$ (red region), $k = 2$ (blue region) and $k = 4$ (cyan region). PDB gain $G = 10^6$ V/A. A/B and B/C were found by fitting the spectra of Fig. 6.6 as illustrated in Fig. 6.8. To reduce scatter, spectra were first averaged in 10 kHz bins. See text for details.

After performing the same analysis over all detection frequencies, we report in Figs. 6.9 and 6.10 lower (A/B) and upper (B/C) power limits of the SNL range (red area) versus frequency for two detector settings (10^6 V/A with 300 kHz BW and 10^5 V/A with 5 MHz BW). According to our previous definition we also show the signficant SNL regions with $k = 2$ (light blue area) and $k = 4$ (cyan area) that correspond to power regions where the photonic shot-noise is respectively 3 dB and 6 dB above the other noise contributions. Below 20 kHz the detection system is limited by electronic noise i.e. not significantly SNL within the investigated

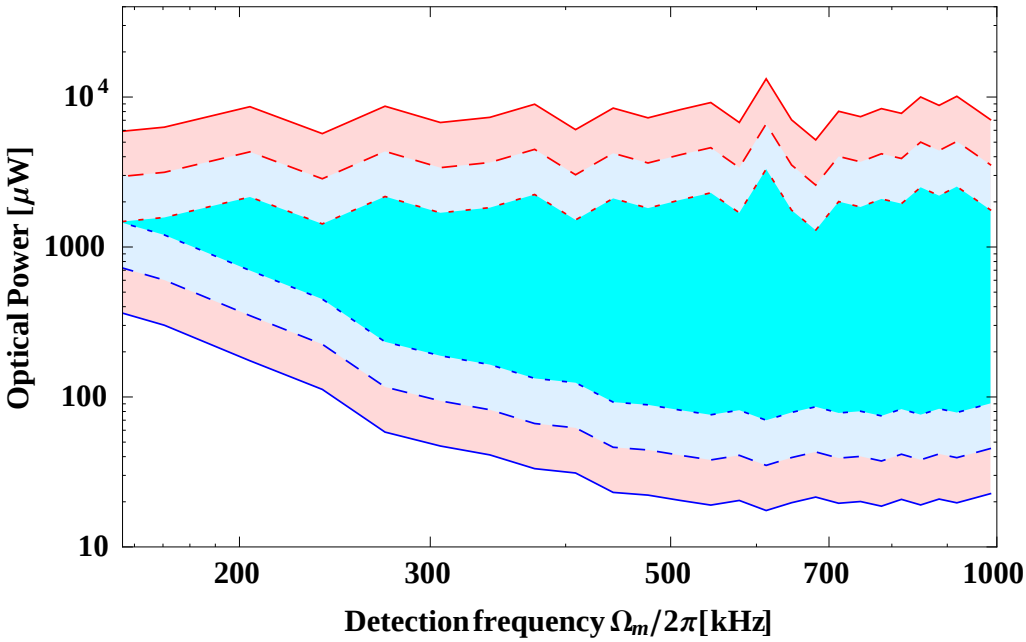

Figure 6.10: **SNL Power Range for high frequencies**. Blue and red curves show $(kA)/B$ and $B/(kC)$, the lower and upper limits, respectively, of the SNL range with $k = 1$ (red region), $k = 2$ (blue region) and $k = 4$ (cyan region). PDB gain $G = 10^5$ V/A. A/B and B/C were found by fitting the spectra of Fig. 6.7 as illustrated in Fig. 6.8. To reduce scatter, spectra were first averaged in 34 kHz bins. See text for details.

range of light power. It is properly reproduced in Fig. 6.9, although the data coming from the fit procedure suffer from considerable scattering. The dip in the red curves (B/kC) at 40 kHz is due to technical noise excess at this frequency (see Fig. 6.6).

6.7 Shot-noise limited performance and conclusions

Being interested in the SNL range, we have constrained our AMOR measurements, reported in section (6.5), to modulation/detection frequencies higher than 50kHz and thus to magnetic field intensities above 5 μT. Above modulation frequency of

200 kHz higher detector BW of 5 MHz needs to be used. Because of the lower gain (10^5 V/A), starting from frequency of 200 kHz the system becomes SNL above 200 μW as shown in Fig. 6.10.

Having determined the SNL range of the detector, we now proceed to characterize the magnetometer noise over this range. We set conditions for an optimized B-field measurement, as described in section (6.5), and switch off the B-field but leave on all other components, including the modulated pumping (in contrast to the measurements described above). We then acquire the noise power spectrum $S_{\mathrm{bg}}(\Omega_m)$ as a function of probe power. We report two representative results that correspond to detector setting with high gain and low gain respectively. Although in our experiment we did not observe any significant difference between the detector and the magnetometric noises, these two features may differ in other experimental conditions where environmental or technical noise sources dominate over the fundamental shot-noise contribution, as reported in previous works [95, 143].

In Fig. 6.11 we show the magnetometer noise power at 71 kHz (B = 7.6 μT) and 700 kHz (B = 75 μT) as a function of probe power. Fitting both data with $N(P)$ of Eq. (6.5) and knowing the electronic noise coefficient A, we find the coefficients B and C and we can define the shot-noise-limited power range. The difference in power range and reference level between the two representative frequencies is due to the different employed BPD gain. The trend of the noise power is linear, i.e. shot-noise-limited, in the power range of 30 μW-500 μW and 100 μW$-$1 mW for 71 kHz and 700 kHz respectively. Within this range the observed noise levels agree with theoretical shot-noise levels, calculated in the same way as for Fig. 6.8, by taking into account the 10% uncertainty on the detector nominal gain.

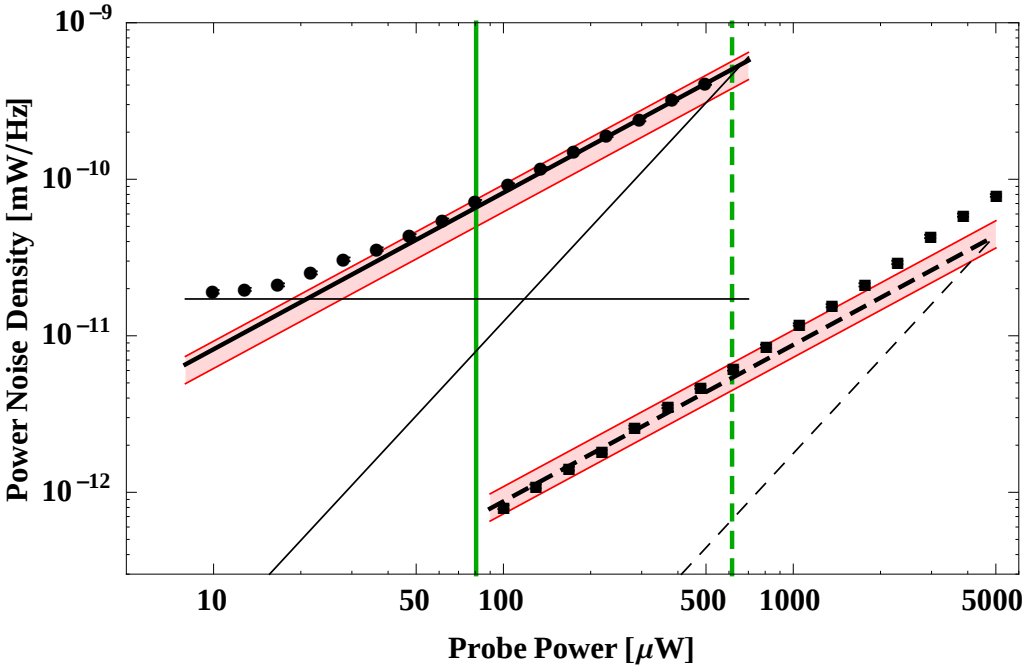

Figure 6.11: **SNL Magnetometer Performance**. Background noise level (acquired with $B = 0$ and averaged over a 4 kHz range around the resonance frequency) versus optical probe power at 71 kHz (black circles) and 700 kHz (black squares). These are simultaneously AM frequencies of the optical pumping (kept on in the noise measurement) and SA detection frequencies. Electronic (constant), shot-noise (linear) and technical noise (quadratic) contributions are shown with solid and dashed black lines at 71 kHz and 700 kHz respectively. For 700 kHz, the electronic noise level is below the shown scale at 5.6×10^{-14} mW/Hz. Red lines represent the theoretical shot-noise levels, calculated with the PDB nominal gain values of $G = 10^6 \pm 10^5$ V/A and $G = 10^5 \pm 10^4$ V/A respectively. The probe powers that maximize the magnetometer sensitivity (vertical green lines) fall within a significant SNL power range. See text for details.

Most importantly, the probe power intervals in which the magnetometer sensitivity is not worse than 10% of the maximum (reached at 80.5 μW and 620 μW respectively) are well inside a significant photon SNL region with $k = 4$, in which the photonic shot-noise is more than 6 dB above the electronic and technical noise levels. Within this optimal power range, significant sensitivity enhancement can be achieved by using optical polarization squeezing of the probe beam [40]. Indeed, the results of Fig. 6.11 show that the fundamental light shot-noise contri-

bution dominates the magnetometer noise budget i.e. technical noise and atomic projection noise (Eq. 6.4) are negligible when the magnetometer sensitivity is optimized at room temperature. Similar SNL performance was observed between 5μT and 75μT, over all the investigated magnetic dynamic range.

To conclude this chapter, we have demonstrated a sensitive pump-probe optical magnetometer that is shot-noise limited over the field range 5 μT to 75 μT. We optimized the system for pump/probe detuning, pump and probe beam powers, and found sensitivity of 70 fT/$\sqrt{\text{Hz}}$ at a field of 7.6 μT. The shot-noise-limited performance of the system has been confirmed by the scaling of the magnetometer noise as a function of probe input power and by agreement with the theoretical shot-noise level. This is the first experimental demonstration of a photon shot-noise-limited AMOR magnetometer. Moreover, it has the highest reported sensitivity for a room-temperature optical magnetometer in a range around 10 μT. Based on these observations, the described magnetometer is a good candidate for squeezed-light enhancement of sub-pT sensitivity over a broad dynamic range.

It is worth noting that AMOR and other modulated magnetometry strategies at these field strengths are well-matched to atom-resonant sources of squeezed light, because the signal is recovered at a multiple of the Larmor frequency, i.e. at a radio frequency. Although optical squeezing can be generated at low frequencies [153], in practice most squeezing experiments, and to date all atom-resonant squeezed light sources [67, 68, 69, 70, 71], have shown squeezing at radio frequencies.

A number of improvements suggest themselves. The lower limit of 5μT is set by the low-frequency electronic noise of the balanced detector. Electronics designed for lower frequency ranges [153] could make the system shot-noise-limited

also for weaker fields. Recently-developed anti-relaxation coatings [78] could extend the ground-state coherence. Techniques to evade broadening due to the nonlinear Zeeman effect could improve the sensitivity at high fields [154, 155, 156].

Chapter 7

Conclusion

7.1 Summary and outlook

This thesis describes the research activities of my PhD and contributes to the understanding and development of quantum-enhanced atomic sensors using squeezed states of light and magnetically-sensitive dense atomic vapors, at the state-of-the-art level of both technology and sensitivity.

First, we have described the design, construction and characterization of a new experimental apparatus for the study of atomic spectroscopy within a high-density regime ($n \geq 10^{12}$ cm^{-3}) and low-noise ($\simeq$ pT/$\sqrt{\text{Hz}}$) magnetic environment. The building of magnetic coils for the generation of both uniform fields in the three axes and gradient fields in the optical probe propagation direction, makes the described apparatus versatile for different applications in atomic metrology i.e. noise spectroscopy [66] and optical magnetometry [7]. Furthermore, by means of several technical efforts like the use of high optical transmission in all compo-

nents of the apparatus, shot-noise-limited detectors and high-stability locking systems, we have combined the new apparatus with an existing source of polarization squeezed light [69], which is based on spontaneous parametric down conversion (SPDC) in a nonlinear crystal placed into an optical parametric oscillator.

As a first application, we have optimized the polarization squeezing to 3.0 dB and we have reported quantum-enhancement of spin noise spectroscopy (SNS) of dense Rb vapor in natural abundance. We demonstrated improvement of the signal-to-noise ratio by 1.5 dB to 2.6 dB over the combined (power)$\otimes$(number density) ranges (0.5 mW to 4.0 mW)$\otimes$($1.5 \times 10^{12}\text{cm}^{-3}$ to $1.3 \times 10^{13}\text{cm}^{-3}$), covering the ranges used in optimized spin noise spectroscopy experiments [26, 27, 47]. We found that the only detrimental effect to squeezing is absorption of the off-resonance probe (20 GHz to the blue of the D_1 line) and we do not observe neither coupling between optical and atomic quantum noise nor back-action of the atomic ensemble onto the squeezed probe: *squeezing reduces the measurement noise at both low and high densities*, even in the saturated regime. These are new experimental observations with respect to related works on squeezed-light optical magnetometry [43, 45], in which squeezing *increased* the measurement noise above a density value which was optimized for sensitivity. However, the fact that we deal with a un-polarized atomic ensemble and off-resonance probing, together with the different source of squeezing (crystal-based versus atom-based) can explain the discrepancy with the mentioned works. We also show that squeezing improves the trade-off between statistical sensitivity and broadening effects, a qualitatively new quantum advantage. Our results provide a clear evidence that polarization squeezing can improve Faraday rotation based spin noise spectroscopy under optimized regimes with a broad range of applications in both atomic [66] and solid

state physics [25].

Secondly, we have developed a novel theoretical model by defining a standard quantum limit (SQL) for optically-detected noise spectroscopy. We have identified quantum limitations to the covariance matrix of the fit parameters estimated through fitting a sample of power noise spectra. We tested the model with the data for spin noise spectroscopy of natural abundance Rb and we demonstrated experimental performance of SNS at the SQL. We further confirm the shot noise limit to the sensitivity of the technique, by demonstrating parameter estimation below the SQL via polarization squeezing of the probe beam. These observations confirm that squeezing can reduce systematic errors on the quantities estimated through SNS, like Larmor frequency and resonance linewidth, under optimized regimes. The introduced model represents an elegant and powerful tool that can be used to identify *a priori* experimental conditions, i.e. figures of merit, that maximize the information obtainable trough noise spectroscopy and could find application not only in atomic [26] and solid state physics [125, 126], but also in cell biology [130, 131], molecular biophysics [136, 127], geophysics [132], space science [137], and quantum information processing [138, 139, 133, 134, 135].

Finally, we have reported a room temperature shot-noise-limited (SNL) optical magnetometer that achieves a best sensitivity of $70\,\mathrm{fT}/\sqrt{\mathrm{Hz}}$ at a field of $7.6\,\mu\mathrm{T}$. We demonstrated the SNL behaviour over the field range 5 μT to 75 μT, where this broad dynamic range is obtained through synchronization between amplitude modulation of the pump beam and the Larmor precession of atomic alignment (AMOR-based magnetometry). The demonstrated sensitivity is among the best reported in the class of low-frequency and scalar optical magnetometers [80, 95, 10] with classical probes and it is more than two orders of magnitude bet-

ter than what has been reported in recent works on squeezed-light magnetometers [40, 43, 44, 45]. Then, the combination of state-of-the-art sensitivity and SNL performance makes the described system a promising candidate to the application of squeezed-light to an optical magnetometer with best-in-class sensitivity.

Appendix

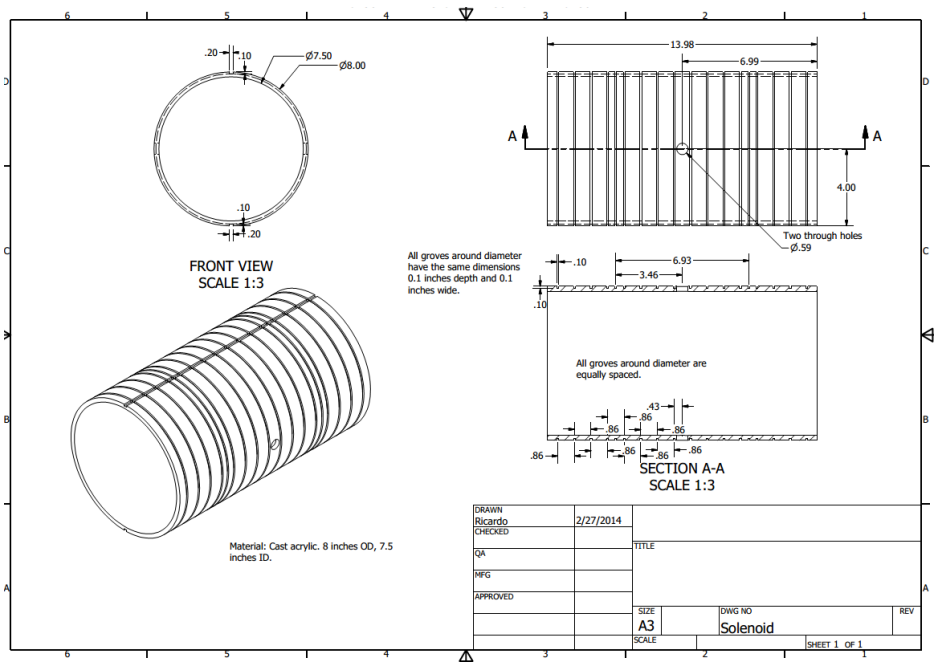

Figure 7.1: **Solenoid technical drawing**.

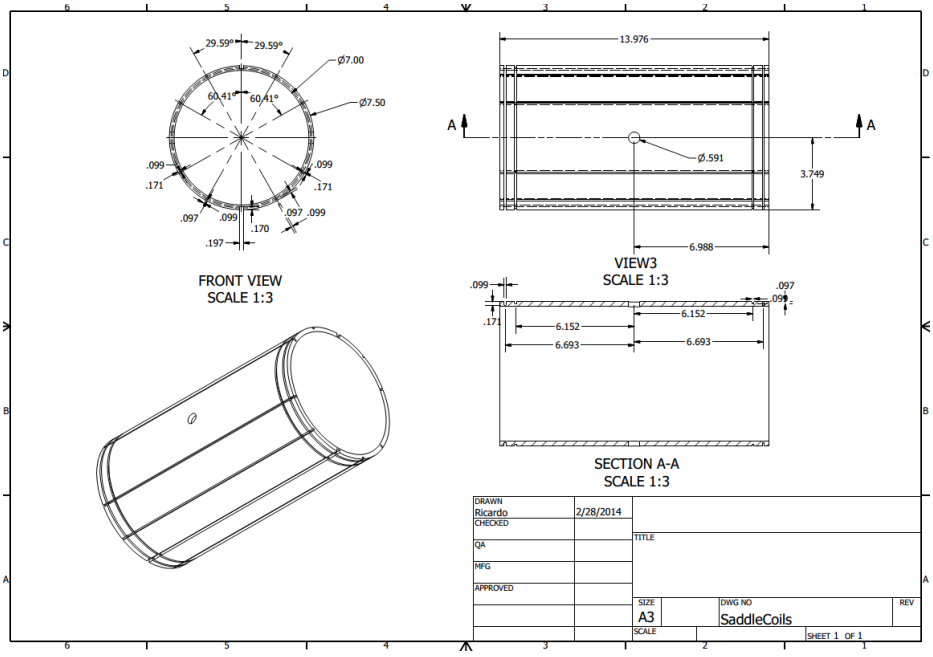

Figure 7.2: **Saddle coils technical drawing**.

List of Publications

The work presented in this thesis is related with the following publications:

- Vito Giovanni Lucivero, Pawel Anielski, Wojciech Gawlik and Morgan W. Mitchell, "Shot-noise-limited magnetometer with sub-picotesla sensitivity at room temperature", Rev. Sci. Instrum. **85**, 113108 (2014)
- Vito Giovanni Lucivero, Ricardo Jiménez-Martínez, Jia Kong, and Morgan W. Mitchell, "Squeezed-light spin noise spectroscopy", Phys. Rev. A **93**, 053802
- Jia Kong, Vito Giovanni Lucivero, Ricardo Jimnez-Martnez and Morgan W. Mitchell, "Long-term laser frequency stabilization using fiber interferometers", Rev. Sci. Instrum. **86**, 073104 (2015)

During my PhD I have been also involved in other works, which are related with but are not included in this thesis, and have been published in:

- Yannick A. de Icaza Astiz, Vito Giovanni Lucivero, R. de J. León-Montiel, and Morgan W. Mitchell, "Optimal signal recovery for pulsed balanced detection", Phys. Rev. A **90**, 033814

- Federica A. Beduini, Joanna A. Zielińska, Vito G. Lucivero, Yannick A. de Icaza Astiz, and Morgan W. Mitchell, "Interferometric Measurement of the Biphoton Wave Function", Phys. Rev. Lett. **113**, 183602

- Joanna A. Zielińska, Federica A. Beduini, Vito Giovanni Lucivero, and Morgan W. Mitchell, "Atomic filtering for hybrid continuous-variable/discrete-variable quantum optics", Opt. Express **22**, 25307-25317 (2014)

- Federica A. Beduini, Joanna A. Zielińska, Vito G. Lucivero, Yannick A. de Icaza Astiz, and Morgan W. Mitchell, "Macroscopic Quantum State Analyzed Particle by Particle", Phys. Rev. Lett. **114**, 120402

and in popular articles:

- Federica A. Beduini, Joanna A. Zielińska, Vito G. Lucivero, Yannick A. de Icaza Astiz, and Morgan W. Mitchell, "A Photonic Many-Body System, Particle by Particle", Opt. Phot. News, Highlights 2016

Bibliography

[1] M. Faraday. *Philos. Trans. R. Soc. London*, XIX:1, 1846.

[2] M. Faraday. *Philos. Mag.*, 28:294, 1846.

[3] W. Voigt. *Ann. Phys. (Leipzig)*, (4):197, 1901.

[4] W. Happer. Optical pumping. *Rev. Mod. Phys.*, 44:169–249, Apr 1972.

[5] W. Gawlik, J. Kowalski, R. Neumann, and F. Träger. Observation of the electric hexadecapole moment of free na atoms in a forward scattering experiment. *Optics Communications*, 12 (issue 4)(4):400–404, 1974.

[6] D. Budker, W. Gawlik, D. F. Kimball, S. M. Rochester, V. V. Yashchuk, and A. Weis. Resonant nonlinear magneto-optical effects in atoms. *Rev. Mod. Phys.*, 74(4):1153–1201, 2002.

[7] Dmitry Budker and Michael Romalis. Optical magnetometry. *Nat Phys*, 3(4):227–234, 2007.

[8] I. K. Kominis, T. W. Kornack, J. C. Allred, and M. V. Romalis. A subfemtotesla multichannel atomic magnetometer. *Nature*, 422(6932):596–599, April 2003.

[9] S.-K. Lee, K. L. Sauer, S. J. Seltzer, O. Alem, and M. V. Romalis. Subfemtotesla radio-frequency atomic magnetometer for detection of nuclear quadrupole resonance. *Applied Physics Letters*, 89(21), 2006.

[10] D. Sheng, S. Li, N. Dural, and M. V. Romalis. Subfemtotesla scalar atomic magnetometry using multipass cells. *Phys. Rev. Lett.*, 110:160802, 2013.

[11] G. Bison, N. Castagna, A. Hofer, P. Knowles, J.-L. Schenker, M. Kasprzak, H. Saudan, and A. Weis. A room temperature 19-channel magnetic field mapping device for cardiac signals. *Applied Physics Letters*, 95(17):173701, 2009.

[12] Svenja Knappe, Tilmann H. Sander, Olaf Kosch, Frank Wiekhorst, John Kitching, and Lutz Trahms. Cross-validation of microfabricated atomic magnetometers with superconducting quantum interference devices for biomagnetic applications. *Applied Physics Letters*, 97(13):133703, 2010.

[13] Cort Johnson, Peter D. D. Schwindt, and Michael Weisend. Magnetoencephalography with a two-color pump-probe, fiber-coupled atomic magnetometer. *Applied Physics Letters*, 97(24):243703, 2010.

[14] E B Alexandrov, M V Balabas, V N Kulyasov, A E Ivanov, A S Pazgalev, J L Rasson, A K Vershovski, and N N Yakobson. Three-component variometer based on a scalar potassium sensor. *Measurement Science and Technology*, 15(5):918, 2004.

[15] A. K. Vershovskii, M. V. Balabas, A. É. Ivanov, V. N. Kulyasov, A. S. Pazgalev, and E. B. Aleksandrov. Fast three-component magnetometer-variometer based on a cesium sensor. *Technical Physics*, 51(1):112–117, 2006.

[16] H. B. Dang, A. C. Maloof, and M. V. Romalis. Ultrahigh sensitivity magnetic field and magnetization measurements with an atomic magnetometer. *Applied Physics Letters*, 97(15), 2010.

[17] B.G. Ledley. Magnetometers for space measurements over a wide range of field intensities. *Rev. Phys. Appl.*, 5:164, 1970.

[18] A. Wicht et al E. Luvsandamdin, G. Mura. *CLEO EUROPE/EQEC*, 2011.

[19] D. Budker, S. K. Lamoreaux, A. O. Sushkov, and O. P. Sushkov. Sensitivity of condensed-matter p- and t-violation experiments. *Phys. Rev. A*, 73(2):022107, 2006.

[20] L. W. Cheuk S. J. Smullin M. Smiciklas, J. M. Brown and M. V. Romalis. New test of local lorentz invariance using a 21ne-rb-k-rb-k comagnetometer. *Phys. Rev. Lett.*, 107:171604, 2011.

[21] M. Pospelov, S. Pustelny, M. P. Ledbetter, D. F. Jackson Kimball, W. Gawlik, and D. Budker. Detecting domain walls of axionlike models using terrestrial experiments. *Phys. Rev. Lett.*, 110:021803, Jan 2013.

[22] Michael V. Romalis. Atomic sensors: Chip-scale magnetometers. *Nat Photon*, 1(11):613–614, November 2007.

[23] F. Bloch. Nuclear induction. *Phys. Rev.*, 70:460–474, Oct 1946.

[24] Valerii S. Zapasskii. Spin-noise spectroscopy: from proof of principle to applications. *Adv. Opt. Photon.*, 5(2):131–168, 2013.

[25] Jens Hübner, Fabian Berski, Ramin Dahbashi, and Michael Oestreich. The rise of spin noise spectroscopy in semiconductors: From acoustic to ghz frequencies. *physica status solidi (b)*, 251(9):1824–1838, 2014.

[26] S. A. Crooker, D. G. Rickel, A. V. Balatsky, and D. L. Smith. Spectroscopy of spontaneous spin noise as a probe of spin dynamics and magnetic resonance. *Nature*, 431(7004):49–52, September 2004.

[27] G. E. Katsoprinakis, A. T. Dellis, and I. K. Kominis. Measurement of transverse spin-relaxation rates in a rubidium vapor by use of spin-noise spectroscopy. *Phys. Rev. A*, 75:042502, Apr 2007.

[28] M. Oestreich, M. Römer, R. J. Haug, and D. Hägele. Spin noise spectroscopy in gaas. *Phys. Rev. Lett.*, 95:216603, Nov 2005.

[29] S. A. Crooker, J. Brandt, C. Sandfort, A. Greilich, D. R. Yakovlev, D. Reuter, A. D. Wieck, and M. Bayer. Spin noise of electrons and holes in self-assembled quantum dots. *Phys. Rev. Lett.*, 104:036601, Jan 2010.

[30] D. Rugar, R. Budakian, H. J. Mamin, and B. W. Chui. Single spin detection by magnetic resonance force microscopy. *Nature*, 430(6997):329–332, July 2004.

[31] R. Budakian, H. J. Mamin, B. W. Chui, and D. Rugar. Creating order from random fluctuations in small spin ensembles. *Science*, 307(5708):408–411, 2005.

[32] Gopalakrishnan Balasubramanian, I. Y. Chan, Roman Kolesov, Mohannad Al-Hmoud, Julia Tisler, Chang Shin, Changdong Kim, Aleksander Wojcik, Philip R. Hemmer, Anke Krueger, Tobias Hanke, Alfred Leitenstorfer, Rudolf Bratschitsch, Fedor Jelezko, and Jorg Wrachtrup. Nanoscale imaging magnetometry with diamond spins under ambient conditions. *Nature*, 455(7213):648–651, October 2008.

[33] J. R. Maze, P. L. Stanwix, J. S. Hodges, S. Hong, J. M. Taylor, P. Cappellaro, L. Jiang, M. V. Gurudev Dutt, E. Togan, A. S. Zibrov, A. Yacoby, R. L. Walsworth, and M. D. Lukin. Nanoscale magnetic sensing with an individual electronic spin in diamond. *Nature*, 455(7213):644–647, October 2008.

[34] H. J. Mamin, M. H. Sherwood, and D. Rugar. Detecting external electron spins using nitrogen-vacancy centers. *Phys. Rev. B*, 86:195422, Nov 2012.

[35] B. Aleksandrov and V. S. Zapasskii. Magnetic resonance in the faraday-rotation noi spectrum. *Sov. Phys. JETP*, 54:64, 1981.

[36] Carlton M. Caves. Quantum-mechanical noise in an interferometer. *Phys. Rev. D*, 23:1693–1708, Apr 1981.

[37] P. Grangier, R. E. Slusher, B. Yurke, and A. LaPorta. Squeezed-light ˘ enhanced polarization interferometer. *Phys. Rev. Lett.*, 59:2153–2156, Nov 1987.

[38] E. S. Polzik, J. Carri, and H. J. Kimble. Spectroscopy with squeezed light. *Phys. Rev. Lett.*, 68:3020–3023, May 1992.

[39] J. L. Sørensen, J. Hald, and E. S. Polzik. Quantum noise of an atomic spin polarization measurement. *Phys. Rev. Lett.*, 80:3487–3490, Apr 1998.

[40] Florian Wolfgramm, Alessandro Cerè, Federica A. Beduini, Ana Predojević, Marco Koschorreck, and Morgan W. Mitchell. Squeezed-light optical magnetometry. *Phys. Rev. Lett.*, 105(5):053601–, 2010.

[41] LIGO Scientific Collaboration. Enhanced sensitivity of the ligo gravitational wave detector by using squeezed states of light. *Nat. Photonics*, 7:613, 2013.

[42] Michael A. Taylor, Jiri Janousek, Vincent Daria, Joachim Knittel, Boris Hage, BachorHans-A., and Warwick P. Bowen. Biological measurement beyond the quantum limit. *Nat Photon*, 7(3):229–233, March 2013.

[43] Travis Horrom, Robinjeet Singh, Jonathan P. Dowling, and Eugeniy E. Mikhailov. Quantum-enhanced magnetometer with low-frequency squeezing. *Phys. Rev. A*, 86(2):023803, 2012.

[44] N. Otterstrom, R. C. Pooser, and B. J. Lawrie. Nonlinear optical magnetometry with accessible in situ optical squeezing. *Opt. Lett.*, 39(22):6533–6536, Nov 2014.

[45] Irina Novikova, Eugeniy E. Mikhailov, and Yanhong Xiao. Excess optical quantum noise in atomic sensors. *Phys. Rev. A*, 91:051804, May 2015.

[46] V. Shah, G. Vasilakis, and M. V. Romalis. High bandwidth atomic magnetometery with continuous quantum nondemolition measurements. *Phys. Rev. Lett.*, 104(1):013601–, 2010.

[47] A. T. Dellis, M. Loulakis, and I. K. Kominis. Spin-noise correlations and spin-noise exchange driven by low-field spin-exchange collisions. *Phys. Rev. A*, 90:032705, Sep 2014.

[48] Vittorio Giovannetti, Seth Lloyd, and Lorenzo Maccone. Quantum metrology. *Phys. Rev. Lett.*, 96:010401, Jan 2006.

[49] W. Schottky. ber spontane stromschwankungen in verschiedenen elektrizittsleitern. *Annalen der Physik*, 362(23):541–567, 1918.

[50] Rodney Loudon. *The Quantum Theory of Light*. Oxford University Press, 2000.

[51] Luiz Davidovich. Sub-poissonian processes in quantum optics. *Rev. Mod. Phys.*, 68:127–173, Jan 1996.

[52] Hans-A Bachor and Timothy C. Ralph. *A Guide to Experiments in Quantum Optics*. 2004.

[53] Marlan O. Scully and M. Suhail Zubairy. *Quantum Optics*. Cambridge University Press, 1997.

[54] H. P. Robertson. The uncertainty principle. *Phys. Rev.*, 34:163–164, Jul 1929.

[55] Warwick P. Bowen, Roman Schnabel, Hans-A. Bachor, and Ping Koy Lam. Polarization squeezing of continuous variable stokes parameters. *Phys. Rev. Lett.*, 88:093601, Feb 2002.

[56] Natalia Korolkova, Gerd Leuchs, Rodney Loudon, Timothy C. Ralph, and Christine Silberhorn. Polarization squeezing and continuous-variable polarization entanglement. *Phys. Rev. A*, 65:052306, Apr 2002.

[57] Roman Schnabel, Warwick P. Bowen, Nicolas Treps, Timothy C. Ralph, Hans-A. Bachor, and Ping Koy Lam. Stokes-operator-squeezed continuous-variable polarization states. *Phys. Rev. A*, 67:012316, Jan 2003.

[58] M. Faraday. *Experimental researches in Electricity*, volume III. Taylor, London, 1855.

[59] D. Macaluso and O. M. Corbino. *Nuovo Cimento*, 8:257, 1898.

[60] D. Macaluso and O. M. Corbino. *Nuovo Cimento*, page 384, 1898.

[61] P. Zeeman. *Phil. Mag.*, 43:226, 1897.

[62] P. Zeeman. *Nature*, 55:347, 1897.

[63] V. Voigt. Magneto- und elektooptik. *Druck und Verlag von B. G. Teubner*, 1908.

[64] Isao Hirano. Forward scattering magneto-optical spectra of the cs d_2 line. *Phys. Rev. A*, 50:4650–4656, Dec 1994.

[65] V. S. Letokhov and V. P. Chebotayev. *Nonlinear Laser Spectroscopy.* Springer, New York, 1977.

[66] V. S. Zapasskii, A. Greilich, S. A. Crooker, Yan Li, G. G. Kozlov, D. R. Yakovlev, D. Reuter, A. D. Wieck, and M. Bayer. Optical spectroscopy of spin noise. *Phys. Rev. Lett.*, 110:176601, Apr 2013.

[67] Takahito Tanimura, Daisuke Akamatsu, Yoshihiko Yokoi, Akira Furusawa, and Mikio Kozuma. Generation of a squeezed vacuum resonant on a rubidium d1 line with periodically poled ktiopo4. *Opt. Lett.*, 31(15):2344–2346, 2006.

[68] G Hétet, O Glöckl, K A Pilypas, C C Harb, B C Buchler, H-A Bachor, and P K Lam. Squeezed light for bandwidth-limited atom optics experiments at the rubidium d1 line. *Journal of Physics B: Atomic, Molecular and Optical Physics*, 40(1):221, 2007.

[69] A. Predojevic, Z. Zhai, J. M. Caballero, and M. W. Mitchell. Rubidium resonant squeezed light from a diode-pumped optical-parametric oscillator. *Phys. Rev. A*, 78(6):063820, 2008.

[70] Jürgen Appel, Eden Figueroa, Dmitry Korystov, M. Lobino, and A. I. Lvovsky. Quantum memory for squeezed light. *Phys. Rev. Lett.*, 100:093602, 2008.

[71] Sidney Burks, Jérémie Ortalo, Antonino Chiummo, Xiaojun Jia, Fabrizio Villa, Alberto Bramati, Julien Laurat, and Elisabeth Giacobino. Vacuum squeezed light for atomic memories at the d2 cesium line. *Opt. Express*, 17(5):3777–3781, 2009.

[72] Vito Giovanni Lucivero, Ricardo Jiménez-Martínez, Jia Kong, and Morgan W. Mitchell. Squeezed-light spin noise spectroscopy. *Phys. Rev. A*, 93:053802, May 2016.

[73] William Happer, Yuan-Yu Jau, and Thad Walker. *Optically pumped atoms.* John Wiley & Sons, 2010.

[74] W. Gawlik, J. Kowalski, R. Neumann, and F. Träger. *Phys. Lett.*, 48A:283, 1974.

[75] Dmitry Budker, Valeriy Yashchuk, and Max Zolotorev. Nonlinear magneto-optic effects with ultranarrow widths. *Phys. Rev. Lett.*, 81(26):5788–5791, 1998.

[76] S. Brandt, A. Nagel, R. Wynands, and D. Meschede. Buffer-gas-induced linewidth reduction of coherent dark resonances to below 50hz. *Phys. Rev. A*, 56(2):R1063–R1066, 1997.

[77] Andrey B. Matsko Irina Novikova and George R. Welch. Influence of a buffer gas on nonlinear magneto-optical polarization rotation. *J. Opt. Soc. Am. B*, 22:44–56, 2005.

[78] Eric P. Corsini, Todor Karaulanov, Mikhail Balabas, and Dmitry Budker. Hyperfine frequency shift and Zeeman relaxation in alkali-metal-vapor cells with antirelaxation alkene coating. *Phys. Rev. A*, 87:022901, 2013.

[79] W. Gawlik, L. Krzemień, S. Pustelny, D. Sangla, J. Zachorowski, M. Graf, A. O. Sushkov, and D. Budker. Nonlinear magneto-optical rotation with amplitude modulated light. *Applied Physics Letters*, 88(13):131108, 2006.

[80] D. Budker, D. F. Kimball, V. V. Yashchuk, and M. Zolotorev. Nonlinear magneto-optical rotation with frequency-modulated light. *Phys. Rev. A*, 65(5):055403, 2002.

[81] C. Cohen-Tannoudji. Optical pumping in lasers. *Atomic Physics 4, Plenum Press*, page p. 589, 1974.

[82] C. Cohen-Tannoudji. Frontiers in laser spectroscopy. *North-Holland*, Les Houches Summer School, 1975.

[83] S. I. Kanorsky, A. Weis, J. Wurster, and T. W. Hänsch. Quantitative investigation of the resonant nonlinear faraday effect under conditions of optical hyperfine pumping. *Phys. Rev. A*, 47:1220–1226, Feb 1993.

[84] Vito Giovanni Lucivero, Pawel Anielski, Wojciech Gawlik, and Morgan W. Mitchell. Shot-noise-limited magnetometer with sub-picotesla sensitivity at room temperature. *Review of Scientific Instruments*, 85(11):–, 2014.

[85] J. M. Higbie, E. Corsini, and D. Budker. Robust, high-speed, all-optical atomic magnetometer. *Review of Scientific Instruments*, 77(11):113106, 2006.

[86] B. Patton, O. O. Versolato, D. C. Hovde, E. Corsini, J. M. Higbie, and D. Budker. A remotely interrogated all-optical 87rb magnetometer. *Applied Physics Letters*, 101(8):083502, 2012.

[87] J. Zachorowski P. Wlodarczyk, S. Pustelny and M. Lipinski. Modeling an optical magnetometer electronic circuit analysis and optimization. *J. Inst. (IOP Journal of Instrumentation)*, JINST 7:P07015, 2012.

[88] D. Budker M. Auzinsh and S. M. Rochester. *Optically Polarized Atoms.* Oxford University Press, 2010.

[89] D. Budker and D. F.J. Kimball, editors. *Optical Magnetometry.* Cambridge University Press, 2013.

[90] S. Li, P. Vachaspati, D. Sheng, N. Dural, and M. V. Romalis. Optical rotation in excess of 100 rad generated by rb vapor in a multipass cell. *Phys. Rev. A*, 84:061403, Dec 2011.

[91] M. Fleischhauer, A. B. Matsko, and M. O. Scully. Quantum limit of optical magnetometry in the presence of ac stark shifts. *Phys. Rev. A*, 62:013808, Jun 2000.

[92] W. Wasilewski, K. Jensen, H. Krauter, J. J. Renema, M. V. Balabas, and E. S. Polzik. Quantum noise limited and entanglement-assisted magnetometry. *Phys. Rev. Lett.*, 104(13):133601–, March 2010.

[93] M. Koschorreck, M. Napolitano, B. Dubost, and M. W. Mitchell. Sub-projection-noise sensitivity in broadband atomic magnetometry. *Phys. Rev. Lett.*, 104(9):093602, 2010.

[94] R. J. Sewell, M. Koschorreck, M. Napolitano, B. Dubost, N. Behbood, and M. W. Mitchell. Magnetic sensitivity beyond the projection noise limit by spin squeezing. *Phys. Rev. Lett.*, 109:253605, 2012.

[95] S. Pustelny, A. Wojciechowski, M. Gring, M. Kotyrba, J. Zachorowski, and W. Gawlik. Magnetometry based on nonlinear magneto-optical rotation with amplitude-modulated light. *Journal of Applied Physics*, 103(6):063108, 2008.

[96] Federica A. Beduini, Joanna A. Zielińska, Vito G. Lucivero, Yannick A. de Icaza Astiz, and Morgan W. Mitchell. Macroscopic quantum state analyzed particle by particle. *Phys. Rev. Lett.*, 114:120402, Mar 2015.

[97] Paul Siddons, Charles S Adams, Chang Ge, and Ifan G Hughes. Absolute absorption on rubidium d lines: comparison between theory and experiment. *Journal of Physics B: Atomic, Molecular and Optical Physics*, 41(15):155004, 2008.

[98] M. V. Romalis, E. Miron, and G. D. Cates. Pressure broadening of rb D_1 and D_2 lines by ^{3}he, ^{4}he, n_2, and xe: Line cores and near wings. *Phys. Rev. A*, 56:4569–4578, Dec 1997.

[99] E. A. Donley, E. Hodby, L. Hollberg, and J. Kitching. Demonstration of high-performance compact magnetic shields for chip-scale atomic devices. *Review of Scientific Instruments*, 78(8), 2007.

[100] D. M. Ginsberg and Melvin J. Melchner. Optimum geometry of saddle shaped coils for generating a uniform magnetic field. *Review of Scientific Instruments*, 41(1):122–123, 1970.

[101] A.Predojevic. *Rubidium resonant squeezed light from a diode-pumped optical parametric oscillator*. PhD Thesis, 2009.

[102] Eric D. Black. An introduction to pounddreverhall laser frequency stabilization. *American Journal of Physics*, 69(1):79–87, 2001.

[103] Florian Wolfgramm. *Atomic quantum metrology with narrowband entangled and squeezed states of light*. PhD Thesis, 2012.

[104] Federica A. Beduini, Joanna A. Zielińska, Vito G. Lucivero, Yannick A. de Icaza Astiz, and Morgan W. Mitchell. Interferometric measurement of the biphoton wave function. *Phys. Rev. Lett.*, 113:183602, Oct 2014.

[105] Jia Kong, Vito Giovanni Lucivero, Ricardo Jiménez-Martínez, and Morgan W. Mitchell. Long-term laser frequency stabilization using fiber interferometers. *Review of Scientific Instruments*, 86(7):–, 2015.

[106] M. Römer, J. Hübner, and M. Oestreich. Spatially resolved doping concentration measurement in semiconductors via spin noise spectroscopy. *Applied Physics Letters*, 94(11):–, 2009.

[107] Qiong Huang and Duncan S. Steel. Optical excitation effects on spin-noise spectroscopy in semiconductors. *Phys. Rev. B*, 83:155204, Apr 2011.

[108] Fabian Berski, Hendrik Kuhn, Jan G. Lonnemann, Jens Hübner, and Michael Oestreich. Ultrahigh bandwidth spin noise spectroscopy: Detection of large g-factor fluctuations in highly-n-doped gaas. *Phys. Rev. Lett.*, 111:186602, Oct 2013.

[109] S. V. Poltavtsev, I. I. Ryzhov, M. M. Glazov, G. G. Kozlov, V. S. Zapasskii, A. V. Kavokin, P. G. Lagoudakis, D. S. Smirnov, and E. L. Ivchenko. Spin

noise spectroscopy of a single quantum well microcavity. *Phys. Rev. B*, 89:081304, Feb 2014.

[110] Yan Li, N. Sinitsyn, D. L. Smith, D. Reuter, A. D. Wieck, D. R. Yakovlev, M. Bayer, and S. A. Crooker. Intrinsic spin fluctuations reveal the dynamical response function of holes coupled to nuclear spin baths in (in,ga)as quantum dots. *Phys. Rev. Lett.*, 108:186603, May 2012.

[111] Ramin Dahbashi, Jens Hübner, Fabian Berski, Klaus Pierz, and Michael Oestreich. Optical spin noise of a single hole spin localized in an (inga)as quantum dot. *Phys. Rev. Lett.*, 112:156601, Apr 2014.

[112] Luyi Yang, P. Glasenapp, A. Greilich, D. Reuter, A. D. Wieck, D. R. Yakovlev, M. Bayer, and S. A. Crooker. Two-colour spin noise spectroscopy and fluctuation correlations reveal homogeneous linewidths within quantum-dot ensembles. *Nat Commun*, 5:–, September 2014.

[113] P. Glasenapp, N.A. Sinitsyn, Luyi Yang, D.G. Rickel, D. Roy, A. Greilich, M. Bayer, and S.A. Crooker. Spin noise spectroscopy beyond thermal equilibrium and linear response. *Phys. Rev. Lett.*, 113(15):156601–, October 2014.

[114] Dibyendu Roy, Luyi Yang, Scott A. Crooker, and Nikolai A. Sinitsyn. Cross-correlation spin noise spectroscopy of heterogeneous interacting spin systems. *Scientific Reports*, 5:9573–, April 2015.

[115] Tycho Sleator, Erwin L. Hahn, Claude Hilbert, and John Clarke. Nuclear-spin noise. *Phys. Rev. Lett.*, 55:1742–1745, Oct 1985.

[116] W. Reim, R. H. Koch, A. P. Malozemoff, M. B. Ketchen, and H. Maletta. Magnetic equilibrium noise in spin-glasses: $eu_{0.4}sr_{0.6}s$. *Phys. Rev. Lett.*, 57:905–908, Aug 1986.

[117] C. L. Degen, M. Poggio, H. J. Mamin, and D. Rugar. Role of spin noise in the detection of nanoscale ensembles of nuclear spins. *Phys. Rev. Lett.*, 99:250601, Dec 2007.

[118] Georg M. Müller, Michael Oestreich, Michael Römer, and Jens Hübner. Semiconductor spin noise spectroscopy: Fundamentals, accomplishments, and challenges. *Physica E: Low-dimensional Systems and Nanostructures*, 43(2):569–587, December 2010.

[119] P. Glasenapp, A. Greilich, I. I. Ryzhov, V. S. Zapasskii, D. R. Yakovlev, G. G. Kozlov, and M. Bayer. Resources of polarimetric sensitivity in spin noise spectroscopy. *Phys. Rev. B*, 88:165314, Oct 2013.

[120] Ricardo Jiménez-Martínez, W. Clark Griffith, Svenja Knappe, John Kitching, and Mark Prouty. High-bandwidth optical magnetometer. *J. Opt. Soc. Am. B*, 29(12):3398–3403, Dec 2012.

[121] Kirk McKenzie, Eugeniy E Mikhailov, Keisuke Goda, Ping Koy Lam, Nicolai Grosse, Malcolm B Gray, Nergis Mavalvala, and David E McClelland. Quantum noise locking. *Journal of Optics B: Quantum and Semiclassical Optics*, 7(10):S421, 2005.

[122] Harald Cramr. *Mathematical Methods of Statistics*. Princeton Univ. Press., 1946.

[123] Calyampudi Radakrishna Rao. Information and the accuracy attainable in the estimation of statistical parameters. *Bulletin of the Calcutta Mathematical Society*, 37:81–89, 1945.

[124] André Klein, Guy Mélard, and Toufik Zahaf. Construction of the exact Fisher information matrix of Gaussian time series models by means of matrix differential rules. *Linear Algebra and its Applications*, 321(1–3):209 – 232, 2000. Eighth Special Issue on Linear Algebra and Statistics.

[125] J. Sikula and L. Stourac. Noise spectroscopy of semiconductor materials and devices. In *Microelectronics, 2002. MIEL 2002. 23rd International Conference on*, volume 2, pages 767–772 vol.2, 2002.

[126] S A Vitusevich, M V Petrychuk, A M Kurakin, S V Danylyuk, D Mayer, Z Bougrioua, A V Naumov, A E Belyaev, and N Klein. Noise spectroscopy of AlGaN/GaN HEMT structures with long channels. *Journal of Statistical Mechanics: Theory and Experiment*, 2009(01):P01046, 2009.

[127] Kirstine Berg-Sørensen and Henrik Flyvbjerg. Power spectrum analysis for optical tweezers. *Review of Scientific Instruments*, 75(3):594–612, 2004.

[128] John Wishart. The generalized product moment distribution in samples from a normal multivariate population. *Biometrika*, 20A (1-2):32–52, 1928.

[129] J.F. Kenney and E.S. Keeping. *Mathematics of statistics, part two, by J.F.Kenney and E.S.Keeping: 2nd ed.* Princeton, NJ: Van Nostrand, 1951.

[130] Iva Marija Tolić-Nørrelykke, Emilia-Laura Munteanu, Genevieve Thon, Lene Oddershede, and Kirstine Berg-Sørensen. Anomalous diffusion in living yeast cells. *Phys. Rev. Lett.*, 93:078102, Aug 2004.

[131] Michael A Taylor, Joachim Knittel, and Warwick P Bowen. Fundamental constraints on particle tracking with optical tweezers. *New Journal of Physics*, 15(2):023018, 2013.

[132] A. V. Descherevsky, A. A. Lukk, A. Y. Sidorin, G. V. Vstovsky, and S. F. Timashev. Flicker-noise spectroscopy in earthquake prediction research. *Natural Hazards and Earth System Science*, 3(3/4):159–164, 2003.

[133] Tatsuro Yuge, Susumu Sasaki, and Yoshiro Hirayama. Measurement of the noise spectrum using a multiple-pulse sequence. *Phys. Rev. Lett.*, 107:170504, Oct 2011.

[134] Jonas Bylander, Simon Gustavsson, Fei Yan, Fumiki Yoshihara, Khalil Harrabi, George Fitch, David G. Cory, Yasunobu Nakamura, Jaw-Shen Tsai, and William D. Oliver. Noise spectroscopy through dynamical decoupling with a superconducting flux qubit. *Nat Phys*, 7(7):565–570, 07 2011.

[135] J. Medford, Ł. Cywiński, C. Barthel, C. M. Marcus, M. P. Hanson, and A. C. Gossard. Scaling of dynamical decoupling for spin qubits. *Phys. Rev. Lett.*, 108:086802, Feb 2012.

[136] Masaru Kawakami, Katherine Byrne, Bhavin Khatri, Tom C. B. Mcleish, Sheena E. Radford, and D. Alastair Smith. Viscoelastic properties of single polysaccharide molecules determined by analysis of thermally driven oscillations of an atomic force microscope cantilever. *Langmuir*, 20(21):9299–9303, 10 2004.

[137] Michel Moncuquet, Alain Lecacheux, Nicole Meyer-Vernet, Baptiste Cecconi, and William S. Kurth. Quasi thermal noise spectroscopy in the inner

magnetosphere of saturn with cassini/rpws: Electron temperatures and density. *Geophysical Research Letters*, 32(20), 2005. L20S02.

[138] Michael J. Biercuk, Hermann Uys, Aaron P. VanDevender, Nobuyasu Shiga, Wayne M. Itano, and John J. Bollinger. Optimized dynamical decoupling in a model quantum memory. *Nature*, 458(7241):996–1000, 04 2009.

[139] Gonzalo A. Álvarez and Dieter Suter. Measuring the spectrum of colored noise by dynamical decoupling. *Phys. Rev. Lett.*, 107:230501, Nov 2011.

[140] Rubidium 85 d line data. *available online at http://steck.us/alkalidata*, (revision 2.1.5, 19 September 2012).

[141] V. Acosta, M. P. Ledbetter, S. M. Rochester, D. Budker, D. F. Jackson Kimball, D. C. Hovde, W. Gawlik, S. Pustelny, J. Zachorowski, and V. V. Yashchuk. Nonlinear magneto-optical rotation with frequency-modulated light in the geophysical field range. *Phys. Rev. A*, 73(5):053404, 2006.

[142] D. F. Jackson Kimball, L. R. Jacome, Srikanth Guttikonda, Eric J. Bahr, and Lok Fai Chan. Magnetometric sensitivity optimization for nonlinear optical rotation with frequency-modulated light: Rubidium d2 line. *Journal of Applied Physics*, 106(6):063113, 2009.

[143] E. Breschi, Z. D. Grujić, P. Knowles, and A. Weis. A high-sensitivity push-pull magnetometer. *Applied Physics Letters*, 104(2):023501, 2014.

[144] S. J. Smullin, I. M. Savukov, G. Vasilakis, R. K. Ghosh, and M. V. Romalis. Low-noise high-density alkali-metal scalar magnetometer. *Phys. Rev. A*, 80:033420, 2009.

[145] M. Koschorreck, M. Napolitano, B. Dubost, and M. W. Mitchell. Quantum nondemolition measurement of large-spin ensembles by dynamical decoupling. *Phys. Rev. Lett.*, 105(9):093602, 2010.

[146] R. J. Sewell, M. Napolitano, N. Behbood, G. Colangelo, and M. W. Mitchell. Certified quantum non-demolition measurement of a macroscopic material system. *Nat Photon*, 7(7):517–520, 2013.

[147] G. Vasilakis, V. Shah, and M. V. Romalis. Stroboscopic backaction evasion in a dense alkali-metal vapor. *Phys. Rev. Lett.*, 106:143601, 2011.

[148] V. Schultze, R. IJsselsteijn, and H.-G. Meyer. Noise reduction in optically pumped magnetometer assemblies. *Applied Physics B*, 100:717–724, 2010.

[149] Volkmar Schultze, Rob IJsselsteijn, Theo Scholtes, Stefan Woetzel, and Hans-Georg Meyer. Characteristics and performance of an intensity-modulated optically pumped magnetometer in comparison to the classical Mx magnetometer. *Opt. Express*, 20:14201–14212, 2012.

[150] S. Pustelny, D. F. Jackson Kimball, S. M. Rochester, V. V. Yashchuk, and D. Budker. Influence of magnetic-field inhomogeneity on nonlinear magneto-optical resonances. *Phys. Rev. A*, 74(6):063406, 2006.

[151] G. Bison S. Groeger and A. Weis. Design and performance of laser-pumped cs magnetometers for the planned ucn-edm experiment at psi. *J. Res. Natl. Inst. Stand. Technol.*, 110:179–183, 2005.

[152] Yannick A. de Icaza Astiz, Vito Giovanni Lucivero, R. de J. León-Montiel, and Morgan W. Mitchell. Optimal signal recovery for pulsed balanced detection. *Phys. Rev. A*, 90:033814, Sep 2014.

[153] Henning Vahlbruch, Simon Chelkowski, Boris Hage, Alexander Franzen, Karsten Danzmann, and Roman Schnabel. Coherent control of vacuum squeezing in the gravitational-wave detection band. *Phys. Rev. Lett.*, 97:011101, 2006.

[154] V. M. Acosta, M. Auzinsh, W. Gawlik, P. Grisins, J. M. Higbie, D. F. Jackson Kimball, L. Krzemien, M. P. Ledbetter, S. Pustelny, S. M. Rochester, V. V. Yashchuk, and D. Budker. Production and detection of atomic hexadecapole at earth's magnetic field. *Opt. Express*, 16(15):11423–11430, 2008.

[155] K. Jensen, V. M. Acosta, J. M. Higbie, M. P. Ledbetter, S. M. Rochester, and D. Budker. Cancellation of nonlinear Zeeman shifts with light shifts. *Phys. Rev. A*, 79(2):023406–, 2009.

[156] W. Chalupczak, A. Wojciechowski, S. Pustelny, and W. Gawlik. Competition between the tensor light shift and nonlinear Zeeman effect. *Phys. Rev. A*, 82(2):023417, 2010.

Acknowledgements

The work presented in this thesis concludes more than 5 amazing years of PhD in Barcelona. During this long time I have met many people who have been of great importance in both my personal and professional life and have helped me in achieving this great objective.

First of all, I am deeply grateful to my thesis advisor Prof. Morgan W. Mitchell for giving me the opportunity to join his amazing group after my difficult start at ICFO. He has been a great and constant guide, both in experiments and theory, from the first till the last day with endless dedication and passion. Morgan is a great leader and an amazing teacher. I really appreciated its ability to maximize my potential and to correct my faults and its patience, sometimes, in explaining to me things n times (often $n \gg 1$). It has been a privilege to learn a huge amount of physics and to be constantly inspired by such a great scientist.

Secondly, I want to thank my colleagues Ricardo Jiménez-Martínez and Jia Kong for working with me during the last three years, by combining great synergy and professionality to friendship and fun, and for being a team that will be really difficult to find again. My work would have never been achieved without their hard work, talent and dedication and I am deeply grateful for that.

Next, I would like to thank my other lab-mates Florian Wolfgramm, even if for few weeks, Yannick de Icaza Astiz and Federica Beduini for introducing me to the lab and for teaching me all its challenges with great professionality, and Joanna Zielinska for sharing the lab and a fantastic trip in Andalucia. I also thank all of them for allowing me to improve my dj skills in the lab, yo! :)

Furthermore, I would like to thank all the past and present members of Morgan's group: Ferran Martin, my first office-mate in the group, Giorgio Colangelo, my "brother in PhD", Mario Napolitano, Rob Sewell, Naeimeh Behbood, Silvana Palacios, Simon Coop, Pau Gomez, Thomas Vanderbruggen, Natali Martinez, Martijn Jasperse, Jayadev Vijayan, Charikleia Troullinou, Lluís, Joaquin, Ignasi, Lorena Bianchet, Nan Li, Vindhiya Prakash and my old good friend Natalia Bruno. It has been a great experience to work in such multicultural team and sharing great days with all of you.

My special thanks go to Prof. Wojciech Gawlik for giving the opportunity to spend 4 months of my PhD at the Institute of Physics of the Jagiellonian University in Krakow. This has been not only a scientifically productive period, very important for the development of my PhD project, but also a wonderful life experience. I would like to thank my polish friends Paweł Anielski for working with me to the AMOR magnetometer, Adam Wojciechowski for useful scientific discussion and barbecues, Marcin Piotrowski for lending me a bike in Krakow, Krystian Sycz for the relaxing ping-pong, Michał Grabka, Julia Sudyka and Ada Umiska for sharing the lab during my stay in Poland.

ICFO has been a unique place where to work. I would especially like to thank Mónica, Mara José and Mercedes for their kindness at the frontdesk, Santiago, Magda and Elena for their efficiency with all the purchasing, Xavi and his team

for their fantastic work (I will finally bring him the promised “limoncello”), José Carlos and the electronic workshop, Juana and Mery for the relaxing discussions at the cafeteria (sin cebolla). I also want to thank Marta García Matos and Jordi Andilla for giving me the opportunity to join the fantastic ICFOband, with whom I had great time and fun by playing in several events. I want to thank all the members of the ICFOband: Ignacio de Miguel and his sunglasses, Núria Segú and her hard-rock voice, Carlo Manzo for the bassline, Francesco Ricci for its talent and passion, Darrick Chang for the progressive touch in the first ICFOband's song and the other voices Carlos, Auxi and Alessio. Thank you guys, I will miss the ICFOband too!

I send big thanks to my beloved friends Giorgio Colangelo, Michela Badioli, Nicolò Accanto and Emanuele Distante with whom I have shared tons of experiences, travels, concerts, dinners, games, playas, paellas, really a lot of happy moments. I mention them first because we really started together this journey and we always have supported us with the each other. Then, I would like to thank all *Los Italianos*: Francesco Ricci, Francesco Pastorelli, Roberta, Maurizia, Michele, Fabio, Vincenzo, Nicola, Isa e Giovanna. It has been a pleasure and an unforgettable experience to enjoy Barcelona with all of you.

I also thank all the great friends and colleagues I met at ICFO: my first office mates Roberto and Jiří, Adam, Ramaiah, Anshuman, James, Pablo, Fabian, Pablo y Elsa, Georg, Matteo, Margherita, Mustafa, Boris, Daniel, Ben, Michele S., Miriam, Carlos, Roland, Juan, Lisa, Kevin, Jonas, Adri, Achim, Stijn, Mathieu, Antoine and Eric for sharing a bit of Flamenco, Ivan, Dominik, Cesar, Luca Tanzi, Luca Tagliacozzo, Nello, Angelo, Martina, Marco, Maria, Pietro, Alessio, Leticia, Simon, Anna, Carlo and many many others, 5 years and half are really a lot.

Much gratitude to my best spanish friend, which is not catalan, but he is from Valencia, Mister Paco Castera for having shared one amazing year in the atico together with several concerts and travels. I also thank Carlos and Almu for their friendship and constant presence on my birthday, typically with a *buen jamon*. Thanks to Maria Surrymury Subbrillo for her constant friendship and energy during these years, thanks also to Irene, Estela, Cristina, Bea, Lucia and, I mean, again, 5 years and half are really a lot. I would like to thank all my other flatmates in Barcelona: Asier Larretxea, Amélie Araguas, Thomas Koffel, Tabarca e Giovanna, Monsieur cabrón Simo Tadili, las filosofas catalanas Alba y Raquel y sobre todo Nicolò, Emanuele and Michele for having shared three amazing and unforgettable years in the fantastic *Pisazo*. Thank you very much for these great living experiences.

Special thanks to my parents, to which this thesis is dedicated, to my father Giacomo Lucivero, for his continuous and wise suggestions, for the constant support, for having taught me the importance and fairness in work, for being an exceptional father and also the most lovely and wise professor I ever met; and to my mother Rosa Petruzzella for her constant love and support, for being always close apart from the distance, for having taught me that "il toro va preso per le corna", even before coming to Spain. And well, she is also the most lovely and wise professoressa I ever met. I feel very lucky to have parents like them and this achievement would not have been possible without their guidance and support. I also thank my sister Marilena Lucivero and my brother in law Michele Guarino for having supported me in choosing Barcelona, without any doubt, for their support and for giving me the opportunity to become uncle twice, indeed I also thank my lovely nephews Matteo and Stefano for all the games and dances that we have

done during these years, when I was back home. I want also to thank all my entire family, especially my grandparents Giovanni and Titina fot their love, support and inspiration. Special thanks to my friends Aldo, Leandro, Bruno, Mario e la "storica e mitica comitiva del viale" for being as they are and for being always a safe harbour where to come back. Thanks to my old good friends Fedele, Chiara, Giorgia and thanks to Manuela for hosting me in New York in a delicate moment for my next future.

Last but not least, I am deeply grateful to Stefania Franklin, michuicanovia, for her love and support, patience and impatience during the last two years. I have been lucky to meet you in Barcelona and I am sure (I don't just hope) that together we can find the key for making of our future a wonderful adventure.

The show must go on! (Queen)